

**HYALURONAN AS EFFECTIVE PLATFORMS FOR COMBINATORIAL
CARBOHYDRATE DERIVATIVE GENERATION, AND FOR IMAGE-GUIDED
SURGERY WITH SURFACE-ENHANCED RAMAN SPECTROSCOPY (SERS)**

By

Kunli Liu

A DISSERTATION

Submitted to
Michigan State University
in partial fulfillment of the requirements
for the degree of

Chemistry—Doctor of Philosophy

2022

ABSTRACT

HYALURONAN AS EFFECTIVE PLATFORMS FOR COMBINATORIAL CARBOHYDRATE DERIVATIVE GENERATION, AND FOR IMAGE-GUIDED SURGERY WITH SURFACE-ENHANCED RAMAN SPECTROSCOPY (SERS)

By

Kunli Liu

Hyaluronan (HA) is a polysaccharide consisting of repeating disaccharides of N-acetyl-D-glucosamine and D-glucuronic acid. HA plays important roles in a wide range of biological events. The principal endogenous receptor of HA, cluster of differentiation 44 (CD44), is overexpressed on many types of tumor cells as well as inflammatory cells in human bodies. HA-CD44 interactions are important in cell adhesion, cell migration, induction of hematopoietic differentiation, and signaling for cell activation. Other HA receptors include lymphatic vessel endothelial HA receptor-1 (LYVE-1), and HA receptor for endocytosis (HARE).

HA is versatile for chemical modification or conjugation by exploiting the reactivity of carboxyl group, hydroxyl group, or the reducing end of the HA chain. Through chemical modification of HA, various kinds of self-assembled HA nanoparticles (HA-NPs) can be generated. There are increasing interests in utilizing HA-NPs for targeted imaging and therapy. Active targeting from HA-CD44 mediated interaction could lead to selective accumulation of HA-NPs at targeted disease sites. Chapter 1 is a review focusing on the synthesis strategies of self-assembled HA-NPs, as well as their applications in therapy and biomedical imaging.

With the recognition of the importance of HA-CD44 interactions, there have been substantial efforts to develop novel compounds capable of binding with CD44 to modulate CD44 biology. Chapter 2 reports a novel approach for generating HA derivatives with enhanced CD44 binding. By modifying the carboxyl group on HA with various amine, aldehyde, and isocyanide moieties through the Ugi reaction, 36 HA like polysaccharides were generated. Two lead

compounds were identified with enhanced CD44 binding from the polysaccharide library compared to unmodified HA, which was confirmed by surface plasmon resonance and cellular studies. Ski-learn as a machine learning tool was utilized to analyze the library of binding data and yield prediction with an accuracy over 80%. In conclusion, modification of HA via the Ugi reaction can be a promising approach to develop novel binders toward CD44.

While HA has been frequently employed as the targeting molecule in imaging via near infrared (NIR) or magnetic resonance (MRI) imaging, the potential of HA for surface-enhanced Raman spectroscopy (SERS) imaging has not yet been explored. SERS NPs are well-known for strong multiplexing capability, since different flavors of SERS NPs can be synthesized using different SERS dyes, resonant or non-resonant dye. SERS NPs are a promising tool for tumor margin removal in image-guided surgery. However, there are several challenges associated with SERS NPs for cancer imaging: 1) reproducible synthesis of SERS NPs; 2) ligand attachment for SERS NPs. Chapter 3 addresses these two issues by: 1) developing a reproducible protocol for 50 nm SERS NPs with low-femtomolar detection sensitivity; 2) employing liposome as the bridge for HA attachment to SERS NPs. The resulting HA-liposome SERS NPs have been successfully applied in imaging guided surgical removal of breast cancer in a spontaneous mouse breast cancer model.

ACKNOWLEDGEMENTS

I need to thank many people for all this to happen. First and foremost, I need to thank my advisor, Dr. Xuefei Huang, for this guidance and mentorship over the last five years. I feel deeply grateful and privileged to receive his support on projects that I've worked on, and on my life in general, especially during no-easy season of my life. Among many things that I've learned from him for science practice, there is patience, persistence, and being throughout. While I will miss the doctorate training with him, I strive to keep all these good qualities of work for future work.

I want to thank my guidance committee members, Dr. Melanie Cooper, Dr. Robert Maleczka and Dr. Aaron Odom. They've been with me through the whole journey: first committee meeting, second year comprehensive exam, and thesis defense. I want to thank them for their guidance and suggestions on the projects and on the thesis.

I want to thank all my collaborators: Dr. Zhen Qiu for our collaboration on SERS technology; Dr. Barry Finzel for our collaboration on HA derivatives; and Dr. Stephanie Watts for our collaboration on antisense oligonucleoside delivery. It is only by collaboration, by combining expertise in different fields, that we can make certain things happen.

I took many TEMs images throughout the years for characterizations of various nanoparticles. I want to thank Dr. Xudong Fan, Dr. Alicia Withrow for kindly and patiently assisting me with that. I want to thank Dr. Dan Holmes, Dr. Li Xie for their help on NMR, and thank Dr. Melinda Frame for her help on confocal imaging.

I want to thank people in the lab. Mehdi helped me with the synthesis of nanoparticles when I first joined the lab, and helped me get onboard. Zahra and Shuyao helped me with various things, including training with new assays. I feel grateful for all the suggestions from my lab-mates

during regular group meetings, practice for organic seminar, practice for comprehensive exam, and practice for thesis defense, and thank all of them for being supportive to me: Dr. Seyedmehdi Hossaini Nasr, Dr. Sherif Ramadan, Dr. Zahra Rashidijahanabad, Dr. Shuyao Lang, Dr. Herbert Kavunja, Shivangi Chugh, Dr. Xingling Pan, Zibin Tan, Mengxia Sun, Hunter Mcfall-Boegeman, Po-Han Lin, Morgan Mayieka, Athar Nakisa, Ida Shafiei, Cameron Talbot, Atique Ullah, Chia-Wei Yang, Dr. Somnath D. Bhagat, Dr. Dushen Chen, Vindula Alwis

I want to thank my family for everything I have. I want to thank my dad, my mom, my grandpa and my grandmon. Thank for their care for me since day one of my life. I'd like to thank my friends for supporting me throughout the journey. It is a privilege to meet you, be friends, and build mutual support with you. Especial thanks for Yubei (Eva) Liu for her support on me. I feel lucky and deeply grateful for our connections. Also thank many other friends as well: Dr. Zhilin Hou, Emmanuel Maloba, Ankush Chakraborty, Dr. Yapei Zhang, Qianyi Wang, Jiaojiao Wang.

TABLE OF CONTENTS

LIST OF TABLES	viii
LIST OF FIGURES	ix
KEY TO ABBREVIATIONS	xv
Chapter 1 Synthesis of self-assembled hyaluronan based nanoparticles and their applications in targeted imaging and therapy	1
1.1 Introduction	1
1.2 Method for synthesis of self-assembled HA-NPs	3
1.2.1 Non-cleavable linkage	4
1.2.2 Cleavable linkage	6
1.2.3 Complexation via hydrophobic interaction	7
1.2.4 Solvent exchange	7
1.2.5 Solvent evaporation	8
1.2.6 Complexation via electrostatic interaction	8
1.3 Imaging applications of self-assembled HA-NPs	9
1.3.1 NIR imaging	9
1.3.2 MRI imaging	11
1.3.3 Multimodal imaging	13
1.4 Therapeutic application of self-assembled HA-NPs	16
1.4.1 Delivery of small molecules to enhance therapeutic efficacy	19
1.4.2 Protein delivery	31
1.4.3 Nucleic acid delivery	32
1.4.4 Photodynamic therapy	40
1.4.5 Photothermal therapy	43
1.5 Conclusions and future outlook	46
REFERENCES	49
Chapter 2 Synthesis of self-assembled hyaluronan based nanoparticles and their applications in targeted imaging and therapy	61
2.1 Introduction	61
2.2 Results and discussions	62
2.2.1 Synthesis of the library of 36 HA like polysaccharides via the Ugi reaction	62
2.2.2 Binding of HA like polysaccharides with CD44 via competitive ELISA	65
2.2.3 Effect of loading percentage on binding of HA derivatives	68
2.2.4 Effect of isocyanide on binding of HA derivatives	69
2.2.5 Effect of molecular weight on binding of HA derivatives	70
2.2.6 Cytotoxicity evaluation of G2 modification	71
2.2.7 Binding of HA like polysaccharides with CD44 via SPR	72
2.2.8 In vitro evaluation of G2 using Raw 264.7 cells	74
2.2.9 Data analytics with ELISA library data	77
2.3 Conclusions	79
2.4 Experimental section	80

2.4.1	Reagents.....	80
2.4.2	Batch synthesis of HA derivatives on 96-well plate.....	80
2.4.3	Synthesis of individual HA derivative.....	81
2.4.4	Competitive ELISA	81
2.4.5	MTS assay.....	82
2.4.6	Cellular uptake of HA and G2 with Raw 264.7 cells	83
2.4.7	CD44 HABD cloning, expression and purification	83
2.4.8	Immobilized CD44 HABD SPR assay	83
2.4.9	Immobilized HA SPR assay.....	84
2.4.10	Immobilized HA SPR assay with ligand only binding subtraction	85
2.4.11	Machine learning modeling of library data.....	85
APPENDIX.....		86
REFERENCES		114
Chapter 3 Synthesis of Liposome-SERS-hyaluronate with low-femtomolar sensitivity and its potential for image guided surgery		118
3.1	Introduction.....	118
3.2	Result and discussions	120
3.2.1	Development of a robust synthesis protocol for SERS NPs	120
3.2.2	Other dye installation methods	125
3.2.3	Detection limit quantification of SERS NPs.....	127
3.2.4	Ratio metric evaluation of mixture of SERS flavors	128
3.2.5	Cytotoxicity evaluation of SERS NPs	129
3.2.6	Ligand attachment to SERS NPs	130
3.2.7	Liposome-SERS HA NPs enabled successful image-guided surgery of spontaneous breast cancer model in mice.....	134
3.3	Conclusion	137
3.4	Experimental section.....	138
3.4.1	Reagents.....	138
3.4.2	Sodium citrate assisted synthesis of SERS NPs	138
3.4.3	Tris base assisted synthesis of SERS NPs	139
3.4.4	Synthesis of Liposome-SERS NPs complex	140
3.4.5	Carbazole assay for hyaluronan quantification.....	140
3.4.6	Image-guide surgery through SERS imaging	140
3.4.7	Competitive ELISA	141
3.4.8	MTS assay with SERS NPs	142
APPENDIX.....		143
REFERENCES		147

LIST OF TABLES

Table 1.1 Fluorophores incorporated in self-assembled HA-NPs.....	10
Table 1.2 Self-assembled HA-NPs for multi-modality imaging.....	13
Table 1.3 Common hydrophobic moieties for self-assembled HA-NPs.....	18
Table 1.4 Self-assembled HA-NPs for tumor targeted delivery of PTX.	24
Table 1.5 Self-assembled HA-NPs for gene delivery.	33
Table 1.6 Self-assembled HA-NPs for photothermal therapy.....	44
Table 2.1 Machine learning model prediction for 11 data points randomly selected as the test set. Their corresponding inhibition change, and predicted inhibition changes were shown. The model was able to predict the sign of inhibition change for 9 out of 11 data points in the test set.	79
Table 2.2 Tabular format of library data of 36 entries in total.....	108
Table 2.3 Training set with 25 entries. Each entry was represented as a vector using one-hot encoding.....	110
Table 2.4 Test set with 11 entries. Each entry was represented as a vector using one-hot encoding.....	112
Table 2.5 Code script from Google Colab for machine learning.....	113

LIST OF FIGURES

Figure 1.1 Structure of HA.	1
Figure 1.2 Schematic demonstration of synthesis methods toward self-assembled HA-NPs.	3
Figure 1.3 Synthesis schemes for common methods for HA modifications. If the hydrophobic moiety has an amine group, direct conjugation can be achieved through amide coupling or reductive amination. A linker can be employed to conjugate HA and the hydrophobic moiety. The linker can have a carboxylic ester linkage or a disulfide linkage, such that the linker can be severed by hydrolysis or reduction in tumor sites to release the drug.	4
Figure 1.4 PEGylation helped to prolong in vivo circulation of HA-NPs. In vivo NIRF imaging in SCC7 tumor-bearing mouse after intravenous injection of DOX-loaded HACE and HACE-PEG nanoparticle. PEGylated HA-NPs lasted longer in vivo. This figure is reproduced with permission from Elsevier publisher ¹⁴	20
Figure 1.5 Ex vivo NIRF imaging 1-day post-injection of nanoparticles showed that PEGylated HA-NPs accumulated more in tumor: a) Optical and Cy5.5 filtered images of excised organs and tumors; b) fluorescence intensity values. This figure is reproduced with permission from Elsevier publisher ¹⁴	21
Figure 1.6 pH responsive HA nanoparticles. Acetal linkage enables pH sensitive drug release. This figure is reproduced with permission from Elsevier publisher ¹⁹	26
Figure 1.7 Preparation of HA conjugated atorvastatin NP. Aminated ATV was conjugated to HA via amide formation. This figure is reproduced with permission from Royal Society of Chemistry (RSC) ¹⁵	31
Figure 1.8 HA conjugated cyclodextrin-oligoethylenimine star polymer for CD44-targeted gene delivery. This figure is reproduced with permission from Elsevier ¹¹⁴	39
Figure 1.9 Catalase-integrated HA as nanocarriers (HA-CAT@aCe6 NPs) for enhanced photodynamic therapy in solid tumor. This figure is reproduced with permission from American Chemical Society (ACS) publisher ¹²²	42
Figure 2.1 Synthesis of HA like polysaccharides via the Ugi reaction. a) Ugi reaction scheme. Nine different amines (benzylamine, ethanolamine, 3-amino-1-propanol, amylamine, cycloheptylamine, 4-phenylbutylamine, 3-phenyl-1-propylamine, tryptamine, and tyramine), four different aldehydes (heptafluorobutyraldehyde, formaldehyde, isovaleraldehyde and propionaldehyde), and cyclohexyl isocyanide were used to produce HA derivatives. b, c) ¹ H-NMR spectra of G2 and HA. G2 corresponds to HA modified through the Ugi reaction with 3-phenyl-1-propylamine (amine G), formaldehyde (aldehyde 2), and cyclohexyl isocyanide. Resonance between 1.0 ppm and 1.7 ppm are from the cyclohexyl rings. Peaks between 7.0 ppm and 7.5 ppm are from the phenyl ring of the amine. The level of modification was estimated as 18% according to the integration value of ¹ H-NMR signals between 7.0 ppm and 7.5 ppm.	65

Figure 2.2 Heat-map of inhibition % changes of various HA derivatives. A positive inhibition change value would indicate the HA derivative has enhanced affinity toward CD44. Red color represents enhanced affinity, while green color represents decreased affinity with the average and standard deviation from three samples shown (N = 3). While the vast majority of the compounds show lower binding as represented by the negative inhibition % change values, F2 and G2 exhibited the highest enhancement in CD44 binding. 67

Figure 2.3 a) Competitive ELISA results for F2, and G2. F2 and G2 showed more potent competition against b-HA for CD44 binding as compared with HA polysaccharide (10 kDa). Statistical test was performed through one way ANOVA. *** $p < 0.001$; **** $p < 0.0001$. b) Dose-dependent inhibition of HA (10 kDa), F2 and G2 at various concentrations. The inhibition % was calculated following **Equation 1**. The average values and the standard deviation from three samples are shown (N = 3). 68

Figure 2.4 Binding evaluation of compounds B2 and G2 at various loading percentage. HA derivatives at different loading percentages were synthesized with various stoichiometry ratio. a) Lead compound G2 was synthesized at different loading percentage. It was found that loading percentage up to 38% of compound G2 showed significantly stronger competition. A2 at 25 % was shown as a negative sample for comparison. b) For compound B2, loading percentage lower than 55% did not decrease its binding much. Significant binding decrease was observed then the loading percentage was above 65%. The average values and the standard deviation from three samples were shown (N = 3). 69

Figure 2.5 Evaluation of G2 derivatives formed with different isocyanides. 0.5 μg HA or derivatives was used to compete against 0.5 μg b-HA. The loading percentage of all three modification was around 30%. Modification using cyclohexyl isocyanide yielded the G2 derivatives with the highest binding, compared with derivatives modified with butyl or pentyl isocyanide. The average values and the standard deviation from three samples were shown (N = 3). Statistical test was performed through one way ANOVA. **** $p < 0.0001$ 70

Figure 2.6 G2 modification using higher molecular weight of HA, a) 60 kDa and b) 100 kDa. G2 derivatives with 60 kDa and 100 kDa HA backbone had stronger inhibition than the corresponding HA polysaccharides. Competition was set at 0.1 μg of equal weight of competitor for either HA or G2. Statistical test was accomplished with two-tailed unpaired t-test. ** $p < 0.01$ 71

Figure 2.7 Cytotoxicity evaluations of G2 of different loading percentage at various concentrations. G2 showed no cytotoxicity at all loading percentage and concentrations evaluated. 72

Figure 2.8 Inhibition % of F2 and G2 relative to HA toward CD44 binding based on the SPR data. The error bars depict the standard deviation of the observations collected (N = 3). G2 demonstrated a 37% increase in relative percentage of inhibition. The average values and the standard deviation from three samples are shown. Statistical test was accomplished with two-tailed unpaired t-test. ** $p < 0.01$ 74

Figure 2.9 Competitive ELISA confirmed that G2-FITC has stronger binding to CD44 compared with HA-FITC. Equal concentrations of HA-FITC and G2-FITC were added to compete with b-

HA. ELISA showed that G2-FITC bound stronger to CD44 as compared to HA-FITC. It also indicates that FITC attachment does not impact the relative competition potency of HA and G2. The average values and the standard deviation from three samples are shown. Statistical test was accomplished with two-tailed unpaired t-test. *** $p < 0.001$ 75

Figure 2.10 G2-FITC and HA-FITC at three concentrations were incubated with Raw 264.7 cells. 1x concentration corresponds to HA at 25 $\mu\text{g/mL}$. For cells only group, no HA or G2 was added, and the mean fluorescence intensity was low. Cells incubated with G2-FITC exhibited stronger fluorescence compared with those incubated with HA-FITC across three different concentrations. The average values and the standard deviation from three samples are shown. Statistical test was carried out with a two-tailed unpaired t-test. * $p < 0.05$ 76

Figure 2.11 Confocal imaging confirms the uptake of G2 and HA in Raw 264.7 cells. Blue DAPI channels show the locations of nuclei; green FITC channels show the locations of the HA or G2; red lysotracker channels show the locations of the lysosomes. Combined image is the overlay of DAPI, green FITC and the red lysotracker channels. 77

Figure 2.12 Vector representation of library data was accomplished through one-hot encoding. The input size is 13, corresponding to 9 different amines and 4 different aldehydes..... 78

Figure 2.13 Sensograms of CD44 incubated with HA (10 kDa) at the following concentration range (from bottom to top): 2500 $\mu\text{g/mL}$, 1250 $\mu\text{g/mL}$, 625 $\mu\text{g/mL}$, 312 $\mu\text{g/mL}$, 156 $\mu\text{g/mL}$, 78 $\mu\text{g/mL}$, 39 $\mu\text{g/mL}$ and 19 $\mu\text{g/mL}$ 87

Figure 2.14 Sensograms of HA (10 kDa) only at the following concentration range: 2500 $\mu\text{g/mL}$, 1250 $\mu\text{g/mL}$, 625 $\mu\text{g/mL}$, 312 $\mu\text{g/mL}$, 156 $\mu\text{g/mL}$, 78 $\mu\text{g/mL}$, 39 $\mu\text{g/mL}$ and 19 $\mu\text{g/mL}$ 87

Figure 2.15 Sensograms of reference subtraction (as indicated by Figure 6 in main text) at the following concentration range (from bottom to top): 2500 $\mu\text{g/mL}$, 1250 $\mu\text{g/mL}$, 625 $\mu\text{g/mL}$, 312 $\mu\text{g/mL}$, 156 $\mu\text{g/mL}$, 78 $\mu\text{g/mL}$, 39 $\mu\text{g/mL}$ and 19 $\mu\text{g/mL}$ 88

Figure 2.16 Sensograms of HA (10 kDa) in the immobilized CD44 SPR assay. Sensograms showed a non-plateau during the equilibrium phase and slow dissociation phase that never reached the baseline, at wide concentration range (from top to bottom): 2500 $\mu\text{g/mL}$, 1250 $\mu\text{g/mL}$, 625 $\mu\text{g/mL}$, 312 $\mu\text{g/mL}$, 156 $\mu\text{g/mL}$, 78 $\mu\text{g/mL}$, 39 $\mu\text{g/mL}$ and 19 $\mu\text{g/mL}$. This implies the non-specific interaction and avidity issue of the polymeric-HA. 89

Figure 2.17 ^1H -NMR spectrum of compound B2 at 12% loading, 10 kDa. 90

Figure 2.18 ^1H -NMR spectrum of compound B2 at 31% loading, 10 kDa. 91

Figure 2.19 ^1H -NMR spectrum of compound B2 at 43% loading, 10 kDa. 92

Figure 2.20 ^1H -NMR spectrum of compound B2 at 57 % loading, 10 kDa. 93

Figure 2.21 ^1H -NMR spectrum of compound B2 at 69% loading, 10 kDa. 94

Figure 2.22 ^1H -NMR spectrum of compound B2 at 92% loading, 10 kDa. 95

Figure 2.23 ^1H -NMR spectrum of compound G2 at 17% loading, 10 kDa.	96
Figure 2.24 ^1H -NMR spectrum of compound G2 at 25% loading, 10 kDa.	97
Figure 2.25 ^1H -NMR spectrum of compound G2 at 38% loading, 10 kDa.	98
Figure 2.26 ^1H -NMR spectrum of compound G2-butyl isocyanide, 10 kDa.	99
Figure 2.27 ^1H -NMR spectrum of compound G2-pentyl isocyanide, 10 kDa.	100
Figure 2.28 ^1H -NMR spectrum of compound G2, 60 kDa.	101
Figure 2.29 ^1H -NMR spectrum of compound G2, 100 kDa.	102
Figure 2.30 ^1H -NMR spectrum of compound A2, 10 kDa.	103
Figure 2.31 ^1H -NMR spectrum of compound A4, 10 kDa.	104
Figure 2.32 ^1H -NMR spectrum of compound D2, 10 kDa.	105
Figure 2.33 ^1H -NMR spectrum of compound F2, 10 kDa.	106
Figure 2.34 ^1H -NMR spectrum of compound I2, 10 kDa.	107
Figure 3.1 Tris base assisted synthesis of SERS NPs. 17 nm seeds were first synthesized via sodium citrate reduction, followed by seed mediated growth of homogenous 50 nm AuNPs via tris base at 100 °C. Raman dye was added right after the formation of AuNPs and stirred for 1 min, followed by immediate cooling down in an ice bath. This method worked for non-resonant or resonant dye yielding bright SERS-NPs, while the working concentration differed for two orders of magnitude for non-resonant dye (10 μM) vs resonant dye (50 nM).	122
Figure 3.2 Characterizations of SERS NPs synthesized via the sodium citrate reduction method, and the tris-base reduction method. Sodium citrate reduction can lead to heterogeneity when the targeted size is above 30 nm as shown in TEM images. This is also indicated by size distribution in DLS. For the tris-base method, 17 nm seeds were first synthesized with sodium citrate reduction, followed by seed-mediated growth of homogeneous SERS NPs with tris base as a weak reducing agent. With seed mediated, tris base assisted synthesis, there was a significant improvement both in terms of size and homogeneity of shape.	123
Figure 3.3 Structures of non-resonant Raman dyes and other compounds screened.	124
Figure 3.4 Structures of resonant Raman dyes and other compounds screened.	125
Figure 3.5 Various methods for the synthesis of SERS NPs. 1) Tris base assisted synthesis of SERS NPs. This method works for non-resonant or resonant dye, while the working concentrations differed by two orders of magnitude. 2) Sodium citrate assisted synthesis of SERS NPs with heterogeneous size and shape distribution. This method can only work for non-resonant dye, with working concentration to be 100 times smaller than the one for tris base assisted synthesis. 3) Raman dye installation with concentrated AuNPs. 50 nm AuNPs from tris base assisted synthesis	

were incubated with 2 μ M resonant dye for 10 mins, followed by PEGylation. This method can only work for resonant dye. Dye installation has to precede PEGylation to yield SERS signals. 127

Figure 3.6 (a) Raman spectra of SERS particles (S420, S421, S440, S481, IR780, and Cy5.5) acquired by the Renishaw system; (b) The highest peaks of Raman spectra acquired by the Renishaw system of each flavor at different concentrations. 128

Figure 3.7 Ratio metric experiment. (a) the phantom with the mixture SERS solution (S420, S481, and S421); (b) the result of ratio estimation using the demultiplex algorithm. 129

Figure 3.8 MTS assay with S420 prepared from the tris base assisted synthesis. SERS-NPs were pegylated to prevent aggregation in cell media. Various concentrations of S420-PEG were incubated with Raw cells for 3 hours: 0 pM, 12 pM, 24 pM, 45 pM and 100 pM. No cytotoxicity was observed for all concentrations tested. 130

Figure 3.9 Characterizations of SERS-HA and SERS-PEG. A) HA competition with b-HA at various concentrations. B) Dose-dependent competition of SERS-HA (10 kDa) with b-HA. SERS-HA showed weak competition even at elevated concentration at 250 pM. C) Competition of 50 pM SERS-HA with HA at different molecular weight: 10 kDa, 250 kDa and 1500 kDa. Similar results were observed across 3 different molecular weights. D) Pictures of SERS, SERS-HA and SERS-PEG in MilliQ water or PBS: 1) 20 pM S420 in MilliQ water; 2) 20 pM S420 in PBS, aggregation is indicated by color change from red to black; 3) 20 pM S420-HA in PBS; 4) 20 pM S481-PEG in PBS. HA or PEG attachment to SERS NPs significantly improved salt stability of SERS NPs in PBS. E, F) DLS of S420-HA and S481-PEG. Size increase was observed compared with unmodified SERS NPs. 132

Figure 3.10 Characterizations of Liposome-SERS-HA and Liposome-SERS-PEG. A) Competitive ELISA showed that HA attachment was successfully only with thiolated HA. Strong competition was observed at only 20 pM when the particles were made with thiolated HA. B) Dose dependent competition of Liposome-SERS-HA. Liposome-SERS-PEG showed no competition at all four concentrations. DLS of C) liposome-SERS-HA and D) liposome-SERS-PEG respectively. E) TEM images of liposome-SERS-HA. SERS NPs were chelated to the surface of liposome. 0.5 % uranyl acetate staining was employed for TEM imaging (scale bar: 200 nm). 134

Figure 3.11 Raman Image-guided surgery using the mixture solution of Liposome-S421-HA and Liposome-S440-PEG. (a) photograph of the tumor mouse; (b) Sequential tumor resection, (b1) photographs of scanning area, (b2) the ratiometric Raman (S421/S440) images, (b3) overlaid images; (c) H&E and IHC images of resected tumors from (b), (c1-c2) H&E images acquired by 10 x and 40 x magnification, respectively, (c3) the corresponding IHC images acquired by 40 x magnification. 136

Figure 3.12 Ratiometric images of the mixture solution of Liposome-S421-HA and Liposome-S440-PEG applied on the tumor and control tissues. (a) photograph of specimens; (b) ratiometric Raman image(S421/S440) ; (c) overlaid image between the photograph and the ratiometric Raman image; (d) the average of Ratiometric Raman weight 137

Figure 3.13 (a) Schematic configuration of the fiber bundle Raman spectrometer. (b) Photograph of the fiber bundle Raman spectrometer. A 785 nm laser (iBeam Smart 785, Toptica Photonics, Munich, Germany) is applied to illuminate the sample. The scattered Raman spectra is acquired by the custom-made fiber bundle Raman probe (Fiber guide Industries, Caldwell, ID, USA). The lens L1 (f=6.83 mm, PLCS-4.0-3.1-UV, CVI Laser Optics, Albuquerque, NM, USA) is used to collimate both excitation (785 nm laser) and emission (scattered Raman spectra) through the fiber bundle Raman probe. An optical relay, containing two lenses (L2, L3) and a long pass filter (LPF), couples the light into the slit of the spectrometer (Kymera 193i-A, Andor Technology, Belfast, UK) and CCD camera (1024 pixel x 256 pixels with pixel size of 26 μm x 26 μm ; DU920P Bx-DD, Andor technology, Belfast, UK). 144

Figure 3.14 (a1-a7) Raman spectra of SERS particles (S420, S421, S440, S481, IR780, and Cy5.5) at seven different concentrations (100 pM, 20 pM, 4 pM, 800 fM, 160 fM, 32 fM, 6 fM) for each flavor; (a8) the quantitative weight calculation graph using demultiplexing algorithm, x-axis is the concentration and y-axis the weight value..... 145

Figure 3.15 (a1-a7) Raman spectra of SERS particles (S420, S421, S440, S481, IR780, and Cy5.5) at seven different concentrations (100 pM, 20 pM, 4 pM, 800 fM, 160 fM, 32 fM, 6 fM) for each flavor; (a8) the quantitative weight calculation graph using demultiplexing algorithm, x-axis is the concentration and y-axis is the weight value. 146

KEY TO ABBREVIATIONS

5-FU	5-Fluorouracil
ADH	Adipic Dihydrazide
AMF	4'-(Aminomethyl)Fluoresceine Hydrochloride
ANF	α -Naphthoflavone
ASO	Oligodeoxynucleotide
ATV	Atorvastatin
b-HA	Biotinylated HA
BA	Boronic Acid
BHQ3	Black Hole Quencher3
BSA	Bovine Serum Albumin
CAB	Carbonic Anhydrase B
CBA	Cystamine Bisacrylamide
CD44	Cluster Of Differentiation
CDMT	2-Chloro-4,6-Dimethoxy-1,3,5-Triazine
CDs	Cyclodextrins
Ce6	Chlorin E6
CEs	Ceramides
cis-Pt	Cisplatin
CLSM	Confocal Laser Scanning Microscopy
CPT	Camptothecin
CT	Computed Tomography
CTAB	Cetyltrimethylammonium Bromide

CuAAC	Copper(I)-Catalyzed Alkyne-Azide Cycloaddition
DCC	Dicyclohexyl Carbodiimide
DM	Deacetyl Mycoepoxydience
DMEM	Dulbecco's Modified Eagle Medium
DMSO	Dimethylsulfoxide
DOCA	Deoxycholic Acid
DOX	Doxorubicin
DPP	Diketopyrrolopyrrole
DPPC	1,2-Dipalmitoyl-Sn-Glycero-3-PC
DTPA	Diethylenetriaminepentaacetic Acid
DTX	Docetaxel
EDC	(1-Ethyl-3-(3-Dimethylaminopropyl) Carbodiimide)
EGCG	Epigallocatechin-3-O-Gallate
ELISA	Competitive Enzyme Linked Immunosorbent Assay
EPR	Enhanced Permeability Retention
FACS	Fluorescence-Activated Cell Sorting
FBS	Fetal Bovine Serum
FDPP	Furan Flanked Diketopyrrolopyrrole
FITC	Fluorescein Isothiocyanate
GA	Glycyrrhetinic Acid
GAG	Glycosaminoglycan
GFP	Green Fluorescent Protein
GSH	Glutathione

H&E	Hematoxylin And Eosin
HA	Hyaluronan
HA-NPs	HA Nanoparticles
HABD	Hyaluronic Acid Binding Domain
HARE	HA Receptor For Endocytosis
HEPES	2-[4-(2-Hydroxyethyl)Piperazin-1-yl]Ethane-1-Sulfonic Acid
hMSCs	Human Mesenchymal Stem Cells
HRP	Horseradish Peroxidase
Hy	Hypericin
IHC	Immunohistochemistry
IHC	Immunoglobulin G
LYVE-1	Lymphatic Vessel Endothelial HA Receptor
MAE	Mean Absolute Error
MAE	Mean Absolute Error
MDR	Multi-Drug Resistance
MPN	Metal-Phenolic Network
MRI	Magnetic Resonance Imaging
MTT	(3-(4,5-Dimethylthiazol-2-Yl)-2,5-Diphenyl Tetrazolium Bromide)
NAC	N-Acetyl-L-Cysteine
NAR	Naringenin
NHS	N-Hydroxysuccinimide
NIR	Near Infrared
NMR	Nuclear Magnetic Resonance Spectroscopy

NPs	Nanoparticles
OD	Optical Density
OEI	Oligoethyleneimine
P85	Pluronic 85
PA	Photoacoustic Imaging
PANI	Polyaniline
PBA	Aminopropyl-1-Pyrenebutanamide
PBLG	Poly(Γ -Benzyl L-Glutamate)
PBS	Phosphate-Buffered Saline
PCL	Polycaprolactone
PDGF-BB	Platelet Derived Growth Factor
PDI	Photodynamic Imaging
PEG	Polyethylene Glycol
PEI	Polyethylenimine
PFCs	Perfluorocarbons
Pgp	p-Glycoprotein
PLA	Polylactic Acid
PLGA	Poly(Lactic-Co-Glycolic Acid)
PLL	Poly-L-Lysine
Ppa	Pyropheophorbide A
PTT	Photothermal Therapy
PTX	Paclitaxel
RHAMM	Receptor For Hyaluronate-Mediated Motility

RNO	p-Nitrosodimethylaniline
RUs	Response Units
SERRS	Surface-Enhanced Resonant Raman Scattering
SERRS NPs	Surface-Enhanced Resonant Raman Scattering Nanoparticles
SERS	Surface-Enhanced Raman Scattering
SPR	Surface Plasma Resonance
TEOS	Tetraethyl Orthosilicate
TGF	Transforming Growth Factor
THP	Tris(Hydroxypyridinone)
TIBA	2,3,5-Triiodobenzoic Acid
TMB	3,3',5,5'-Tetramethylbenzidine
TPP	Triphenylphosphonium
VEGF	Vascular Endothelial Growth Factor
VES	Vitamin E Succinate
β -CD	β -Cyclodextrin

Chapter 1 Synthesis of self-assembled hyaluronan based nanoparticles and their applications in targeted imaging and therapy

1.1 Introduction

HA is a glycosaminoglycan (GAG), consisting of disaccharide repeating units of β -1,4-D-glucuronic acid- β -1,3-D-glucosamine, as shown in **Figure 1.1**. CD44 is the principal endogenous receptor of HA in human bodies. Other HA receptors include the HA receptor for endocytosis (HARE), lymphatic vessel endothelial HA receptor (LYVE-1), and the receptor for hyaluronate-mediated motility (RHAMM) ¹. HA is generally considered to be biocompatible, biodegradable, non-immunogenic, and nontoxic. Meanwhile, chemical conjugation or modification on HA can be readily performed by exploiting the reactivities of the carboxyl groups or hydroxyl groups ². The inherent biocompatibility, targeting ability, as well as versatility in bioconjugation, render HA a good targeting ligand in nanomedicine.

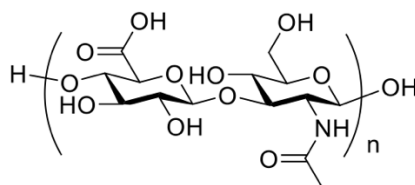


Figure 1.1 Structure of HA.

There have been increasing interests in utilizing NPs for both therapy and imaging applications. Maeda and co-workers first reported the revolutionary concept of the EPR effect ^{3,4}. The EPR effect is a phenomenon in which NPs preferentially accumulate in the targeted sites such as tumor microenvironment. HA has been utilized extensively in nanotechnology, which can be broadly divided into two categories. A common strategy to interface HA and nanomaterials is to conjugate HA to the external surface of NPs, which include iron oxide NPs ⁵, silica NPs ⁵, carbon nanotubes ⁶, liposomes ⁷, quantum dots ⁶, and gold NPs ⁸. Interested readers can refer to multiple

reviews published on this topic ⁹⁻¹². The other major category of HA-NPs is self-assembled HA-NPs, which can be bio-compatible without the potential detrimental effects from some of the core inorganic particles. Self-assembled HA-NPs can be a good candidate for drug release due to their large cargo carrying capacity. Meanwhile, HA can be degraded by hyaluronidases in tumor microenvironment ¹³. In this way, the drug encapsulated in self-assembled HA-NPs can be selectively released in the targeted site. In addition, many different components could be packed into self-assembled HA-NPs for both therapeutic and imaging purposes. For example, doxorubicin (DOX) and Cy5.5 can both be incorporated into HA-NPs, and the resulting NPs have the ability for both targeted drug delivery and near infrared (NIR) imaging ¹⁴. This also helps to alleviate the aqueous solubility challenges since many drugs are hydrophobic with poor aqueous solubility.

A wide variety of drugs was incorporated into self-assembled HA-NPs for the treatment of various diseases, including cancer and inflammation. Meanwhile, many imaging functionalities could be incorporated into HA-NPs as well, including NIR, computed tomography (CT), photodynamic imaging (PDI), photoacoustic imaging (PA) and magnetic resonance imaging (MRI).

This chapter will be divided into three sections. In the first section, general synthesis methods and techniques for self-assembled HA-NPs will be discussed. In the second section, the application of HA-NPs in biomedical imaging will be summarized. In the third section, the therapeutic applications of HA-NPs will be presented, including drug delivery, gene delivery, photothermal therapy (PTT) and photodynamic therapy (PDT). In the second and third sections, some discussions of HA-NP synthesis are also included to illustrate how different synthesis strategies and techniques better fit the specific therapeutic or imaging applications.

1.2 Method for synthesis of self-assembled HA-NPs

The synthetic design of self-assembled HA-NPs can be flexible by exploiting the reactivity of carboxyl group, hydroxyl group, or the reducing end of the HA chain, as shown in **Figure 1.2**. HA can be functionalized through cleavable covalently linkages, including carboxylic esters and di-sulfides, or more hydrolytically stable covalent linkages, mostly amide bonds. Electrostatic interactions and hydrophobic-hydrophobic interactions are commonly employed for the self-assembly process. The common synthetic methods were summarized in **Figure 1.3**. Overall, a wide variety of techniques can be used to encapsulate drugs or incorporate imaging functionalities into self-assembled HA-NPs.

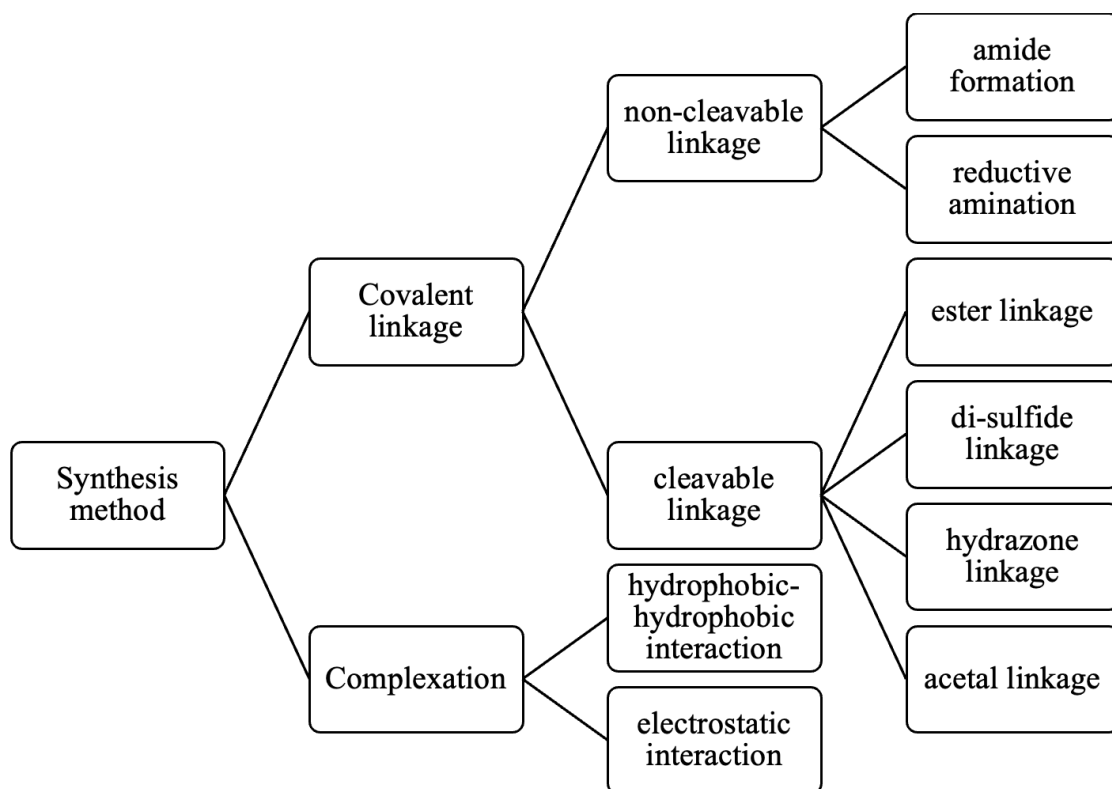


Figure 1.2 Schematic demonstration of synthesis methods toward self-assembled HA-NPs.

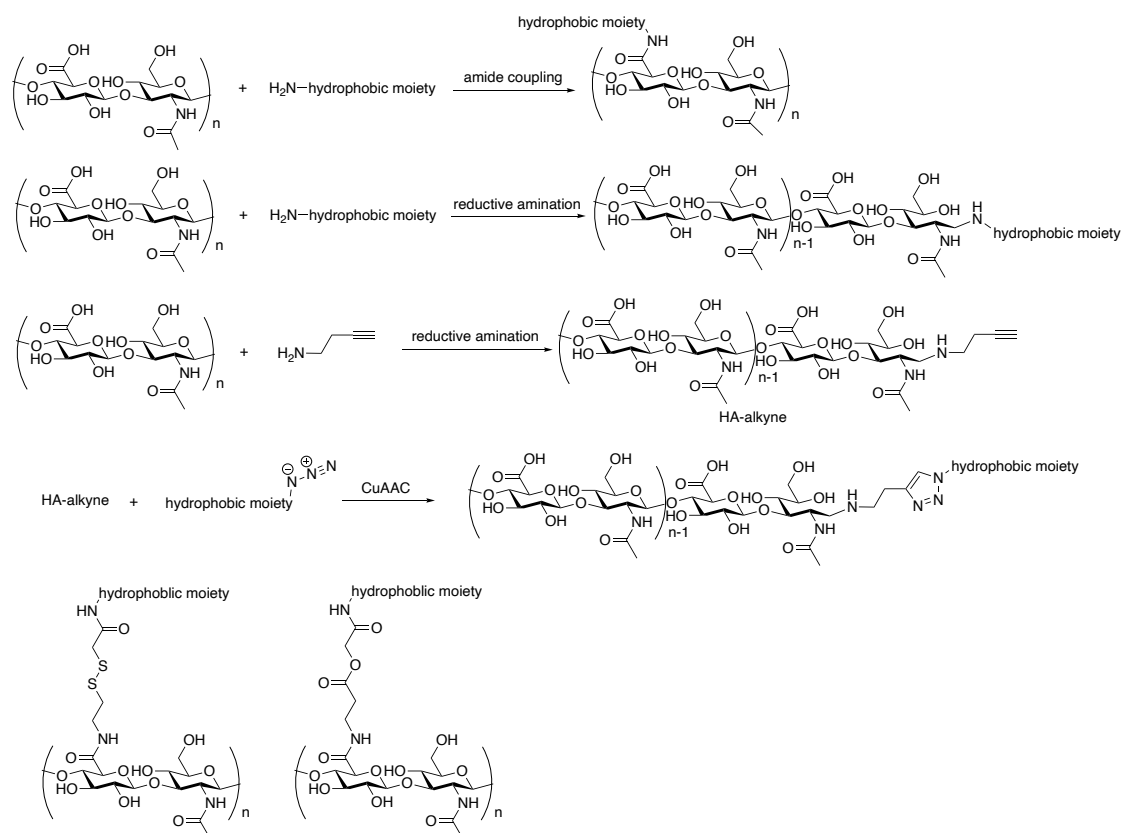


Figure 1.3 Synthesis schemes for common methods for HA modifications. If the hydrophobic moiety has an amine group, direct conjugation can be achieved through amide coupling or reductive amination. A linker can be employed to conjugate HA and the hydrophobic moiety. The linker can have a carboxylic ester linkage or a disulfide linkage, such that the linker can be severed by hydrolysis or reduction in tumor sites to release the drug.

1.2.1 Non-cleavable linkage

To induce self-assembly, a hydrophobic domain can be covalently conjugated with HA first, which is commonly conducted through the carboxyl group on the HA chain *via* amide formation. The extent of modification must be carefully controlled, since a high degree of modification can significantly reduce the binding ability of HA toward its biological receptor such as CD44, while a low degree of modification might not introduce sufficient hydrophobicity to facilitate self-assembly.

If the hydrophobic components have an amine group, the conjugation can be achieved by amide formation. For example, aminated atorvastatin was conjugated to HA *via* 2-chloro-4,6-

dimethoxy-1,3,5-triazine (CDMT) promoted coupling to form the HA-atorvastatin conjugate, which can then self-assemble into HA-NPs in aqueous solutions ¹⁵. Alternatively, if the hydrophobic components have a carboxyl group, they can be transformed to *N*-hydroxysuccinimide (NHS) ester first. Adipic dihydrazide (ADH) can also be conjugated to HA, yielding hydrazide functionalized HA-ADH, which can then react with the NHS ester of the hydrophobic components to produce the conjugate. As an example, NHS ester of chlorin Ce6, a fluorescence dye, has been conjugated to HA-ADH for photothermal therapy ¹⁶.

As an alternative to amide functionalization, reductive amination can be performed through the hemiacetal reducing end of the HA chain. An advantage of conjugation through reductive amination is that it preserves the functional groups such as carboxylates within the polysaccharide backbone necessary for HA binding to CD44 ¹⁷. On the other hand, linkage through the reducing end can only conjugate one exogenous compound per chain, which must have high molecular weight to bestow sufficient hydrophobicity for self-assembly. In addition, the relatively low reactivity of the reducing end hemiacetal group can render the reductive amination reaction difficult.

To overcome the low reactivity of the reducing end, an attractive strategy is to employ the copper(I)-catalyzed alkyne-azide cycloaddition (CuAAC) reaction, which has high reactivity and is orthogonal to common functional groups present in HA. A CuAAC reactive linker, for example, propargylamine, can be installed to the reducing end of HA through reductive amination with a large excess of the reagent, as shown in **Figure 1.3** ¹⁸. Subsequently, the hydrophobic component functionalized with an azide can be conjugated to HA *via* the CuAAC reaction ¹⁹. As most of the hydrophobic component being employed so far has a molecular weight close to or greater than 1000 g/mol, for HA with average molecular weight of 16kDa, this conjugation method will result

in a weight ratio of HA to hydrophobic component to be 16 : 1, which is sufficient for the assembly to occur.

1.2.2 Cleavable linkage

Cleavable linkage is frequently employed in self-assembled HA-NPs. Commonly utilized release methods include pH and redox signals through cleavable linkages such as carboxylic ester, hydrazone, acetal, and di-sulfide. Hydrophobic drugs can be covalently conjugated to HA via a cleavable linker. Upon reaching the target site, the linker can be cleaved, selectively releasing the cargo.

Carboxylic esters are intrinsically more labile than the corresponding amide moieties toward hydrolysis. Linking hydroxyl group bearing drugs with HA through an ester bond can deactivate the drug and reduce the potential off target effects ²⁰. Upon reaching the desired target site, the ester bond can be cleaved by hydrolytic enzymes, regenerating the active drug to exert its biological functions. As an example, paclitaxel (PTX) has been conjugated to HA *via* an ester linkage, yielding self-assembled HA-PTX conjugate for enhanced anti-tumor effects ²¹.

Hydrazone linkage enables pH sensitive drug release. While they are generally stable under the physiological pH (7.4), hydrazones can be rapidly cleaved at more acidic pHs typically encountered in late endosome and lysosomes (pH ~5.0). For the design of self-assembled HA-NPs, a carbonyl bearing drug can be conjugated with hydrazide functionalized HA via a hydrazone bond ²².

The acetal linkage, similar to the hydrazone and ester linkage, enables pH responsive release. It exhibits significantly accelerated cleavage at endo/lysosomal pH compared to physiological condition. A pro-drug with acetal linkage can be conjugated to HA. For example, a PTX pro-drug with an acetal linkage was linked with HA through the reducing end. As a result of

acetal cleavage in the endo/lysosomal compartments, PTX would be quickly and selectively released in tumor tissues ¹⁹.

Disulfide linkage enables redox-sensitive drug release. Disulfides are stable in mildly oxidizing extracellular environment. On the other hand, as the level of reducing agents such as free glutathione (GSH) is significantly higher intracellularly, the disulfide bond is prone to rapid cleavage via a disulfide exchange reaction with intracellular reductants such as GSH. In addition, the tumor environment is more reducing as compared with normal tissues ^{23, 24}. For example, Zhang and coworkers developed self-assembled HA-NPs in which deoxycholic acid (DOCA) was covalently conjugated to HA via a disulfide linkage, which encapsulated PTX in the hydrophobic core ²³. *In vitro* drug release studies demonstrated an accelerated release of PTX under a reducing condition.

1.2.3 Complexation via hydrophobic interaction

In this strategy, a hydrophobic component, be it a drug or a fluorophore, is conjugated to HA. This conjugate can be self-assembled into NPs, and additional components can be packed into the NPs for imaging or therapeutic purposes. The resulting NPs will have HA coating on the surface and a hydrophobic core²⁵.

1.2.4 Solvent exchange

Solvent exchange, also called nanoprecipitation, is the most popular method used in forming self-assembled HA-NPs. It is easy to operate and usually leads to homogeneous size distribution and high loading efficiency. Solvent exchange method involves dialysis to exchange the organic solvent, typically DMSO or ethanol, to water. For example, a solution of PTX in ethanol can be added to an aqueous solution of HA-DOCA conjugate to allow for PTX encapsulation. Dialysis is subsequently performed to remove ethanol leading to HA-NPs with PTX

encapsulated ²³. Besides solution based synthesis, microfluidic techniques can be applied in nanoprecipitation for the synthesis of HA-NPs ²⁶. There are numerous advantages associated with microfluidic techniques compared with conventional solution-based synthesis. First, microfluidic based production enables the convenience of fine-tuning reaction parameter, such as flow rate ratio, polymer concentration and temperature, and thus allows for better homogeneity and reproducibility of NPs ^{26, 27}. Secondly, nanoprecipitation reaction is usually faster than conventional solution-based synthesis, allowing for rapid and large-scale synthesis of NPs. Thirdly, reaction conditions and parameters during microfluidic based production can be carefully controlled and fine-tuned, leading to better reproducibility.

1.2.5 Solvent evaporation

In this method, HA conjugate and other hydrophobic components to be encapsulated, are dissolved in an organic solvent such as MeOH. Upon removal of the organic solvent, the mixture is resuspended in aqueous solution by vortexing to form NPs ¹⁴. A drawback of this method is that it can lead to large NP sizes and heterogeneous size distribution.

1.2.6 Complexation via electrostatic interaction

HA is highly negatively charged due to the carboxyl groups in the polymer chain. Electrostatic interactions can be conveniently employed for self-assembly of HA-NPs. HA-chitosan is the most prominent example of self-assembled HA-NP formation using electrostatic interactions. Chitosan is a polysaccharide consisting of β -1,4 linked D-glucosamine and *N*-acetyl-D-glucosamine. It is highly positively charged due to the presence of free amine groups. By simply mixing HA, chitosan and triphosphate, HA-chitosan NP can be produced, with triphosphate acting as a cross-linker stabilizing the core and HA electrostatically adsorbed on the surface ²⁸. Besides chitosan, polyaniline (PANI) is another highly positively charged polymer. HA can interact with

PANI to form NPs, which are good candidates for photothermal therapy, since PANI can generate a substantial amount of heat upon NIR irradiation ²⁹.

Small molecules can form strong electrostatic interaction with HA as well, leading to the formation of self-assembled HA-NPs. For example, Gao and co-workers developed self-assembled HA-NPs where ionic bonds were used for self-assembly ³⁰. DOX was first conjugated to triphenylphosphonium to form positively charged triphenylphosphonium-DOX with a bromide counter anion, which was added to the silver salt of HA. The formation of AgBr precipitate drove the ion pairing of triphenylphosphonium-DOX with HA, producing HA-*ionic*-triphenylphosphonium-DOX, which could be selectively delivered to mitochondria.

Similar ionic bonding strategies can be used to incorporate imaging or therapeutic modality to HA-NPs. For example, Mohs and coworkers developed self-assembled HA-NPs modified with Gd³⁺ for magnetic resonance imaging ^{31, 32}. Diethylenetriaminepentaacetic acid (DTPA) was conjugated to HA, yielding HA-DTPA. Gd³⁺ was then complexed with DTPA moieties on HA-DTPA conjugate. Other chelation agent utilized includes tris(hydroxypyridinone) (THP) ³³.

1.3 Imaging applications of self-assembled HA-NPs

Self-assembled HA-NPs can selectively accumulate in the tumor microenvironment by the EPR effect and CD44 mediated cellular uptake. Many types of imaging functionalities can be incorporated into self-assembled HA-NPs, including probes for NIR imaging, CT imaging, photodynamic imaging, photoacoustic imaging (PA) and magnetic resonance imaging (MRI).

1.3.1 NIR imaging

NIR imaging is the most popular or common imaging functionality incorporated into self-assembled HA-NPs, primarily because of the ease of incorporating such functionality and the high

sensitivity of NIR imaging. As shown in **Table 1.1**, common fluorophores incorporated are Cy5.5, IR780, IR808, chlorin e6 (Ce6) and ICG.

Fluorophore	references
Cy5.5	14, 34-37
Ce6	16, 38, 39
ICG	40, 41
IR780	42-44
Cy7.5	31, 41
IR808	45

Table 1.1 Fluorophores incorporated in self-assembled HA-NPs.

In 2010, Jeong and co-workers conjugated cholanic acid and Cy5.5 to HA through amide bonds ³⁴. Cholanic acid and Cy5.5 formed the hydrophobic core of the self-assembled NPs. When HA-NPs were administered by intravenous injections, significant accumulation of HA-NPs was observed at tumor sites in mouse skin cancer SCC7 bearing mice. Similar design has been used in other reports ^{14,36}. In a follow up study, Jeong and co-workers chemically conjugated PEG to HA-ceramide conjugate through amide bonds ³⁵. *Ex vivo* imaging of HA-NPs after injection into mice demonstrated that PEGylation of HA-NPs significantly reduced liver uptake and increased the blood circulation time of HA-NPs. Meanwhile, compared with HA-NPs, PEGylated HA-NPs showed higher accumulation at tumor sites.

Ce6, an FDA approved photosensitizer for photodynamic therapy, can also be used for NIR imaging ^{16, 38, 39}. For example, in 2019, Luan and coworkers developed self-assembled HA-NPS where DOX and Ce6 were both covalently conjugated to HA. HA was first modified with ADH and then conjugated with DOX through a hydrazone linkage ⁴⁶. Ce6 was conjugated to HA-ADH

through amide bonds. The resulting HA-NPs were multifunctional: pH-responsive drug release, NIR imaging, and photodynamic therapy. IR780 and other dyes that are frequently used for photothermal therapy can also be used for NIR imaging ⁴²⁻⁴⁵. For example, Kim and coworkers developed self-assembled HA-NPs functionalized with IR780 and polypyrrole for combined photothermal and photodynamic therapy, and for NIR imaging ^{44, 47}.

In 2016, Mohs and coworkers developed self-assembled HA-NPs functionalized with ICG or Cy7.5 ⁴¹. The preparation of such HA-ICG was accomplished by self-assembly of HA-aminopropyl-1-pyrenebutanamide (HA-PBA) and ICG. Mice bearing orthotopic 4T1 breast cancer tumors ⁴¹ or pancreatic cancer ⁴⁰ were used for *in vivo* evaluation. Compared with ICG, HA-ICG showed much better tumor contrast when administered in mice, which helped mark the tumor boundary and direct surgical resection. Similarly, HA-Cy7.5 NP also gave higher tumor contrast compared to Cy7.5 alone in tumor bearing mice. This demonstrated the potential for using HA as a carrier of NIR dye for image-guided surgery.

1.3.2 MRI imaging

To enable MRI using self-assembled HA-NPs, contrast agents such as gadolinium (Gd^{3+}) need to be incorporated into the NPs. This can be achieved by conjugating a chelation agent such as diethylenetriaminepentaacetic acid (DTPA) to HA. In 2002, Winnik and coworkers developed self-assembled HA-NPs by covalently conjugating DTPA to HA *via* amide formation, followed by chelation of Gd^{3+} ⁴⁸. These HA-Gd NPs were used as a lymphatic system-specific MRI contrast agent ⁴⁹. In 2012, Kim and co-workers developed self-assembled HA-NPs enabling both NIR and MRI ⁵⁰. Cy5.5, HA-ceramide and DTPA were covalently conjugated to HA. Gd^{3+} chelation was accomplished via DTPA- Gd^{3+} interactions. *In vitro* cytotoxicity and cellular uptake were evaluated using two cell lines: U87-MG (low expression of CD44) and SCC7 (high expression of CD44)

cells. The cellular uptake efficiency of the HA-CE-based nanoprobe was higher in SCC7 cells than in U87-MG cells, indicating the importance of HA-CD44 interaction. The tumor targetability and MR contrast enhancement by the developed imaging nanoprobe were verified in a tumor xenograft mouse model using SCC7 cells.

In 2015, Jeong and coworkers developed HA-conjugated gadolinium (HA-diethylene triamine pentaacetic acid (DTPA)-Gd) and evaluated its ability for hepatocyte-specific MRI to diagnose hepatic metastasis ³². DTPA was first conjugated to HA *via* carboxylic ester linkages. Gd³⁺ was then allowed to be complexed with DTPA. FL83B and NIH3T3 cells were prepared for cytotoxicity testing. Normal mice (Balb/c mice) and hepatic tumor metastasis mouse model were used for *in vivo* MRI. Their study investigated T1 relaxation-based MR contrast property of HA-DTPA-Gd for MRI of hepatic metastases. The presence of HA amplified the water exchange rate on gadolinium molecules, inducing strong T1 relaxivity. HA-DTPA-Gd had a higher efficiency in liver MRI compared with the commercially available liver-specific contrast agent ($p < 0.001$). HA-DTPA-Gd, which possessed a higher T1 relaxivity, showed excellent capability for the diagnosis of hepatic metastasis through an *in vivo* MRI study in comparison with the commercially available gadoxetic acid ($p < 0.001$). HA-DTPA-Gd possessed excellent contrast enhancement of normal hepatic parenchyma with good signal to noise ratio of hepatic metastasis in the delayed liver MRI. In 2015, Zhang and coworkers developed a self-assembled HA chitosan NP as MRI contrast agents ⁵¹. DTPA was grafted to chitosan *via* amide formation promoted by a carbodiimide. Chitosan-DTPA-Gd was then complexed with HA by ionic gelation. HA induced signal enhancement was observed both *in vitro* and *in vivo*. HA-NPs showed prolonged retention in B16 tumor-bearing mice model. Overall, they demonstrated the feasibility of HA-NPs as an MRI contrast agent for tumor diagnosis.

1.3.3 Multimodal imaging

Multimodal imaging incorporates two or more imaging modalities into one construct. As each modality can have its intrinsic advantages and disadvantages, by combining results from multiple modalities enabled by a single construct, one can quickly acquire complementary information, which can help confirm the imaging results and provide more insights on the system being investigated. **Table 1.2** shows various moieties that can be conjugated to HA for multimodal imaging.

references	functionalities	Imaging modalities
45	IR808	PA, NIR
52	Cy5.5	PA, NIR
53	ICG	PA, NIR
16, 54	Ce6	PA, NIR
55	Ce6, Gd ³⁺	NIR, MRI
31	Gd ³⁺ , Cy7.5	PA, MRI
26	Gd ³⁺ , Cy7.5	NIR, MRI
37	2,3,5-Triiodobenzoic acid (TIBA) and Cy5.5	CT, NIR

Table 1.2 Self-assembled HA-NPs for multi-modality imaging.

Combining NIR and PA. In 2014, Zhu and coworkers developed self-assembled HA-NPs functionalized with copper sulfide (CuS) for photothermal therapy ⁵². CuS was loaded into Cy5.5-conjugated HA-NPs by a high-pressure homogenizer, yielding an activatable Cy5.5 HA-NPs/CuS nanocomposite. In this system, Cy5.5 fluorescent signals were quenched by CuS inside the particles until the whole nanocomposite was degraded by hyaluronidase present in tumor, turning on strong fluorescence signals delineating the tumor. CuS with strong NIR absorbance appears to

be an excellent contrast agent for PA imaging and an effective PTT agent. Ohe and coworkers developed self-assembled HA-NPs for NIR and PA imaging ⁵³. ICG and polyethylene glycol (PEG) were grafted to HA through amide coupling and CuAAC reactions. The conjugate formed self-assembled NPs, in which the near-infrared dyes were tightly packed and arranged to form dimers or H-aggregates. By irradiating an aqueous solution of the conjugate with NIR, photoacoustic signals were detected along with fluorescence emission. Self-assemblies consisting of HA conjugate could accumulate in tumor tissues by active targeting due to HA-CD44 mediated interactions. In 2016, Cai and co-workers explored the possibility of using Ce6 for PA imaging enabled by HA-NPs ¹⁶. They subsequently proposed self-assembled HA-NPs for PTT, and for NIR and PA imaging enabled by the incorporation of a biocompatible cyanine dye IR808 ⁴⁵.

Combining NIR and MRI. In 2017, Mohs and coworkers developed self-assembled HA-NPs with NIR and MRI functionality ³¹. HA was first modified with aminopropyl-1-pyrenebutanamide (PBA). Cy7.5 was conjugated *via* amide formation through the carboxyl groups on the polymer chain. Diethylenetriaminepentaacetic (DTPA) dianhydride then reacted with HA-PBA to produce HA-PBA-DTPA, followed by Gd³⁺ complexation to yield paramagnetic HA-PBA-DTPA-Gd. Imaging efficacy was evaluated in a human breast tumor xenograft model in nude mice, which demonstrated contrast in both fluorescence and MRI. Similar design of combining MRI and fluorescent imaging for HA-NPs was used by Torino and coworkers. The synthesis was conducted in a microfluidic platform, incorporating HA, PEG crosslinking agent, Gd for MRI imaging, and ATTO 488 for fluorescence imaging ²⁶. In 2017, Lim and coworkers developed self-assembled HA-NPs with NIR, MRI imaging functionalities for photodynamic therapy ⁵⁵. Ce6 dyes were encapsulated into poly(lactic-co-glycolic acid) nanoparticles (PLGA-NPs) coated with HA for CD44 targeting. The abundant carboxylate groups of HA also enabled the chelation of Gd³⁺ on

the surface of PLGA-NPs for T1-weighted MRI. These HA-NPs could efficiently target CD44-overexpressing A549 cancer cells. When an NIR laser was illuminated to irradiate A549 tumor-bearing mice, the groups treated with HAGCP-NPs showed remarkable delays in tumor growth or tumor regression. Taken together, these HA-NPs are a promising theranostic platform for the dual modality (MRI/NIR) imaging and PDT of cancer.

Combining NIR and CT. In 2016, Kim and coworkers developed self-assembled HA-NPs where 2,3,5-triiodobenzoic acid (TIBA) and Cy5.5 were conjugated to an HA oligomer as a CT imaging modality and the hydrophobic core for the self-assembled NP ³⁷. DOX was encapsulated into HA-NPs through solvent evaporation. Cellular uptake based on the interaction between HA and the CD44 receptor improved the cytotoxicity of DOX in SCC7 cells. The *in vivo* tumor targetability of the HA-TIBA nano-assembly was also verified by NIRF and CT imaging. The ability to selectively target tumor provided improved antitumor efficacies in SCC7 tumor-xenografted mice following intravenous injection of HA-TIBA/DOX.

Combining SPECT and CT. In 2017, Al-Jamal and coworkers developed self-assembled HA-NPs with single photon emission computed tomography (SPECT) /CT imaging capabilities ³³. HA was conjugated, *via* amide coupling, to Gemcitabine (Gem), 4'-(aminomethyl)fluoresceine hydrochloride (HA-4'-AMF) or tris(hydroxypyridinone) amine (HA-THP) for cancer therapy, *in vitro* tracking and SPECT/CT imaging, respectively. Tris(hydroxypyridinone) (THP) has been reported to offer instant and stable chelation with gallium radiometals, providing an attractive labelling approach for Positron Emission Tomography (PET) (⁶⁸Ga) and SPECT (⁶⁷Ga) imaging. Gem is a bifluorinated deoxycytidine analog prodrug, which internalizes into cells *via* the human equilibrative nucleoside transporter-1 (hENT1). *In vitro* cytotoxicity was evaluated in PANC-1, PANC-0403, CT26, B16-F10 and MDA-MB 435 cell lines. *In vitro* cellular uptake was evaluated

in CT26 cells. *In vivo* uptake of HA-NPs following i.v. injection was examined firstly by 3D whole body SPECT/CT imaging. This was the first study reporting SPECT imaging of cancer using HA as a macromolecular drug conjugate. Furthermore, the use of THP, a Gd^{3+} chelator, added to the attractiveness of the approach as both SPECT (long-lived isotopes for pharmacokinetic studies) and PET (short-lived isotopes for clinical imaging studies) imaging could be performed. The fluorescently labelled conjugate provided information on the possible cell entry mechanisms employed in both CT26 and PANC-1 cells *in vitro*. Gamma scintigraphy and *in vivo* live imaging studies described the quantities of HA that reached the tumor, establishing the correlation between NP concentrations in tumor and therapeutic efficacy.

1.4 Therapeutic application of self-assembled HA-NPs

There are many intrinsic advantages of using self-assembled HA-NPs for the delivery of small molecule drugs. Most of small molecule drugs have limited aqueous solubility, which could lead to poor cellular uptake. By encapsulating these drugs into self-assembled HA-NPs, it would be easier to solubilize the drugs ⁵⁶. Meanwhile, the inherent targeting ability of HA toward CD44 can help to bring the drug to tumor microenvironment and facilitate drug uptake by tumor cells. One concern about this strategy is that the drug may lose its biological activity after conjugation to HA. To overcome this, one common approach is to conjugate the drug to HA through a cleavable linker such as a carboxylic ester, hydrazone or disulfide linkage. The linker could be readily cleaved in the tumor microenvironment, and the free drug could be released from the NPs exerting its cytotoxicity ^{57, 58}.

Most anti-cancer drugs were encapsulated into HA-NPs through hydrophobic-hydrophobic interactions rather than covalent conjugation for several reasons. First, most anti-cancer drugs do not have a carboxyl group or amine group that can be readily used for covalent conjugation. Second,

even if they have such functional groups, chemical conjugation may significantly decrease its biological activity, if a cleavage mechanism is not built in the design. Third, complexation through hydrophobic-hydrophobic interaction is a relatively facile process, and good loading efficiency can usually be achieved. **Tables 1.3** shows different hydrophobic moieties that have been used for self-assembly.

Hydrophobic moiety	references
Ceramides	14
PLGA	24, 59, 60
Poly(γ -benzyl L-glutamate) (PBLG)	18, 61
Poly(lactic acid (PLA)	62-64
Histidine	65, 66
Testosterone	56
2,3,5-Triiodobenzoic acid (TIBA) and Cy5.5	37
n-octyl acrylate	67
Cholanic acid	37, 68
Poly(maleic anhydride-alt-1-octadecene)	42
Chitosan	69
Ce6	46
Glycyrrhetic acid (GA)	70
Deoxycholic acid (DOCA)	71
Vitamin E succinate (VES)	72
Folic acid	73

Table 1.3 Common hydrophobic moieties for self-assembled HA-NPs.

This section is divided by different therapeutic applications of self-assembled HA-NPs, including tumor targeted drug delivery, photothermal therapy, gene delivery, anti-inflammatory drug delivery, and protein delivery.

1.4.1 Delivery of small molecules to enhance therapeutic efficacy

Doxorubicin (DOX). DOX is a traditional anti-cancer drug frequently used in chemotherapy ⁵⁶, which can lead to apoptosis of tumor cells by damaging DNA or inhibiting the topoisomerase. It is the most popular drug being delivered by self-assembled HA-NPs, accounting for about 25% of the reported work using self-assembled HA-NPs for cancer treatment. Various techniques have been adopted to bestow the resulting self-assembled HA-NPs other desirable properties, including pH responsiveness and the abilities to function as contrast agents. The discussion is divided according to the types of agents used to facilitate the formation of HA-NPs.

Triphenylphosphonium. In 2018, Gao and coworkers developed self-assembled HA-NPs functionalized with Triphenylphosphonium (TPP)ion ⁵⁷. TPP can be used to target mitochondria, since it is highly lipophilic and cationic and thus can be easily taken up by mitochondrial membrane. DOX was conjugated to TPP, and then an ADH linker was installed through the hydrazone linkage, yielding ADH-DOX-TPP, which was subsequently conjugated to HA through amide bonds. However, due to its amphiphilicity, TPP-DOX was difficult to be physically entrapped in nanocarriers. In 2018, Gao and coworkers developed another kind of self-assembled HA-NPs functionalized with TPP ³⁰. TPP-DOX was conjugated to HA by an ionic bond, using silver nitrate as an activating agent. The HA nanocarriers (HA-ionic-TPP-DOX) were shown to self-assemble into spherical nanoparticles, which exhibited sensitivity to acidic pH in terms of morphology and drug release. Compared with the free DOX, HA-ionic-TPP-DOX produced much greater intracellular DOX accumulation and mitochondrial localization, leading to increased ROS production, increased cytotoxicity in MCF-7/ADR cells, and enhanced tumor targeting *in vivo*.

Ceramides. Ceramides (CEs) are a family of lipid molecules that are composed of sphingosine and a fatty acid. CE can act as a cellular signaling molecule to regulate the

differentiation, proliferation, and apoptosis of cells. Kim and coworkers developed self-assembled HA-NPs functionalized with CEs and DOX for the treatment of melanoma²⁰. A CE molecule was first conjugated to HA through an ester linkage, yielding the HA-CE conjugate. In a follow-up study in 2012, aminated PEG was added to HA-CE NP *via* amide bonds to prolong the circulation time of NPs in the bloodstream (as shown in **Figures 1.4** and **5**), which led to lower clearance of DOX and enhanced drug delivery efficiency¹⁴.

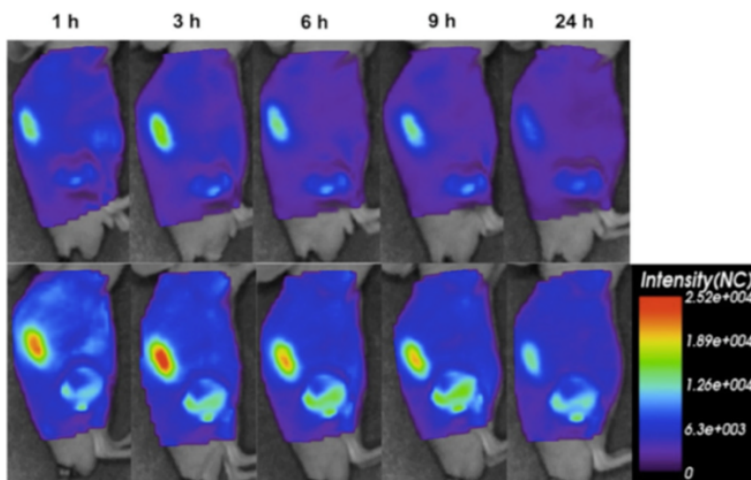


Figure 1.4 PEGylation helped to prolong in vivo circulation of HA-NPs. In vivo NIRF imaging in SCC7 tumor-bearing mouse after intravenous injection of DOX-loaded HACE and HACE-PEG nanoparticle. PEGylated HA-NPs lasted longer in vivo. This figure is reproduced with permission from Elsevier publisher¹⁴.

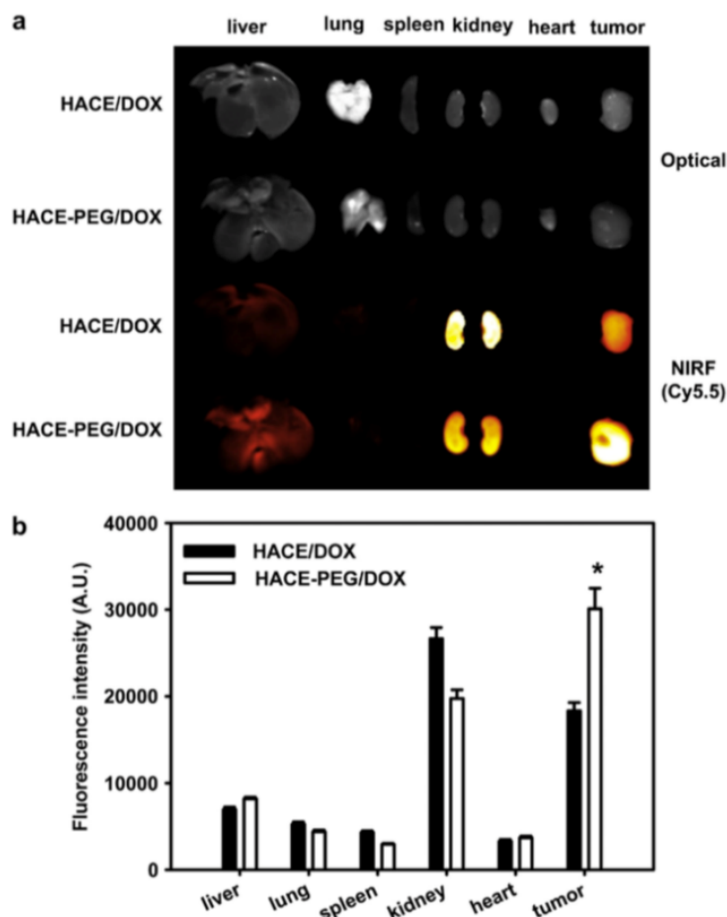


Figure 1.5 Ex vivo NIRF imaging 1-day post-injection of nanoparticles showed that PEGylated HA-NPs accumulated more in tumor: a) Optical and Cy5.5 filtered images of excised organs and tumors; b) fluorescence intensity values. This figure is reproduced with permission from Elsevier publisher¹⁴.

Hydrophobic polymers. Hydrophobic polymers could be used as the hydrophobic core for NP formation. PLGA was a common polymer utilized. Park and coworkers developed self-assembled HA-NPs, where PLGA was covalently conjugated to HA through ester linkages, and DOX was encapsulated through hydrophobic-hydrophobic interaction⁵⁹. Jeong and coworkers developed self-assembled HA-NPs in which PLGA was covalently conjugated to HA through amide linkages⁶⁰. Lee and coworkers also used PLGA but employed a different design. Rather than using the carboxyl group of HA for an ester or amide linkage to PLGA, they used the reducing

end of the HA polysaccharide to install a disulfide linkage²⁴. DOX was then incorporated using the solvent exchange method. In this way, DOX release could be facilitated under a reducing environment.

Besides PLGA, other polymers studied included poly(γ -benzyl L-glutamate) (PBLG) and polylactic acid (PLA). In 2009, Lecommandoux and coworkers developed self-assembled HA-NPs in which PBLG was conjugated to HA *via* the CuAAC reaction with an alkyne linker installed at the reducing end through the reductive amination reaction^{18, 61}. DOX was encapsulated subsequently *via* the nanoprecipitation method. The Giammona group developed self-assembled HA-NPs in which PLA was conjugated to HA *via* an ester linkage⁶⁴. PLA conjugation rendered HA-NPs responsive to pH value changes. The conjugation of PLA with HA could also be achieved through reductive amination⁶² or ring opening polymerization reaction with lactide⁶³.

Histidine. With its aromatic imidazole ring in the side chain, the histidine residue is hydrophobic in its free base form. In an acidic environment, such as tumor tissue (pH 6.5–7.0), endosomes (~pH 6) and lysosomes (~pH 5) in tumor cells, the nitrogen atom in the imidazole ring of histidine can become protonated leading to significantly increased hydrophilicity of the residue. The ability to absorb protons from the media (referred to as the proton sponge effect) of histidine can promote the disruption of endosomes resulting in the release of endosomal content to the cytoplasm. Huang and coworkers developed self-assembled HA-NPs where histidine was conjugated to HA by carbodiimide mediated coupling as the hydrophobic core⁶⁵. Tian and coworkers developed self-assembled HA-NPs where polyhistidine was conjugated to HA through amide bonds⁶⁵. Chen and coworkers incorporated histidine into self-assembled HA-NPs for pH responsive release using a non-covalent approach. They modified HA and PEI with histidine respectively. The resulting polyion formed complexes through electrostatic interactions between

histidine modified HA and histidine modified PEI. Similar design was utilized by Lee and coworkers in 2019 ⁶⁶.

Metal-phenolic network (MPN). In 2019, Park and coworkers developed self-assembled HA-NPs coated with MPN ⁶³. This MPN coating by tannic acid and FeCl₃ could be readily dissolved in an acidic environment, enabling pH responsive drug release in tumor environment.

Mineralization. Park and co-workers employed a mineralization strategy to enable pH responsive drug release from self-assembled HA-NPs ³⁷. PEG was covalently conjugated to HA, with DOX encapsulated during the self-assembly process. The resulting NPs were mineralized through controlled deposition of inorganic calcium and phosphate ions on the nanoparticulate shell *via* a sequential addition method, forming a Ca₃(PO₄)₂ layer on the surface of HA-NPs. This cap layer could readily disassemble in a mildly acidic environment, which led to an accelerated release of DOX.

Theranostic NPs. To aid in detection and tracking of the HA-NPs, imaging agents could be incorporated into HA-NPs. The most common imaging method utilized in self-assembled HA-NPs is NIR imaging facilitated by cyanine dye. Most NIR dyes have poor aqueous solubilities. Conjugation of NIR dye with HA can alleviate the solubility issue, leading to better imaging sensitivity. NIR imaging has a high sensitivity and the dye conjugation could be achieved through the carboxyl group on HA. In 2016, Kim and coworkers developed self-assembled HA-NPs where 2,3,5-triiodobenzoic acid (TIBA) and Cy5.5 were conjugated to HA with DOX encapsulated in the hydrophobic core, for chemotherapy and dual modality imaging (NIR and CT) ³⁷. In 2019, Costa and co-workers developed HA-NPs functionalized with poly(maleic anhydride-alt-1-octadecene), followed by encapsulation of IR780 for NIR imaging and DOX through the nanoprecipitation method ⁴². Park and coworkers developed HA-NPs as carriers for anticancer

drugs including DOX and camptothecin (CPT). In their self-assembled HA-NPs, cholic acid and Cy5.5 were conjugated to HA as the hydrophobic core for NIR imaging ⁶⁸. In 2019, Luan and coworkers developed HA-NPs where DOX and Ce6, an FDA approved photodynamic molecule, were both covalently conjugated to HA. HA was first modified with ADH and then conjugated with DOX through a hydrazone linkage ⁴⁶. The resulting self-assembled HA-NPS could serve as PA and NIR imaging agents.

Paclitaxel (PTX). PTX is a widely used chemotherapeutic drug in the clinics. It is another common drug applied in self-assembled HA-NPs. Various linkage can be employed for PTX delivery, as shown in **Table 1.4**.

Types	Linkage	References
DOCA	Disulfide	23, 74
HA-PTX conjugate	Ester	21
HA-PTX conjugate	acetal	19
vitamin E succinate	disulfide	75
Chitosan	-	59, 76

Table 1.4 Self-assembled HA-NPs for tumor targeted delivery of PTX.

In 2011, Zhang and coworkers developed self-assembled HA-NPs, in which deoxycholic acid (DOCA) was covalently conjugated to HA *via* a disulfide linkage, and PTX was incorporated in the hydrophobic core ²³. The HA-DOCA micelles were demonstrated to be an effective approach for the rapid transport of PTX into the cytosol. It showed improved antitumor efficacy against MDA-MB-231 cells compared with PTX alone.

In 2013, Deng and coworkers reported the strategy of using HA chitosan NP for oral delivery of PTX ⁷⁶. Oral administration is the most convenient method for drug administration

especially for chronic therapies. It eliminates the pain and possible infections caused by injections. PTX was first conjugated to HA through an ester linkage promoted by dicyclohexyl carbodiimide (DCC). The HA-PTX conjugate was then mixed with chitosan, which self-assembled into NPs. In 2014, Dong and coworkers developed another self-assembled HA chitosan NP for oral delivery of PTX ⁵⁹. PTX was similarly conjugated with HA through an ester linkage followed by attachment with polycaprolactone (PCL). PCL is a biodegradable hydrophobic moiety and was widely used in the construction of amphiphilic copolymer NPs for anti-cancer drug delivery. The *in vitro* release of PTX was pH-responsive, suggesting that chitosan/HA-paclitaxel (HA-PTX NPs) could prevent the breakage of the ester bond in HA-PTX NPs in acidic pH conditions. HA-PTX NPs exhibited higher cellular uptake than free PTX against HepG2 cells *via* receptor-mediated endocytosis. PTX could accumulate remarkably into tumor sites after oral administration of HA-PTX NPs. These results indicate that the HA-PTX NPs drug delivery system has a great potential for applications in the oral administration of hydrophobic drugs.

In 2016, Haag and coworkers developed self-assembled HA-NPs delivering PTX (**Figure 1.6**). PTX was covalently conjugated to HA *via* an acetal linkage ¹⁹, which enabled pH sensitive drug release with accelerated release of PTX observed at endosomal acidic pH (pH = 5.0) compared with physiological pH (pH = 7.4). In 2018, Park and coworkers developed HA-NPs in which PTX was covalently conjugated to HA through an ester linkage ²¹. PEG was added during the self-assembly process. In 2018, Lai and coworkers developed self-assembled HA-NPs in which vitamin E succinate was covalently conjugated, and PTX was loaded through a disulfide linkage for redox-sensitive drug release ⁷⁵. In 2020, Sun and coworkers reported self-assembled HA-NPs conjugated with PEG, deoxycholic acid, and *N*-acetyl-L-cysteine (NAC) *via* amide formation ⁷⁴. NAC, a derivative of cysteine, contains free thiol groups (-SH). The disulfide bonds from NAC

crosslinking could be cleaved in the presence of high concentration of GSH in the tumor, leading to the dissociation of the NP and the release of the drug.

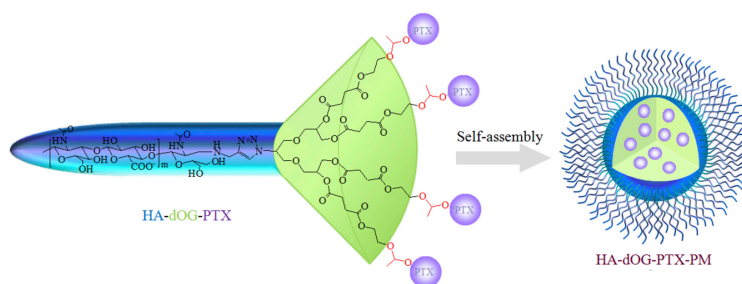


Figure 1.6 pH responsive HA nanoparticles. Acetal linkage enables pH sensitive drug release. This figure is reproduced with permission from Elsevier publisher ¹⁹.

Docetaxel (DTX). DTX is a semi-synthetic derivative from the *Taxus brevifolia* family. DTX can inhibit the depolymerization of microtubules and M-phase cell arrest ⁷⁷. Docetaxel has shown clinical efficacy against various cancer, including breast cancer and ovarian cancer.

In 2000, Prestwich and coworkers developed self-assembled HA-NPs, in which DTX was conjugated to HA *via* ester linkages ⁷⁸. In 2011, Kim and coworkers developed HA-NPs with DTX encapsulated in the hydrophobic core ¹⁴. HA was first converted to tetrabutyl ammonium salt to allow for its solubility in organic solvents, which was then coupled to CE and Cy5.5. Cy5.5 labelled HA-CE conjugate, DTX and Pluronic 85 (P85) were mixed together to form HA-NPs for theragnostic applications.

In 2016, Zhong and coworkers developed self-assembled HA-NPs functionalized with docetaxel, vitamin E, and oligo-(methyl diglycol L-glutamate) ⁷⁹. Vitamin E was covalently conjugated to oligo-(methyl diglycol L-glutamate) through a disulfide linkage, yielding VE-SS-OEG. VE-SS-OEG provides not only amino groups on NP surface to facilitate HA coating through electrostatic interactions, but also redox sensitivity to facilitate decoating and drug release within cancer cells. *In vitro* drug release study demonstrated that DTX release was

significantly accelerated in the presence of 10 mM glutathione. In 2016, Dinarvand and coworkers developed a self-assembled HA chitosan NP functionalized with DTX ⁷⁷. DTX was first encapsulated with HA and the resulting HA-DTX was mixed with chitosan. 4T1 and MCF-7 breast cancer cells were used to evaluate *in vitro* drug release and cytotoxicity. The result showed that this HA chitosan NP significantly increased the availability and the efficacy of DTX *in vitro*.

Multi-drug resistance (MDR) is a big hurdle for effective cancer treatment. In 2018, Shen and coworkers developed self-assembled HA-NPs functionalized with PLGA, PEI, α -naphthoflavone (ANF) and DTX to address this issue by targeting CYP1B1 ⁸⁰, one of the CYP450 enzymes mainly existing in extrahepatic tissues. CYP1B1 is overexpressed in tumor tissue, but has no or extremely low levels of expression in normal tissues, and is related to MDR in tumor treatment as it can metabolize DTX significantly reducing its efficacy. The CYP1B1 usually weakens the therapeutic effect of DTX in tumors where CYP1B1 has strong expression. ANF is a CYP1B1 inhibitor, which can reduce the expression of CYP1B1 and enhance the sensitivity of tumor cells toward DTX. The synthesis of the NPs was through the self-assembly of PLGA with PEI, ANF and DTX. With the surface being positively charged, HA was conveniently attached through electrostatic interactions. The HA-ANF-DTX NPs effectively alleviated the MDR effect. They demonstrated that the HA/PEI NPs could reverse MDR effectively by downregulating the expression of CYP1B1.

5-Fluorouracil (5-FU). 5-FU, a pyrimidine analog, can interfere with thymidylate synthesis. In 2010, Agrawal and coworkers developed self-assembled HA-NPs modified with PEG, PLGA and 5-FU ⁸¹. In 2017, Shi and coworkers developed a self-assembled HA chitosan NP with 5-FU encapsulated in the hydrophobic core ⁸². A549 cells (with high CD44 expression) and HepG2 cells (with low CD44 expression) were used to evaluate cellular uptake and cytotoxicity. The result

demonstrated that this self-assembled HA-NP could effectively deliver 5-FU into CD44 overexpressing cells and more potently led to cell apoptosis.

Camptothecin (CPT). CPT inhibits DNA replication and cell proliferation by forming a ternary complex with DNA and topoisomerase I. CPT demonstrates effective activities against various types of cancers as well as the hepatitis C virus. Encapsulation of CPT into self-assembled HA-NPs can help improve its limited solubility and stability at physiological pH ⁵⁶. In 2011, Park and coworkers developed self-assembled HA-NPs with cholanic acid, Cy5.5 and PEG *via* amide formation. CPT was conveniently encapsulated in the HA-NPs through solvent exchange from DMSO to water ⁶⁸. SCC7 and MDA-MB-231 cancer cell lines (high CD44 expression) and normal fibroblast NIH-3T3 cell lines (low CD44 expression) were used for cellular uptake and cytotoxicity studies of these HA-CPT NPs. Enhanced cellular uptake was observed in SCC7 and MDA-MB-231 cells, compared with NIH-3T3, suggesting the uptake was CD44 mediated. Another report of HA-NPs using CPT was Ossipov in 2018⁵⁶. CPT was encapsulated in HA-testosterone conjugates through hydrophobic-hydrophobic interactions.

Cisplatin (cis-Pt). cis-Pt can form an adduct with DNA resulting in cell apoptosis ⁸³. In 2008, Jung and coworkers developed self-assembled HA-NPs by incubating HA with cisplatin to form NPs *via* chelation of HA with the Pt ion ⁸⁴. In 2017, Kurisawa and coworkers developed self-assembled HA-NPs functionalized with epigallocatechin-3-*O*-gallate (EGCG) and cisplatin, for the treatment of ovarian cancer ⁸⁵. EGCG is the most abundant catechin in green tea, which can interrupt key signaling and metabolic pathway vital to cancer cell survival, leading to cell apoptosis. There are increasing interests of EGCG as a potent adjuvant in cancer therapy. EGCG was conjugated to HA at the reducing end as the hydrophobic core. Cisplatin was encapsulated during the self-assembly process. When evaluated in tumor bearing mice, these HA-NPs was found to

prolong the circulation time of EGCG and cisplatin in mice with significantly enhanced accumulation of NPs in tumor sites, leading to better overall therapeutic effect.

In 2019, Shen and coworkers developed self-assembled HA-NPs functionalized with Sorafenib (an FDA approved drug) and cisplatin for the treatment of hepatocellular carcinoma. Sorafenib induces cell apoptosis via several different mechanisms. It can block some specific pathways such as Raf/MEK/ERK pathway, reduce eukaryotic initiation factor 4E phosphorylation, downregulate myeloid cell leukemia-1 levels in tumor cells, and inactivate vascular endothelial growth factor receptor-2. The preparation of these self-assembled HA-NPs was based on the chelation interaction between HA and cisplatin, and hydrogen bond interactions between HA and Sorafenib. Synergistic antitumor effect of cisplatin and Sorafenib was observed in HepG2 cells and HepG2-tumor-bearing mice.

Naringenin. In 2018, Saraf and coworkers developed self-assembled HA-NPs functionalized with poly caprolactone and Naringenin (NAR) ⁸⁶. NAR is a flavanone, which possesses anticancer, antimutagenic, anti-inflammatory, antiatherogenic, and antifibrogenic properties. NAR is reported to induce cytotoxicity and apoptosis in various cancer cell lines ⁸⁶. *In vitro* cytotoxicity and cellular uptake were evaluated using lung cancer cell line A549. Cell cycle arrest analysis with A549 cell line demonstrated the good cytotoxic effect and active targeting of HA-NPs functionalized with poly caprolactone and NAR. Further chemopreventive treatment with the NPs was found effective in tumor growth inhibitory effect against urethane-induced lung cancer in rats *in vivo*.

Norcantharidin. In 2018, Lv and coworkers developed self-assembled HA-NPs functionalized with galactosamine, Vitamin E succinate and Norcantharidin for the treatment of hepatic carcinoma ⁸⁷. Galactosamine could be selectively recognized by the asialo glycoprotein

receptor (ASGPR), which is highly expressed on the surface of hepatic cancer cells. Vitamin E succinate serves as a hydrophobic side chain and can inhibit multidrug resistance. In this way, the self-assembled HA-NPs were dual targeting to liver with HA and galactosamine serving as targeting molecules.

Deacetyl mycoepoxydience. In 2019, Wang and coworkers developed self-assembled HA-NPs for targeted delivery of deacetyl mycoepoxydience⁸⁸. PEG was conjugated to HA via carbodiimide promoted coupling. Deacetyl mycoepoxydience (DM) was then conveniently encapsulated *via* hydrophobic-hydrophobic interactions. MCF-7 cells were used to evaluate cytotoxicity *in vitro*. Pharmacokinetic studies in rabbits showed HA-NPs significantly increased the area under the plasma concentration-time curve (AUC), and elimination half-life ($t_{1/2}$), and reduced clearance rate (CL_z) compared to the DM solution for intravenous delivery. Results indicated that HA-NPs were successfully developed with higher stability improving the bioavailability of DM with a higher safety profile.

Atorvastatin. While most studies on self-assembled HA-NPs focused on tumor, inflammatory cells can be suitable targets as well since these cells express CD44 with high affinity toward HA under inflammatory conditions⁸⁹. In 2020, Huang group developed HA conjugated Atorvastatin (ATV) NPs for effective atherosclerotic plaque inflammation inhibition (**Figure 1.7**)¹⁵. ATV was first functionalized to introduce an amine group. Then aminated ATV was conjugated to HA through amide formation chemistry. The resulting HA-ATV-NPs exhibited significantly higher anti-inflammatory effects on macrophages compared to ATV alone *in vitro*. Furthermore, when administered in an apolipoprotein E (ApoE)-knockout mouse model of atherosclerosis following a 1-week treatment regimen, HA-ATV-NPs markedly decreased inflammation in advanced atherosclerotic plaques, which were monitored through contrast agent aided magnetic

resonance imaging. These results suggest CD44 targeting with HA-ATV-NPs is an attractive strategy to reduce harmful inflammation in atherosclerotic plaques.

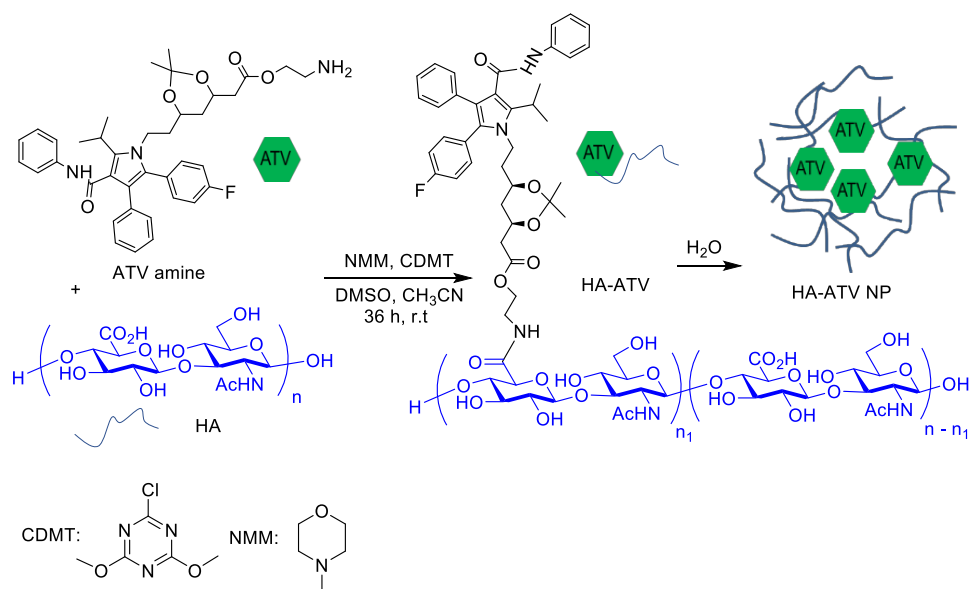


Figure 1.7 Preparation of HA conjugated atorvastatin NP. Aminated ATV was conjugated to HA via amide formation. This figure is reproduced with permission from Royal Society of Chemistry (RSC) ¹⁵.

1.4.2 Protein delivery

Besides small molecule therapeutics, protein cargo can be delivered by self-assembled HA-NPs. In 2010, Alonso and coworkers developed HA-chitosan NPs for the delivery of two pro-angiogenic growth factors: vascular endothelial growth factor (VEGF) and platelet derived growth factor (PDGF-BB) ⁹⁰. These NPs were prepared by an ionic gelification technique, and different formulations were developed by encapsulating the growth factors in association with two stabilizing agents: bovine serum albumin or heparin sodium salt. In 2012, Park and coworkers developed a platform for the delivery of carbonic anhydrase B (CAB) ⁹¹. CAB was physically encapsulated into HA-NPs by the dialysis method. The release rate of CAB could be tuned by the addition of hyaluronidase found in cytosol of cancer cells, suggesting the potential of HA-NPs for enzyme-triggered site-specific delivery of protein drugs. CAB released from HA-NPs retained

their biological activities, as demonstrated by the Nuclease Protection Assays. In 2018, Jeong and coworkers developed self-assembled HA-NPs functionalized with dopamine for the delivery of lysozyme. Dopamine-conjugated HA complexes were prepared by a one-pot synthesis through the self-polymerization of dopamine under oxidative, weakly basic conditions ⁹². The lysozyme was found to maintain its activities in the dopamine-conjugated HA. The presence of protein interaction and activity proved the capability of the dopamine-conjugated HA complexes as protein carriers.

1.4.3 Nucleic acid delivery

Non-viral methods for nucleic delivery are an attractive alternative to viral approaches due to its higher safety and low cost. Common non-viral gene delivery carriers include liposomes and cationic polymers. While liposomes as gene carriers have low immunogenicities and can be prepared easily, the liposomal approach is limited due to its low transfection efficiency, and instability in serum. Cationic polymers, such as PEI, can have significant toxic effects, which severely limited its use as a tool for gene delivery *in vivo*. A variety of HA-NPs has been investigated to deliver nucleic acids (**Table 1.5**). As nucleic acids are negatively charged under physiological conditions, a cationic compound is commonly added to the HA-NPs formulation to assist the incorporation of nucleic acids into the NPs.

Types	References
Chitosan	93-99
Polyethylenimine (PEI)	100-109
Hypericin	110
Spermine	111, 112
Poly-L-lysine (PL)	113
PLGA	7
Cyclodextrins (CDs)	114
HA-ASO conjugate	115

Table 1.5 Self-assembled HA-NPs for gene delivery.

Chitosan. In 2010, Alonso and coworkers developed self-assembled HA-NPs functionalized with chitosan, PEG for pDNA or siRNA delivery ⁹³. PEG was functionalized with a carboxyl group and conjugated to chitosan using carbodiimide-mediated amide formation. The self-assembly of HA-NPs was accomplished *via* ionotropic gelation between HA and PEGylated chitosan. In 2011, Lv and coworkers developed self-assembled HA chitosan NP for gene delivery targeting osteoarthritis ⁹⁴. HA/CS plasmid–DNA NPs were synthesized through the complex coacervation of the cationic polymers with pEGFP. In 2011, Ha and coworkers developed self-assembled HA-NPs functionalized with chitosan, tripolyphosphate and pDNA for gene delivery to spinal cord ⁹⁵. In 2013, Zhang and coworkers developed hybrid HA/chitosan/plasmid-DNA nanoparticles encoding transforming growth factor (TGF)-b1 ⁹⁶. In 2014, Zeng and coworkers used HA chitosan NP for co-delivery of MiR-34a and DOX ⁹⁷. MicroRNA-34a (miR-34a) is regulated by the p53 network at transcriptional level. It has been shown to be remarkably downregulated in a variety of cancers. miR-34a can potentially suppress tumor growth in breast cancer. miR-34a

was co-encapsulated with DOX into self-assembled HA-NPs for dual therapy. *In vitro* and *in vivo* experiments showed that miR-34a and DOX were efficiently encapsulated and delivered by HA-chitosan NP into tumor cells or tumor tissues. In 2013, Chen and coworkers developed oleoyl-carboxymethyl-chitosan (OCMCS)/HA-NPs using a coacervation process⁹⁸. An N/P ratio of 5 and OCMCS/HA weight ratio of 4 were the optimal conditions leading to the smallest (165 nm), positive charged (+14.2 mV) and monodispersed NPs. In 2016, Alonso and coworkers developed a self-assembled HA chitosan NP for ocular gene therapy⁹⁹.

Polyethylenimine. In 2012, Mikos and coworkers investigated a variety of factors that may affect the transfection efficiency of self-assembled HA-NPs functionalized with PEI^{100, 116}. The factors investigated included the effects of primary amines, ligand and charge, Zeta potential, cytotoxicity. The results showed that the length of HA has the most significant effect on cytotoxicity and transfection efficiency. Specifically, use of HA with ten monosaccharides in length significantly increased the transfection efficiency and decreased the cytotoxicity on human mesenchymal stem cells (hMSCs) *in vitro* as compared with formulations with shorter HA. Furthermore, the molar ratio of HA to PEI, as opposed to length, has the most significant effect on zeta potential, but minimal impact on both cytotoxicity and transfection efficiency. A medium level of primary amines incorporated into the NPs yielded higher transfection efficiency, whereas greater HA incorporation, and thus overall negative charge, lowered cytotoxicity.

In 2008, Hahn and coworkers developed self-assembled HA-NPs for VEGF siRNA delivery to tumor. PEI (MW = 25,000) was covalently conjugated to HA *via* amide bonds¹⁰¹. Electrostatic interaction between the negatively charged siRNA and the positively charged PEI of PEI-HA conjugate drove the formation of the self-assembled NPs. The complex had an average size of 21nm. In 2010, in a follow up study, they improved on this gene delivery platform to

address the issue of the inherent cytotoxicity of high MW PEI ¹⁰². Reducible PEI was synthesized by the crosslinking of low M.W. PEI (MW ~ 2,000) with cystamine bisacrylamide (CBA), which was then conjugated with HA. The cytotoxicity of HA-PEI conjugate appeared to be negligible likely due to the cleavage of di-sulfide bonds yielding low MW PEI. In 2010, Sun and coworkers developed another strategy to address the issue of high cytotoxicity of PEI ¹⁰³. The HA-PEI conjugate was produced *via* an imine reaction between periodate-oxidized HA and PEI. The resulting HA-PEI showed high protection of DNA from nuclease, better dissociation of DNA from the complex, and low cytotoxicity.

In 2013, Amiji and coworkers developed self-assembled HA-NPs based on PEI for CD44 mediated siRNA delivery to solid tumors ¹⁰⁴. HA was modified with monofunctional fatty amines, bifunctional fatty amines, and PEI *via* amide formation. PEI was found to exhibit the best gene silencing activity in cells. PLK1 or CTL siRNA was encapsulated *via* the electrostatic interaction. SSB/PLK1 siRNA encapsulated in HA-PEI/PEG nano-systems demonstrated dose dependent and target specific gene knockdown in both sensitive and resistant A549 lung cancer cells overexpressing CD44 receptors. More importantly, these siRNA encapsulated nanosystems demonstrated tumor selective uptake and target specific gene knock down *in vivo* in solid tumors as well as in metastatic tumors.

In 2016, Amiji and coworkers developed self-assembled HA-NPs in which miR-223 was encapsulated in HA-PEI conjugate, which was used to evaluate macrophages repolarization from pro-inflammatory M1 to anti-inflammatory M2 phenotype ¹⁰⁰. HA-PEI-miR-233 NPs were efficiently internalized by both J774A.1 macrophages and primary peritoneal macrophages. Importantly, *in vitro* transfection of macrophages with HA-PEI/miR-223 NPs produced higher miR-223 expression level in the cells than that with HA-PEI/pDNA-miR-223 NPs, which could

decrease iNOS-2 and increase Arg-1 expression level in LPS and IFN- γ stimulated J774A.1 and peritoneal macrophages. Following macrophage phenotype switch, transfection with HA-PEI/miR-223 NPs decreased the expression level of pro-inflammatory cytokines TNF- α , IL-1 β , and IL-6 and thus reduced inflammation in peritoneal macrophages caused by LPS. In 2019, Amiji and coworkers developed another type of self-assembled HA-NPs for pDNA delivery ¹⁰⁵. Aminated PEG and aminated PEI were conjugated to HA, yielding HA-PEG and HA-PEI, respectively. The HA-NPs was formed through electrostatic interactions by mixing HA-PEG, HA-PEI, and pDNA together.

In 2008, Koyama and coworkers developed self-assembled HA-NPs in which PEI was not conjugated to HA, but complexed with HA *via* electrostatic interaction ^{106, 117}. The ternary complexes with negative surface charge formed upon mixing pDNA with PEI and HA. After intratumoral or intravenous injection into the mice bearing B16 cells, which are known to express CD44 on the surface ^{117, 118}, this NP induced a much stronger gene expression than pDNA/PEI complex, demonstrating the importance of targeting ability bestowed by HA.

In 2016, Kurisawa and coworkers developed self-assembled HA-NPs modified with PEI and epigallocatechin gallate (EGCG) ¹⁰⁷. EGCG can bind with DNA and proteins *via* hydrogen bonding, π - π stacking and hydrophobic-hydrophobic interactions. Human colorectal carcinoma HCT-116 cells and human embryonic kidney HEK293 cells were used to evaluate gene transfection efficiency *in vitro*. HA-EGCG-PEI not only stabilized pDNA/PEI complexes *via* strong DNA-binding affinity of EGCG, but also facilitated their transport into CD44-overexpressing cells by receptor-mediated endocytosis. These ternary complexes demonstrated enhanced resistance to nuclease degradation and polyanion induced dissociation.

In 2015, Duan and coworkers developed self-assembled HA-NPs for MDR1 siRNA delivery ¹⁰⁸. MDR severely limits the efficacy of chemotherapy for ovarian cancer and many other types of cancer. A well-known mechanism of MDR is the overexpression of the MDR1 gene and the corresponding P-glycoprotein (Pgp). MDR1 siRNA-based strategies can be used to overcome the challenges of MDR. The HA-PEI/HA-PEG NP could deliver MDR1 siRNA along with paclitaxel to suppress the growth of ovarian cancer. The results showed that this self-assembled NP can efficiently deliver MDR1 siRNA into MDR ovarian cancer cells, leading to down-regulation of MDR1 and Pgp. Administration of HA-PEI/ HA-PEG/MDR1 siRNA NPs followed by paclitaxel treatment induced a significant inhibitory effect on the tumor growth, decreased Pgp expression, and increased apoptosis in MDR ovarian cancer mouse model.

In 2013, Gu and coworkers developed self-assembled HA-NPs functionalized with disulfides for a reduction-responsive de-shielding design. HA was modified with a disulfide containing linker between the carboxyl groups and the backbone of HA (HA-SS-COOH) ¹⁰⁹. HA-SS-COOH and unmodified HA were used to shield DNA/PEI polyplexes to form ternary complexes. HA-SS-COOH/DNA/PEI polyplexes showed an up to 14-fold higher transfection efficacy than those coated with unmodified HA. This indicates the effectiveness of the reduction-responsive de-shielding design. The dependence on HA was confirmed by the observation that the addition of free HA prior to HA-SS-COOH/DNA/PEI incubation inhibited the transfection of CD44 expressing HepG2 and B16F10 cells, while not impacting much on CD44 deficient NIH3T3 cells. *In vivo* study using tumor bearing C57BL/6 mice showed that the self-assembled HA-NPs resulted in high accumulation and luciferase expression.

In 2007, Park and coworkers developed self-assembled HA-NPS for antisense oligodeoxynucleotide (ASO) delivery ¹¹⁵. Green fluorescent protein (GFP) ASO was covalently

conjugated to HA *via* a disulfide linkage. Protamine was then complexed with HA-ASO conjugate to increase cellular uptake and enhance gene inhibition efficiency. HA-ASO/protamine complexes demonstrated higher cellular uptake compared with ASO/protamine. HA-ASO/protamine complexes also showed a comparable level of GFP gene inhibition to that of cytotoxic PEI/ASO complexes.

Tu and coworkers developed self-assembled HA-NPs functionalized with spermine for efficient receptor-mediated siRNA delivery ^{111, 112}. Spermine is a tetraamine involved in cellular metabolism and present in all eukaryotic cells. The degree of modification of spermine significantly affected the transfection efficiency of HA-spermine conjugate as a nucleic acid delivery carrier. HA-NPs with higher spermine content were associated with higher gene transfection efficacy.

In 2012, Ouahab and coworkers developed self-assembled HA-NPs functionalized with hypericin and siRNA *via* the emulsion-diffusion-evaporation method ¹¹⁰. Hypericin (Hy) is a lipophilic compound with very limited solubility in water, and high affinity toward hypoxic necrotic tissues in tumor. Hy mediated photodynamic diagnosis has recently gained much credence in the diagnosis of cancer since it can aid in intraoperative diagnosis of suspicious lesions and recognition of tumor margins, in addition to its ability to selectively accumulate in the cancer tissue.

In 2013, Haam and coworkers developed self-assembled HA-NPs for induction of gastric cancer cell death by RNA interference ¹¹³. Poly-L-lysine (PLL) was first synthesized by ring-opening polymerization followed by a deprotection process. The primary amine groups of PLL were functionalized by imidazole groups, bestowing the polymer pH responsive property around physiologically relevant pH values. The prepared ternary polyplexes have a negative surface charge of +24 mV and a size of approximately 100 nm at an N/P ratio of 5 with HA/PLL molar

ratio of 0.03. This ternary polyplexes showed high stability and no cytotoxicity, primarily due to the anchoring of HA on the surface of the NP.

In 2015, Li and coworkers developed HA conjugated cyclodextrin-oligoethylenimine star polymer for CD44-targeted gene delivery, as shown in **Figure 1.8**¹¹⁴. Cyclodextrins (CDs) are a series of natural cyclic oligosaccharides composed of 6–8 (α -1,4)-linked D-glucopyranose units. They are considered as non-toxic and non-immunogenic. Cyclodextrin was functionalized with oligoethyleneimine (OEI) and then conjugated to HA *via* reductive amination. The CD-OEI-HA polymer contained 6 arms of OEI (600 Da) and HA. This NP can effectively encapsulate pDNA to form NPs with sizes ranging from 100 to 200 nm at N/P ratios of 8 or higher.

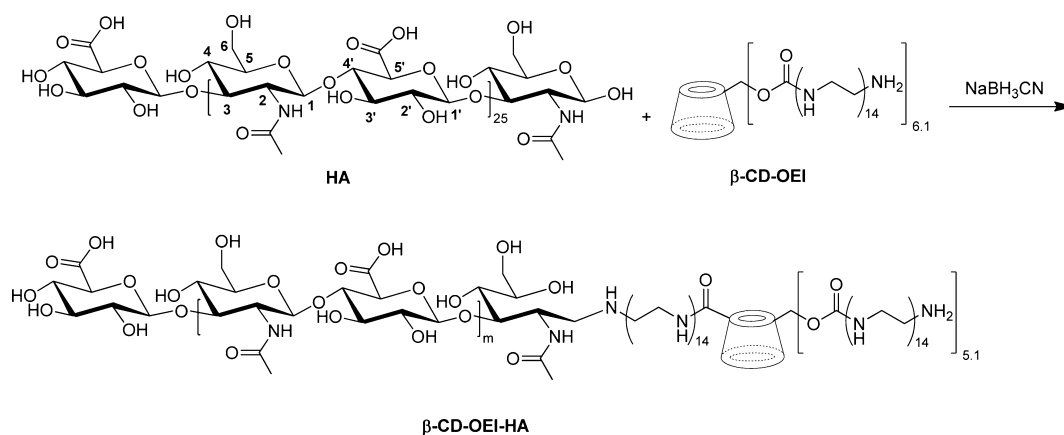


Figure 1.8 HA conjugated cyclodextrin-oligoethylenimine star polymer for CD44-targeted gene delivery. This figure is reproduced with permission from Elsevier¹¹⁴.

In 2017, Shieh and coworkers developed self-assembled HA-NPs conjugated with PLGA and PEG for gene delivery, comparing the efficacy of high and low MW HA in this setting⁷. PLGA and PEG were covalently conjugated to HA, and the conjugates were used to encapsulate pDNA for gene delivery. The cellular transfection efficacy of such micelles with high MW HA was much higher than of the micelles with low MW HA in CD44-positive cells. The specific and strong binding of high molecular weight HA to CD44-positive cells resulted in higher cellular transfection of high molecular weight HA-PEG-PLGA micelles in CD44-positive cells. The result

indicates that high MW HA is a better choice than low MW HA for gene delivery purposes at least for this experimental set up. However, this may not hold true in other delivery systems. For example, Mikos and coworkers investigated a variety of factors that may affect the transfection efficiency of self-assembled HA-NPs functionalized with PEI ¹¹⁶. HA with smaller molecular weight was found to be better for gene transfection. Thus, the effects of HA molecular weight should be carefully investigated.

1.4.4 Photodynamic therapy

In photodynamic therapy (PDT), cancer cells are killed through the generation of reactive singlet oxygen ($^1\text{O}_2$). Ce6 is the most common photosensor used in PDT, which is a second-generation photosensitizer activatable by NIR light. Moreover, it can be used as NIR fluorescence (NIRF) imaging dye in the spectral range of 650-900 nm to reduce the endogenous interference within the body and enhance the depth of tissue penetration. Other photosensitizers include pyropheophorbide ¹¹⁹, BFVPBT¹²⁰ and diketopyrrolopyrrole ¹²¹.

In 2012, Choi and co-workers developed self-assembled HA-NPs functionalized with Ce6 for photodynamic imaging and therapy ³⁹. Aminated 5 β -cholic acid, PEG, and black hole quencher3 (BHQ3) were conjugated to HA *via* amide linkages. During the self-assembly process, Ce6 was added for encapsulation into the NPs. BHQ3 effectively quenched the fluorescence of Ce6 and suppressed singlet generation by the photosensitizer. Meanwhile, upon release from HA-NPs, Ce6 allowed for simultaneous photodynamic imaging and therapy upon irradiation. The generation of singlet oxygen from Ce6 was quantitatively evaluated using *p*-nitrosodimethylaniline (RNO) as a singlet oxygen sensor. Ce6-HA-NPs were rapidly degraded in the hyaluronidase rich tumor environment. *In vivo* study showed that Ce6-HA-NPs could efficiently reach and accumulate in the tumor tissue *via* the EPR effect and CD44-mediated

endocytosis. Upon laser irradiation, Ce6 was released from the NPs, generating fluorescence and singlet oxygen inside tumor cells, resulting in effective suppression of tumor growth. In a follow up study in 2016, Cai and co-workers explored the possibility of using Ce6 for photoacoustic (PA) imaging with HA-NPs¹⁶. Ce6 possesses high potential PA activities due to its low fluorescence quantum yields. They reported a smart self-assembled HA-NP functionalized with Ce6 responsive to hyaluronidase. This HA-NP exhibited hyaluronidase-responsive “OFF/ON” behavior to fluorescence signals. *In vivo* study demonstrated that HA-CE-NPs achieved excellent NIR imaging and PA imaging functionalities with a 5-fold higher fluorescence intensity and 3-fold higher PA intensity than free Ce6 in tumor bearing mice, respectively. In addition, under a low dose of laser power, the HA-CE-NPs presented more effective photodynamic therapy to suppress tumor growth than free Ce6 both *in vitro* and *in vivo*.

In 2017, Zhu and coworkers reported self-assembled HA-NPs in which Ce6 was physically encapsulated into the hydrophobic core³⁸. In 2019, Luan and coworkers developed self-assembled HA-NPs where DOX and Ce6 were both covalently conjugated to HA. HA was first modified with ADH and then conjugated with DOX through a hydrazone linkage⁴⁶. Ce6 was conjugated to HA-ADH through amide bonds. *In vitro* and *in vivo* experiments were performed using B16 cells and BALB/C mice, respectively. The resulting HA-NPs were capable of pH-response, self-targeting delivery and NIR imaging-guided chemo-photodynamic therapy. The HA-NPs could dramatically improve the cellular uptake of drugs and enhance the therapeutic effects under laser irradiation with remarkably higher photostability.

In 2019, Zhao and coworkers developed catalase-integrated HA as nanocarriers (HA-CAT@aCe6) for enhanced photodynamic therapy in solid tumor, as shown in **Figure 1.9**¹²². *In situ* generation of oxygen using catalase as an enzyme is attractive because it is self-responsive to

hydrogen peroxide (H_2O_2) without the need for high local oxygen levels in the tissues. HA-CAT@aCe6 NPs showed high colloidal stability and monodispersity in aqueous solution. The encapsulated catalase could decompose the endogenous H_2O_2 to generate O_2 *in situ* for relieving hypoxia in cells incubated under hypoxic conditions. Cell viability assays indicated that HA-CAT@aCe6 NPs possessed minimal cytotoxicity in the dark, while presenting high cellular toxicity under 660 nm light irradiation at normoxic conditions. *In vivo* accumulation of HA-CAT@aCe6 NPs at tumor sites was observed in MDA-MB-231 tumor bearing nude mice. Significant tumor regression was observed after intravenous injection of HA-CAT@aCe6 NPs under light irradiation, compared with the control system without loading catalase.

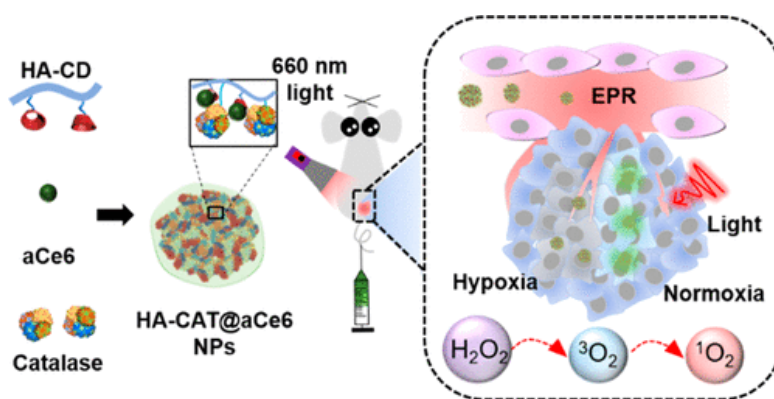


Figure 1.9 Catalase-integrated HA as nanocarriers (HA-CAT@aCe6 NPs) for enhanced photodynamic therapy in solid tumor. This figure is reproduced with permission from American Chemical Society (ACS) publisher ¹²².

In 2020, Fan and coworkers developed self-assembled HA-NPs functionalized with pyropheophorbide a (Ppa) and perfluorocarbons (PFCs) ¹¹⁹. HA was partially acetylated to prepare an amphiphilic HA polymer. PFCs served two roles: it helped to solubilize the photosensitizer and increased the yield of singlet oxygen generation. OM431 cells were used to evaluate cytotoxicity, cellular uptake and synergistic therapeutic effects of the HA-PFCs-Ppa NPs. HA-PFCs-Ppa NPs showed better cellular uptake compared with free Ppa and HA-Ppa, as demonstrated by flow cytometry analysis and confocal laser scanning microscopy (CLSM). The *in vitro* PDT experiment

showed that this NP effectively inhibited tumor cell growth and killed tumor cells. Significant decrease of tumor volume (to 6.9%) was observed in *in vivo* experiment. It indicated that the HA-PFCs-Ppa possessed great PDT efficiency in ocular tumor.

In 2019, Huang and coworkers developed self-assembled HA-NPs functionalized with BFVPBT *via* disulfide linkages, a novel conjugated oligomer photosensitizer ¹²⁰. The BFVPBT moieties in HA-SS-BFVPBT NPs not only provided a hydrophobic domain for the formation of NPs and drug entrapment, but also acted as excellent two-photon imaging and PDT agents. CPT-loaded HSBNPs could be efficiently degraded by the reductive GSH and overexpressed hyaluronidase in cancer cells. As a result, the NPs released drugs rapidly and boosted strong two-photon fluorescent signals to indicate the presence of tumor. *In vitro* two-photon and *in vivo* one-photon fluorescence imaging with HeLa cells and HeLa-tumor-bearing mice demonstrated the target-specific drug delivery capability of CPT-loaded HSBNPs. Moreover, *in vitro* cytotoxicity experiments demonstrated synergistic effects of PDT therapy *via* BFVPBT and chemotherapy due to CPT.

In 2017, Dong and coworkers developed self-assembled HA-NPs functionalized with a furan flanked diketopyrrolopyrrole (FDPP) molecule ¹²¹. This molecule has a good singlet oxygen quantum yield (26%). FDPP was covalently connected with HA, yielding HA-FDPP NPs conjugate for PDT. Both *in vitro* and *in vivo* experiments demonstrated that HA-FDPP NPs had strong specific targeting ability to HCT-116 tumor cells.

1.4.5 Photothermal therapy

In PTT, photosensitizers serve as the therapeutic agents. When present in the target tumor site, upon light irradiation, heat generated from photosensitizers can induce cellular necrosis and apoptosis with excellent spatial and temporal controls. Self-assembled HA-NPs have been shown

to be useful to deliver photosensitizers for effective anti-tumor therapy. Various photosensitizers can be employed as shown in **Table 1.6**.

PPT agents	references
IR780	42-44
IR808	45
polyaniline	29
CuS	52
cyclodextrin	123
Diketopyrrolopyrrole (DPP) derivatives	124

Table 1.6 Self-assembled HA-NPs for photothermal therapy.

IR780. In 2017, Guo and coworkers developed HA-NPs functionalized with IR780 for PTT⁴³. IR780 was conjugated to HA using 4-aminothiophenol as a linker. In the same year, Kim and coworkers developed self-assembled HA-NPs functionalized with IR780 and polypyrrole for PTT and PDT^{44, 47}. IR-780 was loaded into the PLGA core, decorated with polypyrrole shells and HA. Under NIR irradiation, these self-assembled HA-NPs generated reactive oxygen species and heat, demonstrating synergistic therapeutic effects. SCC-7 and MDA-MB-231 cells with high levels of CD44 receptor were used to evaluate cellular uptake and *in vitro* cytotoxicity. SCC-7 xenograft mice were used to evaluate the efficacy of combined PTT and PDT. The effective uptake and heat and ROS generation in response to NIR irradiation significantly inhibited cell viability. An *in vivo* study showed nearly complete tumor ablation, demonstrating the effective combination therapy. In 2019, Costa and co-workers developed self-assembled HA-NPs functionalized with poly(maleic anhydride-alt-1-octadecene), IR780 and DOX⁴². Poly(maleic anhydride-alt-1-octadecene) was conjugated to the HA backbone and then IR780 and DOX were encapsulated into HA-NPs through

the nanoprecipitation method. This HA-NPs showed good cellular uptake by CD44 expressing MCF-7 cells.

IR808. In 2017, Cai and co-workers developed IR808 functionalized self-assembled HA-NPs for PTT, as well as NIR and PA imaging ⁴⁵. Upon laser irradiation, IR808 showed excellent NIR and PA imaging capability in tumor-bearing mice. In addition, the tight nanostructure arising from the covalent link between HA and IR808 could significantly improve the light-thermal conversion efficiency of IR808. Under a low dose of laser power, these self-assembled HA-NPs achieved more effective photothermal therapy for the suppression of tumor growth both *in vitro* and *in vivo* as compared to free IR808 dye.

Polyaniline. In 2015, Liang and coworkers developed self-assembled HA-NPs functionalized with polyaniline (PANI) for photothermal therapy ²⁹. Upon absorption of light, polyaniline can generate a substantial amount of heat, and thus can be a promising photothermal agent. Meanwhile, PANI is highly positively charged, which can interact with the highly negatively charged HA to self-assemble into NPs. *In vitro* experiment demonstrated that HA–PANI NPs could selectively kill HeLa and HCT-116 cells but not normal HFF cells upon exposure to a NIR 808 nm laser. Moreover, enhanced intracellular uptake of HA–PANI NPs was observed in both HeLa and HCT-116 cells, which could be explained by the CD44 mediated cellular uptake. *In vivo* experiment with tumor bearing mice demonstrated that HA–PANI NPs effectively induced photothermal ablation of tumors.

Cyclodextrin. In 2017, Park and coworkers reported self-assembled HA-NPs functionalized with β -cyclodextrin (β -CD) for photothermal therapy and chemotherapy ¹²³. TPP and boronic acid (BA), β -CD were covalently conjugated to HA. PTX was then allowed to complex with this HA conjugate for self-assembly, yielding a shell-like composite on a core of

carbonized fluorescent polydopamine nanoparticles (FNPs-pDA) applicable for photothermal therapy as well as bioimaging. The successful diol cross-linking between core@shells generated nanocarriers [FNPs-pDA@HA-TPP-CD-PTX] that could be used as an extracellular HA- and intracellular TPP-mediated dual targeting system. The carbonized FNPs-pDA was cross-linked with the boronic acid groups of HA-TPP-CD-PTX to promote the formation of boronate esters for pH-mediated photothermal activity, which showed time dependent complete PTX release along with a photothermal mediated response.

Diketopyrrolopyrrole derivatives. In 2016, Dong and coworkers developed self-assembled HA-NPs functionalized with a novel Diketopyrrolopyrrole (DPP) derivative, 2,5-bis-(6-bromohexyl)-3,6-di-thiophen-2-yl-2,5-dihydro-pyrrolo[3,4-c]pyrrole-1,4-dione (DTDPP), for photothermal therapy ¹²⁴. The inclusion of a thiophene group in DTDPP provided excellent fluorescence, and considerable ability to generate singlet oxygen due to the heavy atom effect. Furthermore, the long di-alkyl chain on *N*-atom of DPP greatly improved the solubility of DTDPP in organic solutions, which is beneficial for further modification. Most important of all, the conjunction of HA to DTDPP overcame its poor aqueous solubility and non-selectivity toward tumor cells. The DTDPP-HA led to high levels of singlet oxygen generation and selective targeting to CD44 receptor expressing cancer cells, as well as low dark toxicity and high phototoxicity. More importantly, both *in vitro* and *in vivo* experiments revealed that DTDPP-HA effectively suppressed tumor growth.

1.5 Conclusions and future outlook

HA has been extensively utilized in nanotechnology. In this review, we summarized the development of a class of HA based nanomaterials, i.e., NPs formed through self-assembly of HA derivatives. With multiple functional groups including carboxylic acid and hydroxyl groups in the

main chain and the hemiacetal at the reducing end, HA can be readily derivatized with hydrophobic domains, transforming it into an amphiphilic molecule capable of self-assembly into NPs. As a targeting ligand, HA can enable selective accumulation of the NPs in disease sites overexpressing HA receptors such as CD44. With their hydrophobic cores, the self-assembled particles can encapsulate a wide range of structurally diverse molecules ranging from small hydrophobic compounds, fluorophores, to nucleic acids and proteins. HA can help enhance the aqueous solubility of hydrophobic drugs, protect the nucleic acids from nuclease degradation, change the biodistribution and reduce the toxicities of therapeutic compounds. Furthermore, with their large carrying capacity, the self-assembled HA-NPs are capable of accommodating multiple cargos within one carrier system, enabling multi-functional applications.

While the advantages of self-assembled HA nanomaterials have been demonstrated, several attributes of building such constructs need to be addressed. The diverse chemistry applied to form HA-NPs implies that the core, composition, and the structure of the materials need to be tailored to fit each specific biological application. Another important consideration is that the expression of HA receptors such as CD44 is not restricted to tumor cells or inflammatory cells. However, it is known that there are structural differences between various CD44 as inflammatory signals to cells can enhance the affinity of expressed CD44 with HA ¹²⁵. Further study and understanding of HA receptor structures and regulation factors can help improve the precision in targeting HA-NPs to diseased sites and reduce the amount accumulating in normal tissues.

Besides CD44, there are multiple types of HA receptors, in particular HA receptor for endocytosis (HARE) expressed in liver. It is important to minimize liver uptake of HA nanomaterials to avoid liver toxicity if liver is not the targeted site. More specific HA derivatives can be developed with much enhanced CD44 affinities. To facilitate this effort, the co-crystal

structures of CD44 and a HA octasaccharide can provide the critical insights ¹⁷. In addition, combinatorial synthesis of functionalized HA can be pursued for ligand screening to complement structure-based design. With further development, many more innovative applications of self-assembled HA-NPs can be achieved to address challenging biomedical problems.

REFERENCES

REFERENCES

1. Day, A. J.; Prestwich, G. D., Hyaluronan-binding proteins: tying up the giant. *J. Biol. Chem.* **2002**, *277*, 4585-4588.
2. Schanté, C. E.; Zuber, G.; Herlin, C.; Vandamme, T. F., Chemical modifications of hyaluronic acid for the synthesis of derivatives for a broad range of biomedical applications. *Carbohydr. Polym.* **2011**, *85*, 469-489.
3. Iwai, K.; Maeda, H.; Konno, T., Use of oily contrast medium for selective drug targeting to tumor: enhanced therapeutic effect and X-ray image. *Cancer Res.* **1984**, *44*, 2115-2121.
4. Matsumura, Y.; Maeda, H., A new concept for macromolecular therapeutics in cancer chemotherapy: mechanism of tumorotropic accumulation of proteins and the antitumor agent smancs. *Cancer Res.* **1986**, *46*, 6387-6392.
5. Kumar, A.; Sahoo, B.; Montpetit, A.; Behera, S.; Lockey, R. F.; Mohapatra, S. S., Development of hyaluronic acid-Fe₂O₃ hybrid magnetic nanoparticles for targeted delivery of peptides. *Nanomed. Nanotechnol. Biol. Med.* **2007**, *3*, 132-137.
6. Dosio, F.; Arpicco, S.; Stella, B.; Fattal, E., Hyaluronic acid for anticancer drug and nucleic acid delivery. *Adv. Drug Del. Rev.* **2016**, *97*, 204-236.
7. Lin, W. J.; Lee, W.-C.; Shieh, M.-J., Hyaluronic acid conjugated micelles possessing CD44 targeting potential for gene delivery. *Carbohydr. Polym.* **2017**, *155*, 101-108.
8. Hu, Y.; Yang, J.; Wei, P.; Li, J.; Ding, L.; Zhang, G.; Shi, X.; Shen, M., Facile synthesis of hyaluronic acid-modified Fe₃O₄/Au composite nanoparticles for targeted dual mode MR/CT imaging of tumors. *J. Mater. Chem. B* **2015**, *3*, 9098-9108.
9. Tripodo, G.; Trapani, A.; Torre, M. L.; Giammona, G.; Trapani, G.; Mandracchia, D., Hyaluronic acid and its derivatives in drug delivery and imaging: recent advances and challenges. *Eur. J. Pharm. Biopharm.* **2015**, *97*, 400-416.
10. Wickens, J. M.; Alsaab, H. O.; Kesharwani, P.; Bhise, K.; Amin, M. C. I. M.; Tekade, R. K.; Gupta, U.; Iyer, A. K., Recent advances in hyaluronic acid-decorated nanocarriers for targeted cancer therapy. *Drug Discov. Today* **2017**, *22*, 665-680.
11. Bayer, I. S., Hyaluronic acid and controlled release: A review. *Molecules* **2020**, *25*, 2649.
12. Rao, N. V.; Yoon, H. Y.; Han, H. S.; Ko, H.; Son, S.; Lee, M.; Lee, H.; Jo, D.-G.; Kang, Y. M.; Park, J. H., Recent developments in hyaluronic acid-based nanomedicine for targeted cancer treatment. *Expert Opin. Drug Deliv.* **2016**, *13*, 239-252.
13. Luo, Z.; Dai, Y.; Gao, H., Development and application of hyaluronic acid in tumor targeting drug delivery. *Acta Pharm. Sin. B* **2019**, *9*, 1099-1112.

14. Cho, H.-J.; Yoon, I.-S.; Yoon, H. Y.; Koo, H.; Jin, Y.-J.; Ko, S.-H.; Shim, J.-S.; Kim, K.; Kwon, I. C.; Kim, D.-D., Polyethylene glycol-conjugated hyaluronic acid-ceramide self-assembled nanoparticles for targeted delivery of doxorubicin. *Biomaterials* **2012**, *33*, 1190-1200.
15. Nasr, S. H.; Rashidijahanabad, Z.; Ramadan, S.; Kauffman, N.; Parameswaran, N.; Zinn, K. R.; Qian, C.; Arora, R.; Agnew, D.; Huang, X., Effective atherosclerotic plaque inflammation inhibition with targeted drug delivery by hyaluronan conjugated atorvastatin nanoparticles. *Nanoscale* **2020**, *12*, 9541-9556.
16. Li, W.; Zheng, C.; Pan, Z.; Chen, C.; Hu, D.; Gao, G.; Kang, S.; Cui, H.; Gong, P.; Cai, L., Smart hyaluronidase-activated theranostic micelles for dual-modal imaging guided photodynamic therapy. *Biomaterials* **2016**, *101*, 10-19.
17. Banerji, S.; Wright, A. J.; Noble, M.; Mahoney, D. J.; Campbell, I. D.; Day, A. J.; Jackson, D. G., Structures of the Cd44-hyaluronan complex provide insight into a fundamental carbohydrate-protein interaction. *Nat. Struct. Mol. Biol.* **2007**, *14*, 234-239.
18. Upadhyay, K. K.; Meins, J.-F. L.; Misra, A.; Voisin, P.; Bouchaud, V.; Ibarboure, E.; Schatz, C.; Lecommandoux, S., Biomimetic doxorubicin loaded polymersomes from hyaluronan-block-poly (γ -benzyl glutamate) copolymers. *Biomacromolecules* **2009**, *10*, 2802-2808.
19. Zhong, Y.; Goltsche, K.; Cheng, L.; Xie, F.; Meng, F.; Deng, C.; Zhong, Z.; Haag, R., Hyaluronic acid-shelled acid-activatable paclitaxel prodrug micelles effectively target and treat CD44-overexpressing human breast tumor xenografts in vivo. *Biomaterials* **2016**, *84*, 250-261.
20. Cho, H.-J.; Yoon, H. Y.; Koo, H.; Ko, S.-H.; Shim, J.-S.; Lee, J.-H.; Kim, K.; Kwon, I. C.; Kim, D.-D., Self-assembled nanoparticles based on hyaluronic acid-ceramide (HA-CE) and Pluronic® for tumor-targeted delivery of docetaxel. *Biomaterials* **2011**, *32*, 7181-7190.
21. Lee, H.; Lee, K.; Park, T. G., Hyaluronic acid-paclitaxel conjugate micelles: Synthesis, characterization, and antitumor activity. *Bioconjug. Chem.* **2008**, *19*, 1319-1325.
22. Wang, L.; Wang, Y.; Jin, Q.; Jia, F.; Wang, H.; Ji, J., Biomimic pH/reduction dual-sensitive reversibly cross-linked hyaluronic acid prodrug micelles for targeted intracellular drug delivery. *Polymer* **2015**, *76*, 237-244.
23. Li, J.; Huo, M.; Wang, J.; Zhou, J.; Mohammad, J. M.; Zhang, Y.; Zhu, Q.; Waddad, A. Y.; Zhang, Q., Redox-sensitive micelles self-assembled from amphiphilic hyaluronic acid-deoxycholic acid conjugates for targeted intracellular delivery of paclitaxel. *Biomaterials* **2012**, *33*, 2310-2320.
24. Park, H.-K.; Lee, S. J.; Oh, J.-S.; Lee, S.-G.; Jeong, Y.-I.; Lee, H. C., Smart nanoparticles based on hyaluronic acid for redox-responsive and CD44 receptor-mediated targeting of tumor. *Nanoscale Res. Lett.* **2015**, *10*, 288.
25. Meyer, E. E.; Rosenberg, K. J.; Israelachvili, J., Recent progress in understanding hydrophobic interactions. *Proc. Natl. Acad. Sci. U. S. A.* **2006**, *103*, 15739-15746.

26. Tammaro, O.; di Polidoro, A. C.; Romano, E.; Netti, P. A.; Torino, E., A Microfluidic Platform to design Multimodal PEG-crosslinked Hyaluronic Acid Nanoparticles (PEG-cHANPs) for diagnostic applications. *Sci. Rep.* **2020**, *10*, 1-11.
27. Russo, M.; Bevilacqua, P.; Netti, P. A.; Torino, E., A Microfluidic Platform to design crosslinked Hyaluronic Acid Nanoparticles (cHANPs) for enhanced MRI. *Sci. Rep.* **2016**, *6*, 1-10.
28. Zaki, N. M.; Nasti, A.; Tirelli, N., Nanocarriers for cytoplasmic delivery: cellular uptake and intracellular fate of chitosan and hyaluronic acid-coated chitosan nanoparticles in a phagocytic cell model. *Macromol. Biosci.* **2011**, *11*, 1747-1760.
29. Jiang, B.-P.; Zhang, L.; Zhu, Y.; Shen, X.-C.; Ji, S.-C.; Tan, X.-Y.; Cheng, L.; Liang, H., Water-soluble hyaluronic acid-hybridized polyaniline nanoparticles for effectively targeted photothermal therapy. *J. Mater. Chem. B* **2015**, *3*, 3767-3776.
30. Liu, H.-n.; Guo, N.-n.; Guo, W.-w.; Huang-Fu, M.-y.; Vakili, M. R.; Chen, J.-j.; Xu, W.-h.; Wei, Q.-c.; Han, M.; Lavasanifar, A., Delivery of mitochondriotropic doxorubicin derivatives using self-assembling hyaluronic acid nanocarriers in doxorubicin-resistant breast cancer. *Acta Pharm. Sin. B* **2018**, *39*, 1681-1692.
31. Payne, W. M.; Hill, T. K.; Svehkarev, D.; Holmes, M. B.; Sajja, B. R.; Mohs, A. M., Multimodal imaging nanoparticles derived from hyaluronic acid for integrated preoperative and intraoperative cancer imaging. *Contrast Media Mol. Imaging* **2017**, *2017*.
32. Moon, M.; Thomas, R. G.; Heo, S.-u.; Park, M.-S.; Bae, W. K.; Heo, S. H.; Yim, N. Y.; Jeong, Y. Y., A Hyaluronic Acid-Conjugated Gadolinium Hepatocyte-Specific T1 Contrast Agent for Liver Magnetic Resonance Imaging. *Mol. Imaging Biol.* **2015**, *17*, 497-503.
33. Dubey, R. D.; Klippstein, R.; Wang, J. T.-W.; Hodgins, N.; Mei, K.-C.; Sosabowski, J.; Hider, R. C.; Abbate, V.; Gupta, P. N.; Al-Jamal, K. T., Novel hyaluronic acid conjugates for dual nuclear imaging and therapy in CD44-expressing tumors in mice in vivo. *Nanotheranostics* **2017**, *1*, 59.
34. Choi, K. Y.; Chung, H.; Min, K. H.; Yoon, H. Y.; Kim, K.; Park, J. H.; Kwon, I. C.; Jeong, S. Y., Self-assembled hyaluronic acid nanoparticles for active tumor targeting. *Biomaterials* **2010**, *31*, 106-114.
35. Choi, K. Y.; Min, K. H.; Yoon, H. Y.; Kim, K.; Park, J. H.; Kwon, I. C.; Choi, K.; Jeong, S. Y., PEGylation of hyaluronic acid nanoparticles improves tumor targetability in vivo. *Biomaterials* **2011**, *32*, 1880-1889.
36. Lin, C.; Kim, S. B.; Yon, J.-M.; Park, S. G.; Gwon, L. W.; Lee, J.-G.; Baek, I.-J.; Lee, B. J.; Yun, Y. W.; Nam, S.-Y., Temporal and subcellular distributions of Cy5. 5-labeled hyaluronic acid nanoparticles in mouse organs during 28 days as a drug carrier. *Korean J. Vet. Res.* **2017**, *57*, 215-222.
37. Lee, J.-Y.; Chung, S.-J.; Cho, H.-J.; Kim, D.-D., Iodinated hyaluronic acid oligomer-based nanoassemblies for tumor-targeted drug delivery and cancer imaging. *Biomaterials* **2016**,

85, 218-231.

38. Gao, S.; Wang, J.; Tian, R.; Wang, G.; Zhang, L.; Li, Y.; Li, L.; Ma, Q.; Zhu, L., Construction and evaluation of a targeted hyaluronic acid nanoparticle/photosensitizer complex for cancer photodynamic therapy. *ACS Appl. Mater. Interfaces* **2017**, *9*, 32509-32519.
39. Yoon, H. Y.; Koo, H.; Choi, K. Y.; Lee, S. J.; Kim, K.; Kwon, I. C.; Leary, J. F.; Park, K.; Yuk, S. H.; Park, J. H., Tumor-targeting hyaluronic acid nanoparticles for photodynamic imaging and therapy. *Biomaterials* **2012**, *33*, 3980-3989.
40. Qi, B.; Crawford, A. J.; Wojtynek, N. E.; Holmes, M. B.; Soucek, J. J.; Almeida-Porada, G.; Ly, Q. P.; Cohen, S. M.; Hollingsworth, M. A.; Mohs, A. M., Indocyanine green loaded hyaluronan-derived nanoparticles for fluorescence-enhanced surgical imaging of pancreatic cancer. *Nanomed. Nanotechnol. Biol. Med.* **2018**, *14*, 769-780.
41. Hill, T. K.; Kelkar, S. S.; Wojtynek, N. E.; Soucek, J. J.; Payne, W. M.; Stumpf, K.; Marini, F. C.; Mohs, A. M., Near infrared fluorescent nanoparticles derived from hyaluronic acid improve tumor contrast for image-guided surgery. *Theranostics* **2016**, *6*, 2314.
42. Alves, C. G.; de Melo-Diogo, D.; Lima-Sousa, R.; Costa, E. C.; Correia, I. J., Hyaluronic acid functionalized nanoparticles loaded with IR780 and DOX for cancer chemo-photothermal therapy. *Eur. J. Pharm. Biopharm.* **2019**, *137*, 86-94.
43. Lin, T.; Yuan, A.; Zhao, X.; Lian, H.; Zhuang, J.; Chen, W.; Zhang, Q.; Liu, G.; Zhang, S.; Cao, W., Self-assembled tumor-targeting hyaluronic acid nanoparticles for photothermal ablation in orthotopic bladder cancer. *Acta Biomater.* **2017**, *53*, 427-438.
44. Daeihamed, M.; Haeri, A.; Ostad, S. N.; Akhlaghi, M. F.; Dadashzadeh, S., Doxorubicin-loaded liposomes: enhancing the oral bioavailability by modulation of physicochemical characteristics. *Nanomedicine* **2017**, *12*, 1187-1202.
45. Li, S.; Sun, Z.; Deng, G.; Meng, X.; Li, W.; Ni, D.; Zhang, J.; Gong, P.; Cai, L., Dual-modal imaging-guided highly efficient photothermal therapy using heptamethine cyanine-conjugated hyaluronic acid micelles. *Biomater. Sci.* **2017**, *5*, 1122-1129.
46. Wu, J.; Hu, X.; Liu, R.; Zhang, J.; Song, A.; Luan, Y., pH-responsive and self-targeting assembly from hyaluronic acid-based conjugate toward all-in-one chemo-photodynamic therapy. *J. Colloid Interface Sci.* **2019**, *547*, 30-39.
47. Tran, T. H.; Nguyen, H. T.; Phuong Tran, T. T.; Ku, S. K.; Jeong, J.-H.; Choi, H.-G.; Yong, C. S.; Kim, J. O., Combined photothermal and photodynamic therapy by hyaluronic acid-decorated polypyrrole nanoparticles. *Nanomedicine* **2017**, *12*, 1511-1523.
48. Gouin, S.; Grayeb, M. V. V.; Winnik, F. M. In *Gadolinium diethylenetriaminepentaacetic acid hyaluronan conjugates: preparation, properties and applications*, Macromolecular Symposia, Wiley Online Library: 2002; pp 105-110.
49. Wu, G.; Zhang, H.; Zhan, Z.; Lu, Q.; Cheng, J.; Xu, J.; Zhu, J., Hyaluronic Acid-

Gadolinium Complex Nanospheres as Lymphatic System-Specific Contrast Agent for Magnetic Resonance Imaging. *Chin. J. Chem.* **2015**, *33*, 1153-1158.

50. Cho, H.-J.; Yoon, H. Y.; Koo, H.; Ko, S.-H.; Shim, J.-S.; Cho, J.-H.; Park, J. H.; Kim, K.; Kwon, I. C.; Kim, D.-D., Hyaluronic acid-ceramide-based optical/MR dual imaging nanoprobe for cancer diagnosis. *J. Control. Release* **2012**, *162*, 111-118.

51. Zhang, L.; Liu, T.; Xiao, Y.; Yu, D.; Zhang, N., Hyaluronic acid-chitosan nanoparticles to deliver Gd-DTPA for MR cancer imaging. *Nanomaterials* **2015**, *5*, 1379-1396.

52. Zhang, L.; Gao, S.; Zhang, F.; Yang, K.; Ma, Q.; Zhu, L., Activatable hyaluronic acid nanoparticle as a theranostic agent for optical/photoacoustic image-guided photothermal therapy. *ACS Nano* **2014**, *8*, 12250-12258.

53. Miki, K.; Inoue, T.; Kobayashi, Y.; Nakano, K.; Matsuoka, H.; Yamauchi, F.; Yano, T.; Ohe, K., Near-infrared dye-conjugated amphiphilic hyaluronic acid derivatives as a dual contrast agent for in vivo optical and photoacoustic tumor imaging. *Biomacromolecules* **2015**, *16*, 219-227.

54. Kim, H.; Mun, S.; Choi, Y., Photosensitizer-conjugated polymeric nanoparticles for redox-responsive fluorescence imaging and photodynamic therapy. *J. Mater. Chem. B* **2013**, *1*, 429-431.

55. Park, K. E.; Noh, Y.-W.; Kim, A.; Lim, Y. T., Hyaluronic acid-coated nanoparticles for targeted photodynamic therapy of cancer guided by near-infrared and MR imaging. *Carbohydr. Polym.* **2017**, *157*, 476-483.

56. Quinones, J. P.; Jokinen, J.; Keinänen, S.; Covas, C. P.; Brüggemann, O.; Ossipov, D., Self-assembled hyaluronic acid-testosterone nanocarriers for delivery of anticancer drugs. *Eur. Polym. J.* **2018**, *99*, 384-393.

57. Liu, H.-N.; Guo, N.-N.; Wang, T.-T.; Guo, W.-W.; Lin, M.-T.; Huang-Fu, M.-Y.; Vakili, M. R.; Xu, W.-H.; Chen, J.-J.; Wei, Q.-C., Mitochondrial targeted doxorubicin-triphenylphosphonium delivered by hyaluronic acid modified and pH responsive nanocarriers to breast tumor: in vitro and in vivo studies. *Mol. Pharm.* **2018**, *15*, 882-891.

58. Feigl, V.; Anton, A.; Uzigner, N.; Gruiz, K., Red mud as a chemical stabilizer for soil contaminated with toxic metals. *Water, Air, Soil Pollut.* **2012**, *223*, 1237-1247.

59. Lee, H.; Ahn, C. H.; Park, T. G., Poly [lactic-co-(glycolic acid)]-grafted hyaluronic acid copolymer micelle nanoparticles for target-specific delivery of doxorubicin. *Macromol. Biosci.* **2009**, *9*, 336-342.

60. Son, G. M.; Kim, H. Y.; Ryu, J. H.; Chu, C. W.; Kang, D. H.; Park, S. B.; Jeong, Y.-I., Self-assembled polymeric micelles based on hyaluronic acid-g-poly (D, L-lactide-co-glycolide) copolymer for tumor targeting. *Int. J. Mol. Sci.* **2014**, *15*, 16057-16068.

61. Upadhyay, K. K.; Bhatt, A. N.; Mishra, A. K.; Dwarakanath, B. S.; Jain, S.; Schatz, C.; Le Meins, J.-F.; Farooque, A.; Chandraiah, G.; Jain, A. K., The intracellular drug delivery and

anti tumor activity of doxorubicin loaded poly (γ -benzyl L-glutamate)-b-hyaluronan polymersomes. *Biomaterials* **2010**, *31*, 2882-2892.

62. Deng, C.; Xu, X.; Tashi, D.; Wu, Y.; Su, B.; Zhang, Q., Co-administration of biocompatible self-assembled polylactic acid–hyaluronic acid block copolymer nanoparticles with tumor-penetrating peptide-iRGD for metastatic breast cancer therapy. *J. Mater. Chem. B* **2018**, *6*, 3163-3180.

63. Jo, Y.-u.; Lee, C. B.; Bae, S. K.; Na, K., Acetylated hyaluronic acid-poly (L-lactic acid) conjugate nanoparticles for inhibition of doxorubicinol production from doxorubicin. *Macromol. Res.* **2020**, *28*, 67-73.

64. Pitarresi, G.; Palumbo, F. S.; Albanese, A.; Fiorica, C.; Picone, P.; Giammona, G., Self-assembled amphiphilic hyaluronic acid graft copolymers for targeted release of antitumoral drug. *J. Drug Target.* **2010**, *18*, 264-276.

65. Wu, J.-l.; Liu, C.-g.; Wang, X.-l.; Huang, Z.-h., Preparation and characterization of nanoparticles based on histidine–hyaluronic acid conjugates as doxorubicin carriers. *J. Mater. Sci. Mater. Med.* **2012**, *23*, 1921-1929.

66. Hsu, M. F.; Tyan, Y. S.; Chien, Y. C.; Lee, M. W., Hyaluronic acid-based nano-sized drug carrier-containing Gellan gum microspheres as potential multifunctional embolic agent. *Sci. Rep.* **2018**, *8*, 1-10.

67. Yan, X.; Chen, Q.; An, J.; Liu, D.-E.; Huang, Y.; Yang, R.; Li, W.; Chen, L.; Gao, H., Hyaluronic acid/PEGylated amphiphilic nanoparticles for pursuit of selective intracellular doxorubicin release. *J. Mater. Chem. B* **2019**, *7*, 95-102.

68. Choi, K. Y.; Yoon, H. Y.; Kim, J.-H.; Bae, S. M.; Park, R.-W.; Kang, Y. M.; Kim, I.-S.; Kwon, I. C.; Choi, K.; Jeong, S. Y., Smart nanocarrier based on PEGylated hyaluronic acid for cancer therapy. *ACS Nano* **2011**, *5*, 8591-8599.

69. Huang, P.; Yang, C.; Liu, J.; Wang, W.; Guo, S.; Li, J.; Sun, Y.; Dong, H.; Deng, L.; Zhang, J., Improving the oral delivery efficiency of anticancer drugs by chitosan coated polycaprolactone-grafted hyaluronic acid nanoparticles. *J. Mater. Chem. B* **2014**, *2*, 4021-4033.

70. Wang, X.; Gu, X.; Wang, H.; Yang, J.; Mao, S., Enhanced delivery of doxorubicin to the liver through self-assembled nanoparticles formed via conjugation of glycyrrhetic acid to the hydroxyl group of hyaluronic acid. *Carbohydr. Polym.* **2018**, *195*, 170-179.

71. Wei, W.-H.; Dong, X.-M.; Liu, C.-G., In vitro investigation of self-assembled nanoparticles based on hyaluronic acid-deoxycholic acid conjugates for controlled release doxorubicin: effect of degree of substitution of deoxycholic acid. *Int. J. Mol. Sci.* **2015**, *16*, 7195-7209.

72. Wang, J.; Ma, W.; Guo, Q.; Li, Y.; Hu, Z.; Zhu, Z.; Wang, X.; Zhao, Y.; Chai, X.; Tu, P., The effect of dual-functional hyaluronic acid-vitamin E succinate micelles on targeting delivery of doxorubicin. *Int. J. Nanomedicine* **2016**, *11*, 5851.

73. Yang, Y.; Zhao, Y.; Lan, J.; Kang, Y.; Zhang, T.; Ding, Y.; Zhang, X.; Lu, L., Reduction-sensitive CD44 receptor-targeted hyaluronic acid derivative micelles for doxorubicin delivery. *Int. J. Nanomedicine* **2018**, *13*, 4361.
74. Li, S.; Zhao, W.; Liang, N.; Xu, Y.; Kawashima, Y.; Sun, S., Multifunctional micelles self-assembled from hyaluronic acid conjugate for enhancing anti-tumor effect of paclitaxel. *React. Funct. Polym.* **2020**, *152*, 104608.
75. Song, Y.; Cai, H.; Yin, T.; Huo, M.; Ma, P.; Zhou, J.; Lai, W., Paclitaxel-loaded redox-sensitive nanoparticles based on hyaluronic acid-vitamin E succinate conjugates for improved lung cancer treatment. *Int. J. Nanomedicine* **2018**, *13*, 1585.
76. Li, J.; Huang, P.; Chang, L.; Long, X.; Dong, A.; Liu, J.; Chu, L.; Hu, F.; Liu, J.; Deng, L., Tumor targeting and pH-responsive polyelectrolyte complex nanoparticles based on hyaluronic acid-paclitaxel conjugates and chitosan for oral delivery of paclitaxel. *Macromol. Res.* **2013**, *21*, 1331-1337.
77. Ravari, N. S.; Goodarzi, N.; Alvandifar, F.; Amini, M.; Souri, E.; Khoshayand, M. R.; Mirzaie, Z. H.; Atyabi, F.; Dinarvand, R., Fabrication and biological evaluation of chitosan coated hyaluronic acid-docetaxel conjugate nanoparticles in CD44⁺ cancer cells. *DARU J. Pharm. Sci.* **2016**, *24*, 21.
78. Luo, Y.; Ziebell, M. R.; Prestwich, G. D., A hyaluronic acid– taxol antitumor bioconjugate targeted to cancer cells. *Biomacromolecules* **2000**, *1*, 208-218.
79. Wu, J.; Zhang, J.; Deng, C.; Meng, F.; Cheng, R.; Zhong, Z., Robust, responsive, and targeted PLGA anticancer nanomedicines by combination of reductively cleavable surfactant and covalent hyaluronic acid coating. *ACS Appl. Mater. Interfaces* **2017**, *9*, 3985-3994.
80. Zhang, J.; Song, J.; Liang, X.; Yin, Y.; Zuo, T.; Chen, D.; Shen, Q., Hyaluronic acid-modified cationic nanoparticles overcome enzyme CYP1B1-mediated breast cancer multidrug resistance. *Nanomedicine* **2019**, *14*, 447-464.
81. Yadav, A. K.; Agarwal, A.; Rai, G.; Mishra, P.; Jain, S.; Mishra, A. K.; Agrawal, H.; Agrawal, G. P., Development and characterization of hyaluronic acid decorated PLGA nanoparticles for delivery of 5-fluorouracil. *Drug Deliv.* **2010**, *17*, 561-572.
82. Wang, T.; Hou, J.; Su, C.; Zhao, L.; Shi, Y., Hyaluronic acid-coated chitosan nanoparticles induce ROS-mediated tumor cell apoptosis and enhance antitumor efficiency by targeted drug delivery via CD44. *J. Nanobiotechnology* **2017**, *15*, 7.
83. Zhang, W.; Cai, J.; Wu, B.; Shen, Z., pH-responsive hyaluronic acid nanoparticles coloaded with sorafenib and cisplatin for treatment of hepatocellular carcinoma. *J. Biomater. Appl.* **2019**, *34*, 219-228.
84. Jeong, Y. I.; Kim, S. T.; Jin, S. G.; Ryu, H. H.; Jin, Y. H.; Jung, T. Y.; Kim, I. Y.; Jung, S., Cisplatin-incorporated hyaluronic acid nanoparticles based on ion-complex formation. *J. Pharm. Sci.* **2008**, *97*, 1268-1276.

85. Liu, C.; Bae, K. H.; Yamashita, A.; Chung, J. E.; Kurisawa, M., Thiol-mediated synthesis of hyaluronic acid–epigallocatechin-3-O-gallate conjugates for the formation of injectable hydrogels with free radical scavenging property and degradation resistance. *Biomacromolecules* **2017**, *18*, 3143-3155.
86. Parashar, P.; Rathor, M.; Dwivedi, M.; Saraf, S. A., Hyaluronic acid decorated naringenin nanoparticles: Appraisal of chemopreventive and curative potential for lung cancer. *Pharmaceutics* **2018**, *10*, 33.
87. Jiang, S.; Li, M.; Hu, Y.; Zhang, Z.; Lv, H., Multifunctional self-assembled micelles of galactosamine-hyaluronic acid-vitamin E succinate for targeting delivery of norcantharidin to hepatic carcinoma. *Carbohydr. Polym.* **2018**, *197*, 194-203.
88. Zhao, J.; Wang, Y.; Ma, Y.; Liu, Y.; Yan, B.; Wang, L., Smart nanocarrier based on PEGylated hyaluronic acid for deacetyl mycoepoxydience: High stability with enhanced bioavailability and efficiency. *Carbohydr. Polym.* **2019**, *203*, 356-368.
89. Maiti, A.; Maki, G.; Johnson, P., TNF- α induction of CD44-mediated leukocyte adhesion by sulfation. *Science* **1998**, *282*, 941-943.
90. Parajó, Y.; d'Angelo, I.; Welle, A.; Garcia-Fuentes, M.; Alonso, M. J., Hyaluronic acid/Chitosan nanoparticles as delivery vehicles for VEGF and PDGF-BB. *Drug Deliv.* **2010**, *17*, 596-604.
91. Sivasubramanian, M.; Kang, A. R.; Han, H. S.; Heo, R.; Lee, J.-Y.; Kim, K. J.; Jeon, S. M.; Chae, S. Y.; Jo, D.-G.; Kim, J.-H., Molecular chaperone-like hyaluronic acid nanoparticles: Implications as the carrier for protein delivery systems. *Macromol. Res.* **2012**, *20*, 1007-1010.
92. Lim, D. G.; Prim, R. E.; Kang, E.; Jeong, S. H., One-pot synthesis of dopamine-conjugated hyaluronic acid/polydopamine nanocomplexes to control protein drug release. *Int. J. Pharm.* **2018**, *542*, 288-296.
93. Raviña, M.; Cubillo, E.; Olmeda, D.; Novoa-Carballal, R.; Fernandez-Megia, E.; Riguera, R.; Sánchez, A.; Cano, A.; Alonso, M. J., Hyaluronic acid/chitosan-g-poly (ethylene glycol) nanoparticles for gene therapy: an application for pDNA and siRNA delivery. *Pharm. Res.* **2010**, *27*, 2544-2555.
94. Lu, H.-D.; Zhao, H.-Q.; Wang, K.; Lv, L.-L., Novel hyaluronic acid–chitosan nanoparticles as non-viral gene delivery vectors targeting osteoarthritis. *Int. J. Pharm.* **2011**, *420*, 358-365.
95. Gwak, S.-J.; Jung, J. K.; An, S. S.; Kim, H. J.; Oh, J. S.; Pennant, W. A.; Lee, H. Y.; Kong, M. H.; Kim, K. N.; Yoon, D. H., Chitosan/TPP-hyaluronic acid nanoparticles: a new vehicle for gene delivery to the spinal cord. *J. Biomater. Sci. Polym. Ed.* **2012**, *23*, 1437-1450.
96. Lu, H.; Lv, L.; Dai, Y.; Wu, G.; Zhao, H.; Zhang, F., Porous chitosan scaffolds with embedded hyaluronic acid/chitosan/plasmid-DNA nanoparticles encoding TGF- β 1 induce DNA controlled release, transfected chondrocytes, and promoted cell proliferation. *PLoS One* **2013**, *8*.

97. Deng, X.; Cao, M.; Zhang, J.; Hu, K.; Yin, Z.; Zhou, Z.; Xiao, X.; Yang, Y.; Sheng, W.; Wu, Y., Hyaluronic acid-chitosan nanoparticles for co-delivery of MiR-34a and doxorubicin in therapy against triple negative breast cancer. *Biomaterials* **2014**, *35*, 4333-4344.
98. Liu, Y.; Kong, M.; Cheng, X. J.; Wang, Q. Q.; Jiang, L. M.; Chen, X. G., Self-assembled nanoparticles based on amphiphilic chitosan derivative and hyaluronic acid for gene delivery. *Carbohydr. Polym.* **2013**, *94*, 309-316.
99. De la Fuente, M.; Seijo, B.; Alonso, M. J., Novel hyaluronic acid-chitosan nanoparticles for ocular gene therapy. *Invest. Ophthalmol. Vis. Sci.* **2008**, *49*, 2016-2024.
100. Tran, T.-H.; Krishnan, S.; Amiji, M. M., MicroRNA-223 induced repolarization of peritoneal macrophages using CD44 targeting hyaluronic acid nanoparticles for anti-inflammatory effects. *PLoS One* **2016**, *11*.
101. Jiang, G.; Park, K.; Kim, J.; Kim, K. S.; Oh, E. J.; Kang, H.; Han, S. E.; Oh, Y. K.; Park, T. G.; Kwang Hahn, S., Hyaluronic acid-polyethyleneimine conjugate for target specific intracellular delivery of siRNA. *Biopolymers: Original Research on Biomolecules* **2008**, *89*, 635-642.
102. Park, K.; Lee, M.-Y.; Kim, K. S.; Hahn, S. K., Target specific tumor treatment by VEGF siRNA complexed with reducible polyethyleneimine-hyaluronic acid conjugate. *Biomaterials* **2010**, *31*, 5258-5265.
103. Yao, J.; Fan, Y.; Du, R.; Zhou, J.; Lu, Y.; Wang, W.; Ren, J.; Sun, X., Amphoteric hyaluronic acid derivative for targeting gene delivery. *Biomaterials* **2010**, *31*, 9357-9365.
104. Ganesh, S.; Iyer, A. K.; Morrissey, D. V.; Amiji, M. M., Hyaluronic acid based self-assembling nanosystems for CD44 target mediated siRNA delivery to solid tumors. *Biomaterials* **2013**, *34*, 3489-3502.
105. Aldawsari, H. M.; Dhaliwal, H. K.; Aljaeid, B. M.; Alhakamy, N. A.; Banjar, Z. M.; Amiji, M. M., Optimization of the conditions for plasmid DNA delivery and transfection with self-assembled hyaluronic acid-based nanoparticles. *Mol. Pharm.* **2018**, *16*, 128-140.
106. Ito, T.; Yoshihara, C.; Hamada, K.; Koyama, Y., DNA/polyethyleneimine/hyaluronic acid small complex particles and tumor suppression in mice. *Biomaterials* **2010**, *31*, 2912-2918.
107. Liang, K.; Bae, K. H.; Lee, F.; Xu, K.; Chung, J. E.; Gao, S. J.; Kurisawa, M., Self-assembled ternary complexes stabilized with hyaluronic acid-green tea catechin conjugates for targeted gene delivery. *J. Control. Release* **2016**, *226*, 205-216.
108. Yang, X.; Singh, A.; Choy, E.; Hornicek, F. J.; Amiji, M. M.; Duan, Z., MDR1 siRNA loaded hyaluronic acid-based CD44 targeted nanoparticle systems circumvent paclitaxel resistance in ovarian cancer. *Sci. Rep.* **2015**, *5*, 8509.
109. He, Y.; Cheng, G.; Xie, L.; Nie, Y.; He, B.; Gu, Z., Polyethyleneimine/DNA polyplexes with reduction-sensitive hyaluronic acid derivatives shielding for targeted gene delivery.

Biomaterials **2013**, *34*, 1235-1245.

110. Li, Y.; Zhang, J.; Wang, B.; Shen, Y.; Ouahab, A., Co-delivery of siRNA and hypericin into cancer cells by hyaluronic acid modified PLGA-PEI nanoparticles. *Drug. Dev. Ind. Pharm.* **2016**, *42*, 737-746.

111. Shen, Y.; Li, Q.; Tu, J.; Zhu, J., Synthesis and characterization of low molecular weight hyaluronic acid-based cationic micelles for efficient siRNA delivery. *Carbohydr. Polym.* **2009**, *77*, 95-104.

112. Shen, Y.; Wang, B.; Lu, Y.; Ouahab, A.; Li, Q.; Tu, J., A novel tumor-targeted delivery system with hydrophobized hyaluronic acid–spermine conjugates (HHSCs) for efficient receptor-mediated siRNA delivery. *Int. J. Pharm.* **2011**, *414*, 233-243.

113. Kim, E.; Yang, J.; Kim, H.-O.; An, Y.; Lim, E.-K.; Lee, G.; Kwon, T.; Cheong, J.-H.; Suh, J.-S.; Huh, Y.-M., Hyaluronic acid receptor-targetable imidazolized nanovectors for induction of gastric cancer cell death by RNA interference. *Biomaterials* **2013**, *34*, 4327-4338.

114. Yin, H.; Zhao, F.; Zhang, D.; Li, J., Hyaluronic acid conjugated β -cyclodextrin-oligoethylenimine star polymer for CD44-targeted gene delivery. *Int. J. Pharm.* **2015**, *483*, 169-179.

115. Mok, H.; Park, J. W.; Park, T. G., Antisense oligodeoxynucleotide-conjugated hyaluronic acid/protamine nanocomplexes for intracellular gene inhibition. *Bioconjug. Chem.* **2007**, *18*, 1483-1489.

116. Needham, C. J.; Williams, A. K.; Chew, S. A.; Kasper, F. K.; Mikos, A. G., Engineering a polymeric gene delivery vector based on poly (ethylenimine) and hyaluronic acid. *Biomacromolecules* **2012**, *13*, 1429-1437.

117. Ito, T.; Iida-Tanaka, N.; Koyama, Y., Efficient in vivo gene transfection by stable DNA/PEI complexes coated by hyaluronic acid. *J. Drug Target.* **2008**, *16*, 276-281.

118. Mummert, M. E.; Mummert, D. I.; Ellinger, L.; Takashima, A., Functional Roles of Hyaluronan in B16-F10 Melanoma Growth and Experimental Metastasis in Mice. *Mol. Cancer Ther.* **2003**, *2*, 295-300.

119. Li, J.; Xue, Y.; Tian, J.; Liu, Z.; Zhuang, A.; Gu, P.; Zhou, H.; Zhang, W.; Fan, X., Fluorinated-functionalized hyaluronic acid nanoparticles for enhanced photodynamic therapy of ocular choroidal melanoma by ameliorating hypoxia. *Carbohydr. Polym.* **2020**, *237*, 116119.

120. Huang, Y.-Q.; Sun, L.-J.; Zhang, R.; Hu, J.; Liu, X.-F.; Jiang, R.-C.; Fan, Q.-L.; Wang, L.-H.; Huang, W., Hyaluronic acid nanoparticles based on a conjugated oligomer photosensitizer: Target-specific two-photon imaging, redox-sensitive drug delivery, and synergistic chemophotodynamic therapy. *ACS Appl. Bio Mater.* **2019**, *2*, 2421-2434.

121. Liang, P.; Shao, J.; Tang, Q.; Si, W.; Wang, Q.; Zhang, Q.; Dong, X., FDPP–HA as a theranostic agent for cancer-targeted fluorescence imaging and photodynamic therapy. *RSC Adv.*

2017, *7*, 37369-37373.

122. Phua, S. Z. F.; Yang, G.; Lim, W. Q.; Verma, A.; Chen, H.; Thanabalu, T.; Zhao, Y., Catalase-integrated hyaluronic acid as nanocarriers for enhanced photodynamic therapy in solid tumor. *ACS Nano* **2019**, *13*, 4742-4751.

123. Kim, S. H.; In, I.; Park, S. Y., pH-responsive NIR-absorbing fluorescent polydopamine with hyaluronic acid for dual targeting and synergistic effects of photothermal and chemotherapy. *Biomacromolecules* **2017**, *18*, 1825-1835.

124. Cai, Y.; Tang, Q.; Wu, X.; Si, W.; Huang, W.; Zhang, Q.; Dong, X., Diketopyrrolopyrrole derivatives grafting hyaluronic acid for targeted photodynamic therapy. *ChemistrySelect* **2016**, *1*, 3071-3074.

125. Misra, S.; Hascall, V. C.; Markwald, R. R.; Ghatak, S., Interactions between hyaluronan and its receptors (CD44, RHAMM) regulate the activities of inflammation and cancer. *Front. Immunol.* **2015**, *6*, 201.

Chapter 2 Synthesis of self-assembled hyaluronan based nanoparticles and their applications in targeted imaging and therapy

2.1 Introduction

Hyaluronan (HA) is a biodegradable and biocompatible linear polysaccharide consisting of disaccharide repeating units of β -1,4-D-glucuronic acid (GlcA)- β -1,3-D-*N*-acetyl glucosamine (GlcNAc) ¹. A major endogenous receptor of HA is the Cluster of Differentiation 44 (CD44) ². CD44 has been found overexpressed on cancer cells and inflammatory cells ^{3, 4}. HA-CD44 interactions are important in cell adhesion, cell migration, induction of hematopoietic differentiation, and signaling for cell activation ⁵. Thus, CD44 can serve as an attractive target for molecular imaging and drug delivery to target cancer as well as inflammation sites ⁶⁻¹⁰. Chemotherapeutic drugs, such as cisplatin ¹¹, paclitaxel ¹², doxorubicin ^{13, 14} have been conjugated to HA for cancer treatment with exciting pre-clinical results against a variety of cancer including breast, colon and ovarian cancer. Furthermore, HA has been conjugated to a variety of nanoparticles (NPs) ¹⁵⁻¹⁸ or used to construct self-assembled NPs ⁷ to alleviate solubility issues associated with hydrophobic drugs such as doxorubicin ¹⁹ and atorvastatin ¹⁰.

With the recognition of the importance of HA-CD44 interactions, there has been significant effort to develop novel compounds capable of binding with CD44 to modulate CD44 biology. The first approach is the fragment-based design of CD44 binders. Nuclear magnetic resonance spectroscopy (NMR) or surface plasma resonance (SPR) -based fragment screening of libraries of small organic molecules has identified novel structures of CD44 binders. While promising, the modest affinities ($K_D \sim \text{mM}$) of these compounds with CD44 ²⁰⁻²² as compared to that of HA ($K_D \sim 21 \mu\text{M}$) ²³ suggest this method is still in its infancy.

A second strategy for the discovery of CD44 binders is based on HA structures. With the rich functional groups present, HA polysaccharide could be chemically functionalized. Mohs and co-workers installed sulfation at the 6-*O* position of GlcNAc or deacetylated GlcNAc of HA ²³. However, both of these modifications decreased the binding of HA toward CD44. In a separate approach, a library of nine HA derivatives based on HA tetrasaccharide was synthesized ²⁴. Following screening of CD44 binding, the derivative with the strongest binding to CD44 was identified with an IC₅₀ value of 322 μ M.

To further enhance the CD44 binding affinity and increase the chance of success in identifying strong binders, one important consideration is the ability to generate a large number of compounds for screening. In this work, we describe a new strategy to synthesize a library of potential binders based on HA polysaccharide structures using the Ugi reaction. The Ugi reaction is a four-component reaction consisting of a carboxylic acid, an amine, an aldehyde, and an isocyanide ²⁵, which can create multiple derivatives in one step by varying the four reaction components. The HA like compounds were screened for their abilities to bind with CD44 *via* competitive enzyme linked immunosorbent assay (ELISA) and SPR. The lead compound exhibited significantly enhanced binding with CD44 compared to HA polysaccharide. Furthermore, it has much stronger interactions with CD44 expressing *Raw* 264.7 cells, highlighting its potential in aiding biological investigations.

2.2 Results and discussions

2.2.1 Synthesis of the library of 36 HA like polysaccharides via the Ugi reaction

As shown in **Figure 2.1a**, our design of Ugi reaction on HA (MW = 10 kDa) involved the usage of the carboxylic acid functionality of HA. Nine amines (numbered A to I), four aldehydes (numbered 1 to 4) and cyclohexyl isocyanide were used as components for Ugi reactions. As a

result, 36 different HA derivatives were synthesized combinatorially. Only aliphatic aldehydes were used due to the lower reactivities of aromatic aldehydes²⁶. While Ugi reactions on aromatic aldehydes can be promoted by a titanium based catalyst²⁶, it is not applicable to our synthesis due to the need to use water as a solvent to solubilize HA and the instability of the catalyst in water.

For the selection of aliphatic aldehyde, formaldehyde was chosen since it is the simplest form of aldehyde. Other aldehydes such as iso valeraldehyde and propionaldehyde was chosen as well. Since the interaction between HA and CD44 was primarily through H bonding, introduction of fluorine may strengthen H bonding due to high electronegativity of fluorine. For this reason, heptafluorobutyraldehyde was chosen. For the selection of amine, amine without aromatic group was chosen, including ethanolamine, 3-amino-1-propanol, amylamine and cycloheptylamine. The introduction of -OH group from ethanolamine or 3-amino-1-propanol may strengthen H bond binding. Amine with aromatic group, including benzylamine, 3-phenyl-1-propylamine, 4-phenylbutylamine was chosen, while varying the spacer between amine functionality and phenyl group. Tyramine and Tyramine are also chosen for different aromatic group.

The Ugi reactions were first performed in a 96-well microtiter plate at 10 mg HA scales. Equal molar of carboxylic acid, amine, aldehyde, and isocyanide were mixed in H₂O / EtOH (1 : 1) cosolvent. pH value of the reaction was adjusted to 3 with the addition of HCl solution. The reaction was allowed to proceed for 12 hours, followed by pH adjustment to 10 with the addition of aqueous NaOH solution to hydrolyze the carboxylic ester byproducts due to the Passerini reaction between HA, the isocyanide and the aldehyde. The HA derivative from the Ugi reaction was precipitated out from the reaction mixture after the addition of EtOH followed by five washes with EtOH to remove unreacted small molecules. The precipitate was collected and subject to dialysis for 48 hours (3 kDa cutoff) to further remove any impurities. ¹H-NMR analysis of the

products confirmed successful Ugi reactions on all 36 components. As an example, as shown in **Figure 2.1b** for compounds G2 (G2 denotes the HA derivative formed through Ugi reaction involving HA, 3-phenyl-1-propylamine (amine G), formaldehyde (aldehyde 2), and cyclohexyl isocyanide), compared to the unmodified HA polysaccharide (**Figure 2.1c**), there are additional ^1H -NMR resonances supporting the addition of small molecules, which appeared broadened consistent with their attachment to HA polysaccharide backbone. Peaks from 0.9 ppm to 1.8 ppm resulted from the cyclohexyl moiety. Signals from 7.0 ppm to 7.5 ppm were due to the aromatic protons from the amine. The integration value of anomeric protons from HA around 4.3 ppm was set to 2, with those from the acetyl group set to 3. In the case of G2, the level of modification was determined by NMR integration of aromatic protons from 7.0 ppm to 7.5 ppm, which was about 18% per disaccharide repeating unit. The loading percentage of HA derivatives produced in this method has loading percentage between 15% and 20%. As a comparison, the reactions were carried out without the amine or the aldehyde component at $\text{pH} = 3$. Furthermore, parallel reactions were carried out at $\text{pH} = 10$ with all four components required for Ugi. In all these control reactions, unmodified HA was recovered after purification, which indicates the complete removal of unreacted small molecular weight components from the reaction mixture following our purification protocol and the pH-dependent behavior of Ugi reaction.

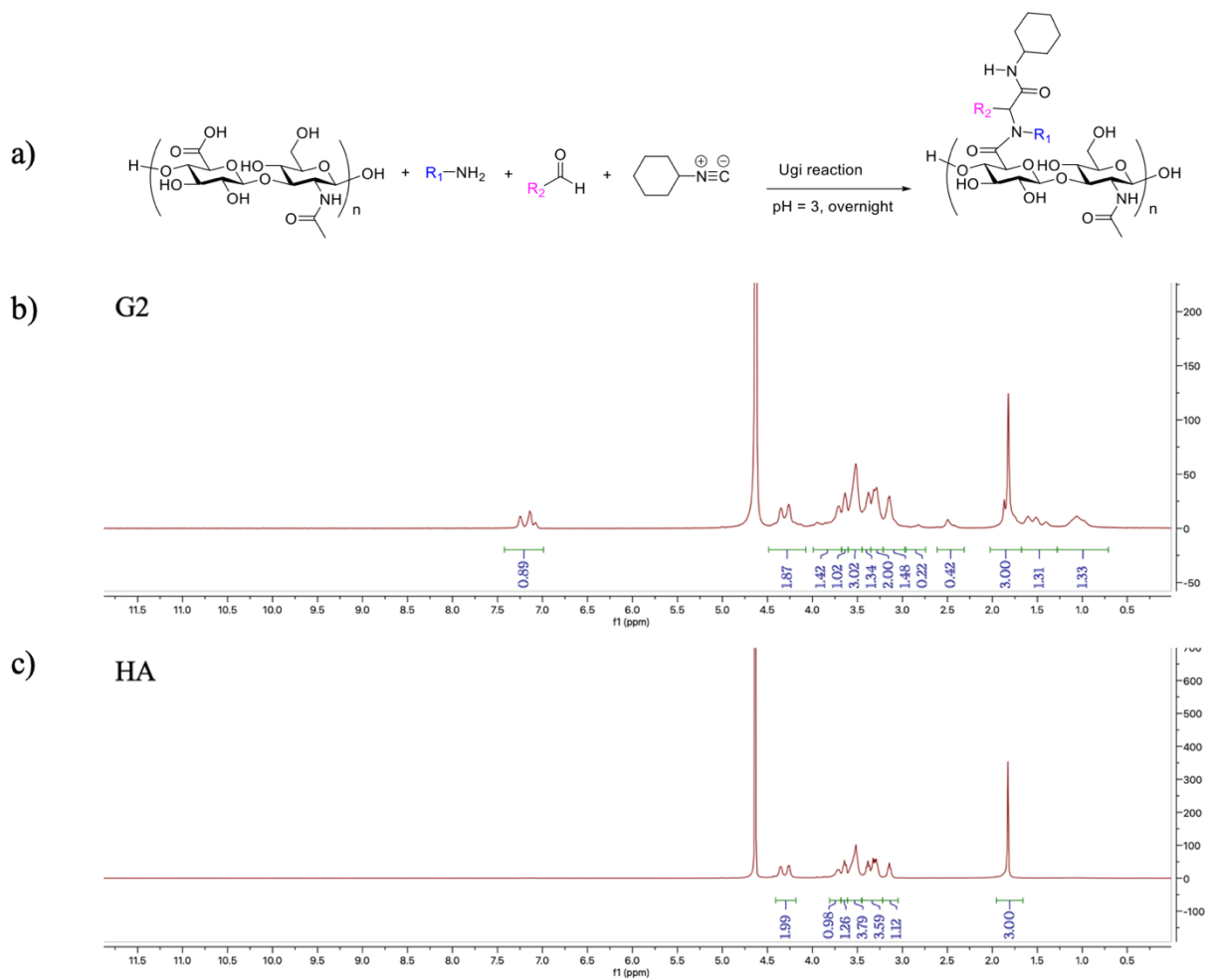


Figure 2.1 Synthesis of HA like polysaccharides via the Ugi reaction. a) Ugi reaction scheme.

Nine different amines (benzylamine, ethanolamine, 3-amino-1-propanol, amylamine, cycloheptylamine, 4-phenylbutylamine, 3-phenyl-1-propylamine, tryptamine, and tyramine), four different aldehydes (heptafluorobutyraldehyde, formaldehyde, isovaleraldehyde and propionaldehyde), and cyclohexyl isocyanide were used to produce HA derivatives. b, c) ^1H -NMR spectra of G2 and HA. G2 corresponds to HA modified through the Ugi reaction with 3-phenyl-1-propylamine (amine G), formaldehyde (aldehyde 2), and cyclohexyl isocyanide. Resonance between 1.0 ppm and 1.7 ppm are from the cyclohexyl rings. Peaks between 7.0 ppm and 7.5 ppm are from the phenyl ring of the amine. The level of modification was estimated as 18% according to the integration value of ^1H -NMR signals between 7.0 ppm and 7.5 ppm.

2.2.2 Binding of HA like polysaccharides with CD44 via competitive ELISA

With the HA-like polysaccharides in hand, their abilities to bind CD44 were investigated via a competitive ELISA ²⁴. Biotinylated HA (b-HA) was synthesized ²⁷ and added to ELISA wells coated with the CD44 HA binding domain (HABD). Upon washing off unbound b-HA, the

amounts of b-HA bound to CD44 HABD could be semi-quantified by the optical density (OD) changes upon addition of streptavidin conjugated with horseradish peroxidase (HRP). To evaluate the affinity of HA polysaccharide to CD44 HABD, HA (10 kDa) was added together with b-HA to CD44 HABD coated ELISA wells. The HA would compete against b-HA for CD44 binding, thus reducing the amount of b-HA bound to the plate leading to lower OD values in the wells.

The potency of the HA like polysaccharides synthesized to inhibit b-HA binding was compared to that by the unmodified HA at 0.32 μ M concentration. The percentage of inhibition % was calculated by subtracting the OD value with HA or the HA like polysaccharide from that without competition divided by the OD value without competition (**Equation 1**). Inhibition % change value was calculated by subtracting the % of inhibition by unmodified HA from the % of inhibition by HA like polysaccharide. A positive inhibition change value would indicate the HA like polysaccharide has a higher affinity with CD44 than the unmodified HA polysaccharide.

$$\text{Inhibition \%} = \frac{\text{OD without competition} - \text{OD with HA or HA like polysaccharide for competition}}{\text{OD without competition}} \times 100\%$$

Equation 1. Formula for calculation of inhibition % values.

The inhibition % change values of HA like polysaccharides were shown in **Figure 2.2** as a heat map. Many of the derivatives have reduced binding to CD44 compared with HA as suggested by the green color in the heat map. Among the four aldehydes explored, only aldehyde 2, i.e., formaldehyde, yielded HA like polysaccharides with positive inhibition changes, i.e., producing derivatives with stronger CD44 binding. This suggests the CD44 binding site prefers to have a small group on the carbon center immediately adjacent to the amide moiety formed by the Ugi reaction.

		A	B	C	D	E	F	G	H	I
1		-13%±6%	-9%±7%	-6%±1%	0%±1%	-7%±1%	1%±2%	-6%±0%	-1%±1%	3%±1%
2		-14%±6%	3%±11%	2%±0%	11%±1%	-26%±2%	38%±1%	38%±0%	22%±0%	23%±1%
3		-10%±0%	-14%±6%	-23%±3%	-17%±0%	-23%±0%	-6%±2%	4%±2%	4%±6%	-22%±4%
4		-13%±4%	-11%±0%	-18%±3%	-15%±0%	-10%±0%	-8%±1%	-5%±2%	-8%±1%	-25%±3%

inhibition difference	< -15%	-15% to -5%	-5% to 5%	5% to 25%	> 25%
	Green	Light Green	Grey	Red	Dark Red

Figure 2.2 Heat-map of inhibition % changes of various HA derivatives. A positive inhibition change value would indicate the HA derivative has enhanced affinity toward CD44. Red color represents enhanced affinity, while green color represents decreased affinity with the average and standard deviation from three samples shown (N = 3). While the vast majority of the compounds show lower binding as represented by the negative inhibition % change values, F2 and G2 exhibited the highest enhancement in CD44 binding.

For the amine structures, when amines A, B, C and E were used, all HA derivatives formed have lower binding toward CD44, suggesting these amines did not enhance CD44 affinity. In contrast, F2 and G2 were identified with strong binding with the structures of F2 and G2 only differing by one methylene moiety (**Figures 2.3a**). Interestingly, A2 has two fewer methylene groups compared to G2. Yet A2 is far less potent in CD44 binding.

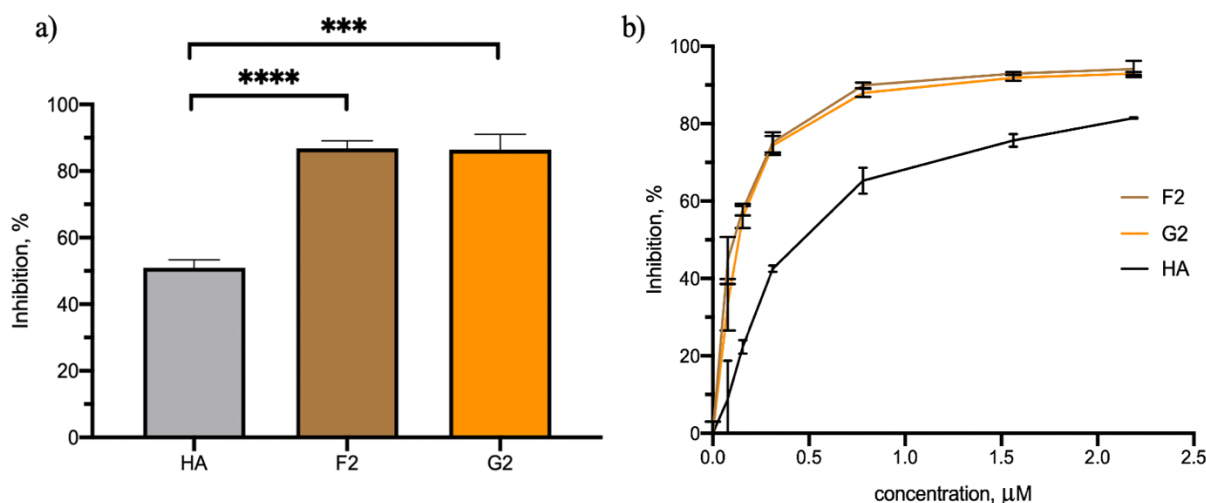


Figure 2.3 a) Competitive ELISA results for F2, and G2. F2 and G2 showed more potent competition against b-HA for CD44 binding as compared with HA polysaccharide (10 kDa). Statistical test was performed through one way ANOVA. *** $p < 0.001$; **** $p < 0.0001$. b) Dose-dependent inhibition of HA (10 kDa), F2 and G2 at various concentrations. The inhibition % was calculated following **Equation 1**. The average values and the standard deviation from three samples are shown ($N = 3$).

Dose-dependent inhibition of HA by G2 and F2 was measured at various concentrations, as shown in **Figure 2.3b**. At all concentrations examined, G2 and F2 consistently demonstrated significantly stronger inhibition compared with HA. The IC₅₀ value (the concentration of HA leading to 50% reduction of the binding of b-HA to CD44 immobilized to the surface) of HA interaction with CD44 HABD was determined to be 0.5 μ M. The IC₅₀ value for F2 and G2 was determined to be 0.1 μ M, which is a five-fold reduction compared with that of unmodified HA.

2.2.3 Effect of loading percentage on binding of HA derivatives

Carboxyl group plays important role in hyaluronic acid binding to CD44²⁸. Ugi modification on the carboxyl group may significantly change the structure of HA such that interaction of HA with CD44 protein through the carboxyl group is no longer viable. Therefore, we investigated the effect of loading percentage of compounds B2 and G2 on CD44 binding, as shown in **Figure 2.4**. When the loading percentage was 11%, B2 had slightly stronger binding.

When the loading percentage was between 30% and 60%, B2 had similar binding ability as HA (~50%). However, when the loading percentage went up to 70% or 90%, B2 showed significantly lower binding. This is consistent with the idea that the carboxyl group plays critical roles for CD44 binding, and that the loading percentage should not be higher than 60%. The lead compound G2 with different loading percentages was synthesized as well. As the loading percentage increased to 38%, the G2 derivative had higher inhibition, suggesting its higher affinity with CD44.

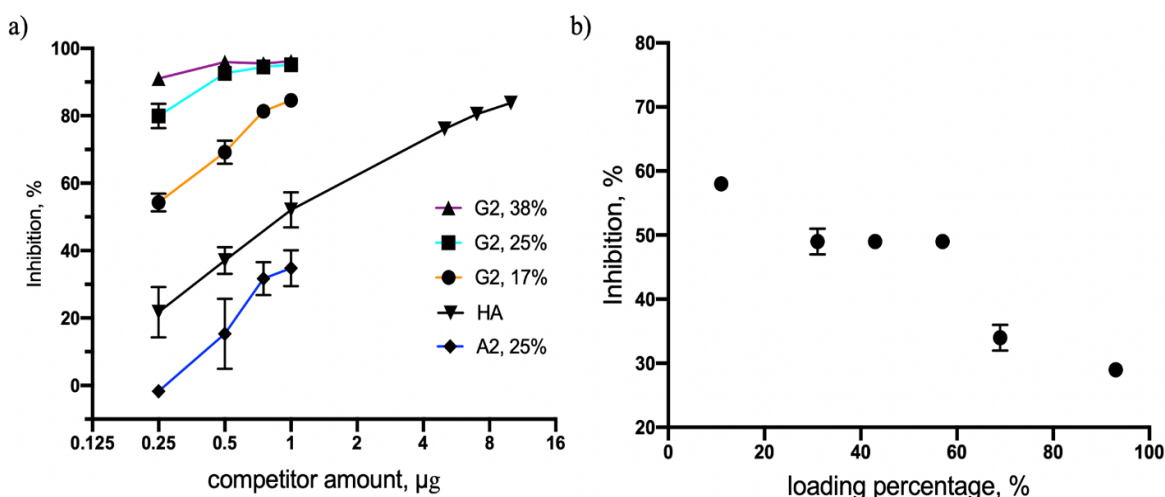


Figure 2.4 Binding evaluation of compounds B2 and G2 at various loading percentage. HA derivatives at different loading percentages were synthesized with various stoichiometry ratio. a) Lead compound G2 was synthesized at different loading percentage. It was found that loading percentage up to 38% of compound G2 showed significantly stronger competition. A2 at 25 % was shown as a negative sample for comparison. b) For compound B2, loading percentage lower than 55% did not decrease its binding much. Significant binding decrease was observed then the loading percentage was above 65%. The average values and the standard deviation from three samples were shown ($N = 3$).

2.2.4 Effect of isocyanide on binding of HA derivatives

While the 36 membered library (**Figure 2.2**) was constructed using cyclohexyl isocyanide, we investigated into other potential isocyanides to synthesize G2 like HA derivatives, as shown in **Figure 2.5**. Butyl isocyanide or pentyl isocyanide was combined with formaldehyde and 3-phenyl 1-propyl amine (same components as in G2 modifications) for Ugi reaction on HA, leading to G2-

butyl isocyanide and G2-pentyl isocyanide with about 40% loading. The G2 derivative formed with the cyclohexyl isocyanide gave strongest inhibition. Comparing butyl and pentyl isocyanide, as the length of carbon chain increased, the binding decreased. In contrast, the cyclic cyclohexyl group helped enhance the CD44 affinity. For the ease of discussion, we use G2 to refer to G2 HA derivatives formed with the cyclohexyl isocyanide.

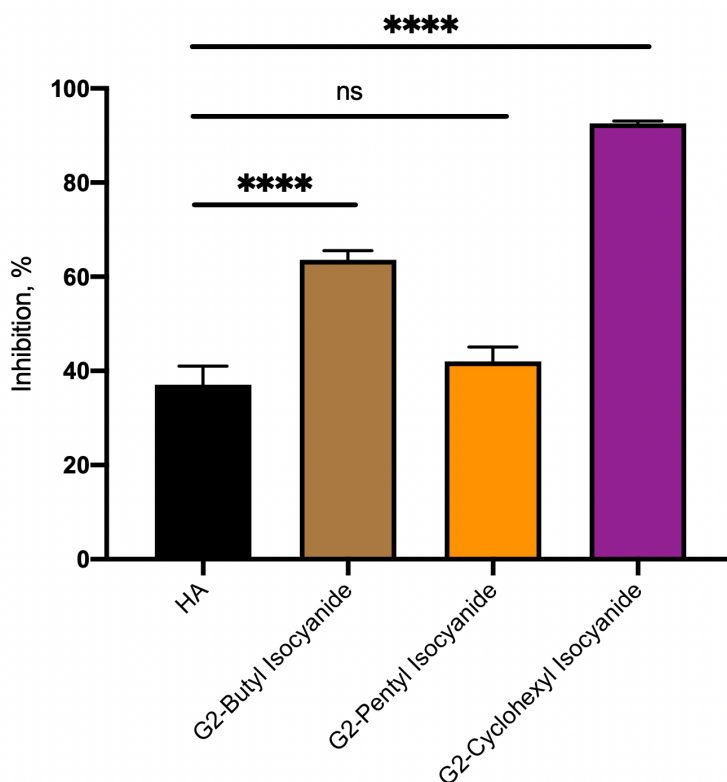


Figure 2.5 Evaluation of G2 derivatives formed with different isocyanides. 0.5 μ g HA or derivatives was used to compete against 0.5 μ g b-HA. The loading percentage of all three modification was around 30%. Modification using cyclohexyl isocyanide yielded the G2 derivatives with the highest binding, compared with derivatives modified with butyl or pentyl isocyanide. The average values and the standard deviation from three samples were shown (N = 3). Statistical test was performed through one way ANOVA. **** $p < 0.0001$.

2.2.5 Effect of molecular weight on binding of HA derivatives

While the library was synthesized using 10 kDa HA, we investigated the impact of the molecular weight of HA. G2 derivatives with HA backbones with molecular weights of 60 kDa and 100 kDa were synthesized. As shown in **Figure 2.6** higher molecular weight HA at 60 kDa

and 100 kDa show more competition compared to the corresponding derivative with the 10 kDa HA backbone at equivalent weight, probably due to the enhanced multivalency effect in CD44 binding associated with higher molecular weight. G2 derivatives with 60 kDa and 100 kDa HA consistently showed stronger binding compared with unmodified HA.

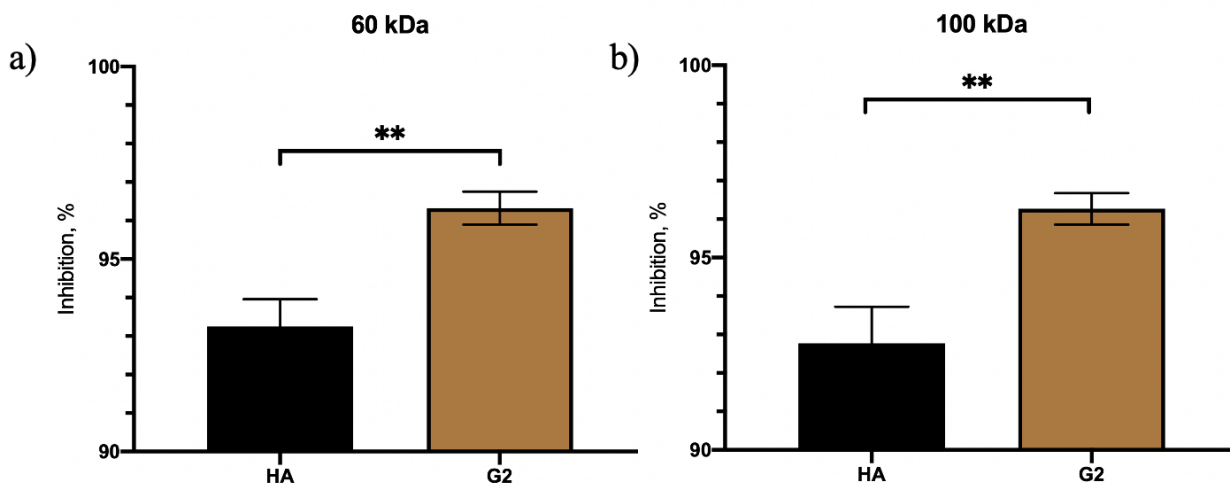


Figure 2.6 G2 modification using higher molecular weight of HA, a) 60 kDa and b) 100 kDa. G2 derivatives with 60 kDa and 100 kDa HA backbone had stronger inhibition than the corresponding HA polysaccharides. Competition was set at 0.1 μ g of equal weight of competitor for either HA or G2. Statistical test was accomplished with two-tailed unpaired t-test. ** $p < 0.01$.

2.2.6 Cytotoxicity evaluation of G2 modification

To establish the potential of using G2 in biological setting, cytotoxicity of G2 at various loading percentage was evaluated using the MTS cell proliferation assay, as shown in **Figure 2.7**. For all loading percentage, G2 showed minimal cytotoxicity up to 100 μ g/mL.

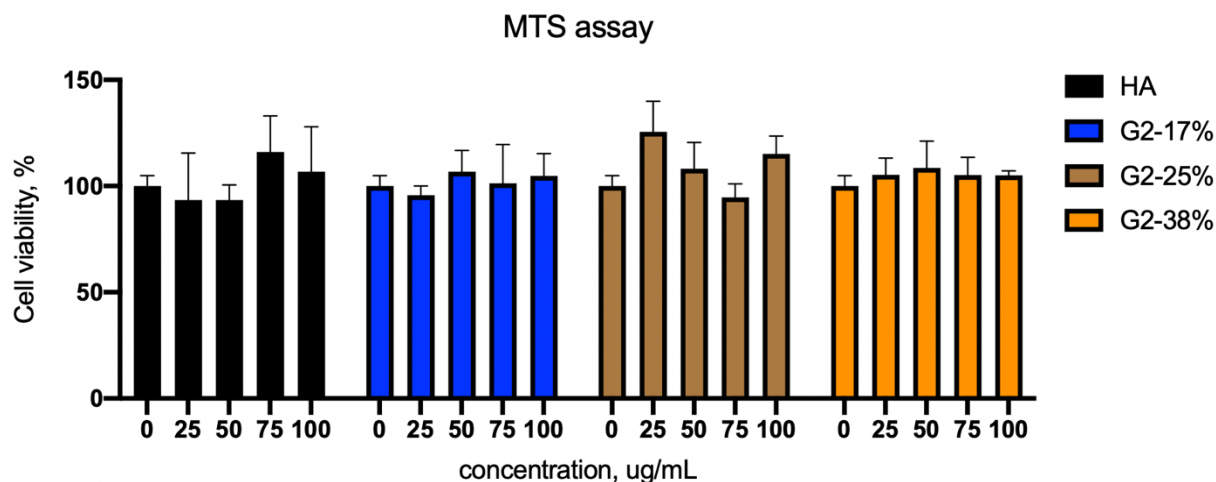


Figure 2.7 Cytotoxicity evaluations of G2 of different loading percentage at various concentrations. G2 showed no cytotoxicity at all loading percentage and concentrations evaluated.

2.2.7 Binding of HA like polysaccharides with CD44 via SPR

To confirm the ELISA results, SPR experiments were carried out. SPR has been used previously to characterize binding involving the CD44 HABD in two different ways ²². In the first approach, the CD44 HABD protein was immobilized onto SRP sensors. HA was then flowed over the CD44 coated surface, and the mass change upon binding triggered the SPR signal changes as measured in response units (RUs). This assay has been successfully applied to determine K_D values of both small molecule fragments and short HA oligosaccharides binding with CD44 HABD ²². However, HA polysaccharides and all the HA like polysaccharides behaved very differently than small molecules in this assay. HA was slow to reach equilibrium binding, particularly at low concentrations, and washed off the surface even more slowly. This is likely due to fluidic properties arising from the polymeric nature of HA and the potential for high avidity with multiple (but unnumbered) sites for interaction with immobilized CD44. Moreover, high binding to the unmodified dextran surface of the CM5 chip was observed in the reference channels of the SPR sensor that further complicated data analysis.

As an alternative, HA can be immobilized on the sensor surface with CD44 HABD flowed over this surface to bind with HA ²². To determine the integrity of the chip surface, various concentrations of CD44 HABD (0-150 μ M) in HEPES-EP buffer (pH 7.4, 150 mM NaCl, 3 mM EDTA, 0.005% (v/v) surfactant P-20) were passed over the SPR sensor coated with HA polysaccharide. An apparent K_D could be calculated for the affinity of CD44 to the chip surface and previous work showed that small molecules could specifically affect the apparent K_D values. Small molecules capable of competing with HA for binding with CD44 on the chip surface was used to calculate the IC_{50} values of the small molecules. As a positive control, HA deca-saccharide (HA-10) in a two-fold dilution series (250 μ M – 1.95 μ M) was incubated with a fixed concentration of CD44 (~17 μ M). An IC_{50} value of 32 μ M was determined for HA-10 that was close to previously published value of 48 μ M ²². However, upon introducing the HA polysaccharide (10 kDa) to the same flow experiments, problems with fluid control, binding kinetics, reference surface affinity and avidity arose complicating both data collection and analysis.

To address the aforementioned challenges encountered in SPR, a reference subtraction strategy was devised to decipher CD44 related binding. For HA, F2, and G2, a complete set of sensograms was collected for both a two-fold dilution series without any CD44 HABD, and an identical series with preincubation with CD44 HABD (17 μ M) was obtained. Reference subtracted sensograms reflecting CD44 binding to the surface were generated by subtracting curves obtained without CD44 from those with CD44 (**Figures 2.13-2.14**). This approach enabled us to compute IC_{50} values from each reference-subtracted series of SPR sensograms.

To benchmark the inhibition potency by the HA like polysaccharide, the relative percentage inhibition was calculated by dividing the IC_{50} value of HA obtained from SPR measurements over the corresponding IC_{50} value of the F2 or G2, at loading percentage of 17%.

A relative inhibition percentage greater than 100 % would suggest tighter binding to CD44 HABD compared to the native HA. As shown in **Figure 2.8**, G2 at 17% loading demonstrated significantly greater inhibitory potential than HA polysaccharide as they bind tighter to the HABD, with a 37% increase in relative % inhibition. These results support the stronger binding of G2 from the aforementioned competitive ELISA data (**Figure 2.2**).

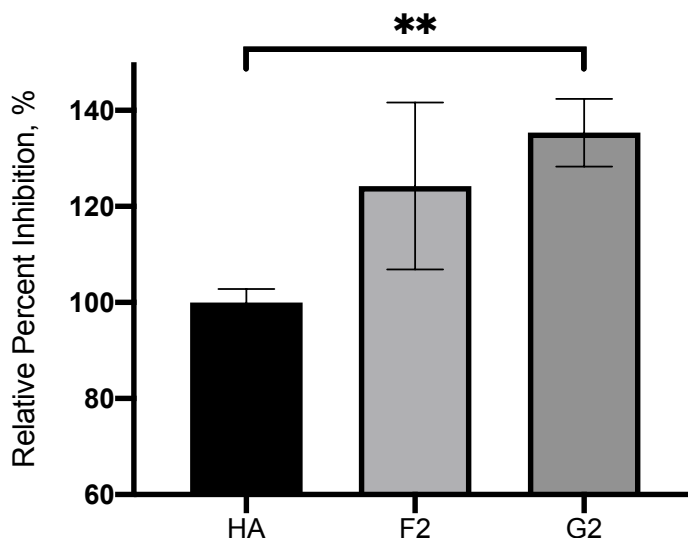


Figure 2.8 Inhibition % of F2 and G2 relative to HA toward CD44 binding based on the SPR data. The error bars depict the standard deviation of the observations collected (N = 3). G2 demonstrated a 37% increase in relative percentage of inhibition. The average values and the standard deviation from three samples are shown. Statistical test was accomplished with two-tailed unpaired t-test. ** $p < 0.01$.

2.2.8 In vitro evaluation of G2 using Raw 264.7 cells

With the stronger binding of HA derivative confirmed, we investigated next the potential biological applications of G2 at 17% in cellular targeting. To monitor cellular interactions *via* fluorescence, the fluorescein isothiocyanate (FITC) fluorophore was conjugated to both G2 and HA presumably through the reaction of the hydroxyl group and isocyanate group. Based on fluorescence quantification, on average each polymer chain has 0.6 FITC molecule for HA, and 1.3 FITC molecule for G2. Competitive ELISA was carried out for HA-FITC and G2-FITC, which

confirmed that G2-FITC has stronger binding than HA-FITC suggesting that derivatization with the fluorophore does not impact the relative potency of G2 vs HA (**Figure 2.9**).

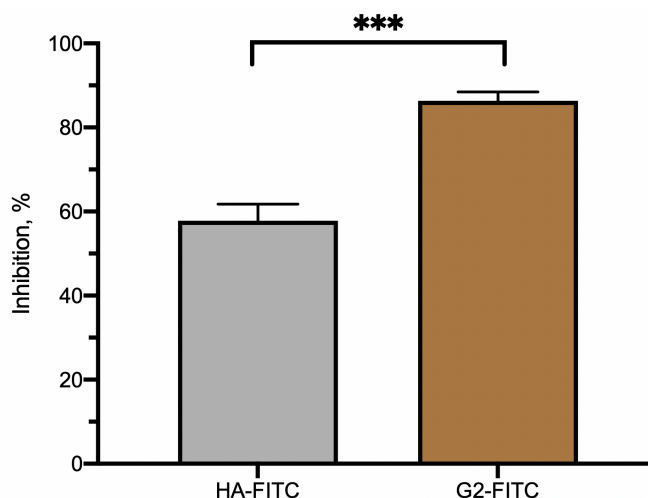


Figure 2.9 Competitive ELISA confirmed that G2-FITC has stronger binding to CD44 compared with HA-FITC. Equal concentrations of HA-FITC and G2-FITC were added to compete with b-HA. ELISA showed that G2-FITC bound stronger to CD44 as compared to HA-FITC. It also indicates that FITC attachment does not impact the relative competition potency of HA and G2. The average values and the standard deviation from three samples are shown. Statistical test was accomplished with two-tailed unpaired t-test. *** $p < 0.001$.

Cellular uptake experiments were performed next using Raw 264.7 macrophage cells, which are known to express CD44 on cell surface ⁹. HA-FITC and G2-FITC at the same fluorescence intensities were incubated with Raw 264.7 cells for 1.5 hours. Three samples of HA-FITC and G2-FITC at the same fluorescence intensities were examined. Upon completion of incubation, unbound ligands were removed by thorough washing, and the amounts of polysaccharides associated with the cells were quantified by flow cytometry. As shown in **Figure 2.10**, G2 consistently showed better cellular binding compared with HA at all concentrations examined.

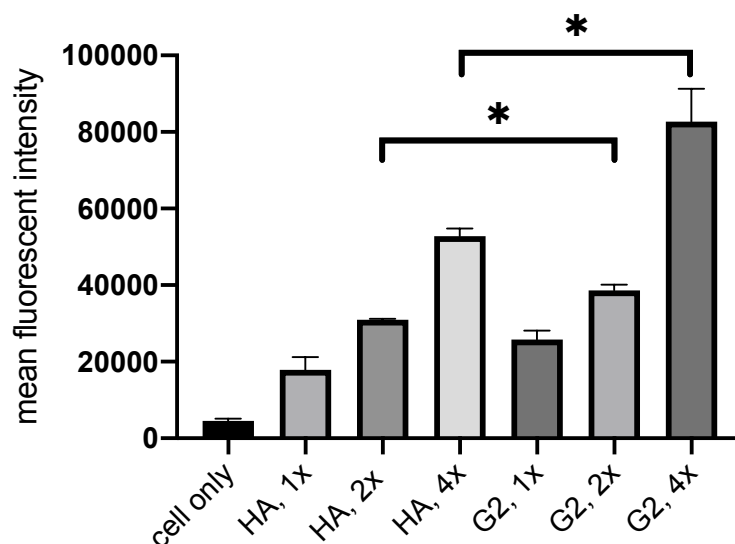


Figure 2.10 G2-FITC and HA-FITC at three concentrations were incubated with Raw 264.7 cells. 1x concentration corresponds to HA at 25 $\mu\text{g/mL}$. For cells only group, no HA or G2 was added, and the mean fluorescence intensity was low. Cells incubated with G2-FITC exhibited stronger fluorescence compared with those incubated with HA-FITC across three different concentrations. The average values and the standard deviation from three samples are shown. Statistical test was carried out with a two-tailed unpaired t-test. * $p < 0.05$.

To better understand the fate of the HA like polysaccharides upon cellular binding, confocal microscopy studies were performed on the cells following incubation with G2-FITC. As shown in **Figure 2.11**, significant green color was observed inside the cells with extensive co-localization with the red lysotracker stain suggesting that G2 was taken up by the cells into lysosomes. The fluorescence staining patterns of cells incubated with G2-FITC were similar to those with HA-FITC indicating they have similar cellular distribution. Thus, G2 can be uptaken up into cells, which bodes well for its future applications in targeted intracellular drug delivery.

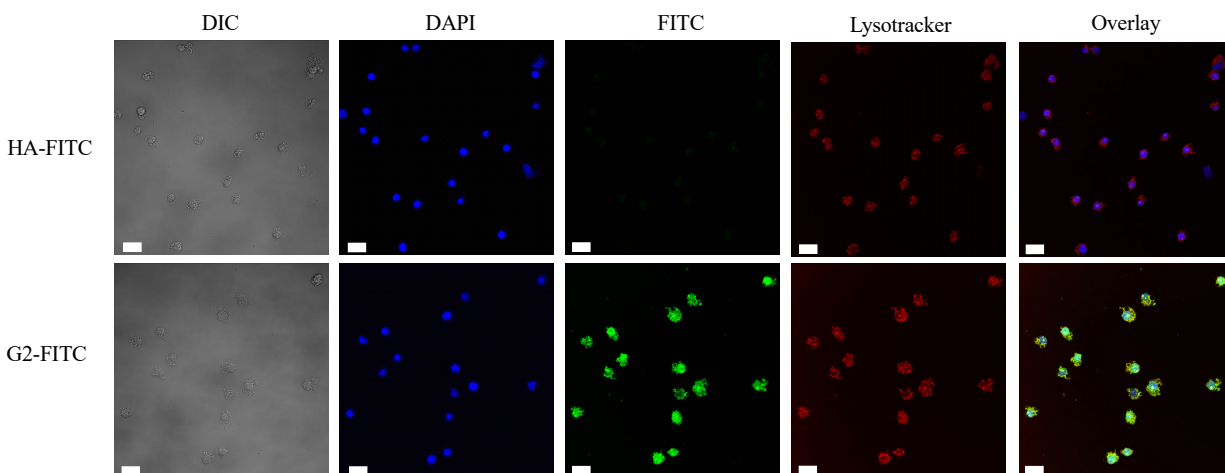


Figure 2.11 Confocal imaging confirms the uptake of G2 and HA in Raw 264.7 cells. Blue DAPI channels show the locations of nuclei; green FITC channels show the locations of the HA or G2; red lysotracker channels show the locations of the lysosomes. Combined image is the overlay of DAPI, green FITC and the red lysotracker channels.

2.2.9 Data analytics with ELISA library data

Machine learning has been an increasingly useful tool for analyzing library data generated through combinatorial chemistry ²⁹. It can help to find inherent structure within the dataset and yield predictions based on explored chemical space. For the current study, we subjected the inhibition % change data (**Figure 2.2**) to a machine learning algorithm, with the features being different types of the amine and the aldehyde, and the label being the inhibition % change. For the feature, categorical input data such as amine and aldehyde structure was converted into numerical vector using one-hot encoding, as shown in **Figure 2.12** ³⁰. As a result, the input size is 13, and the output size is 1. The dataset is randomly shuffled with 25 of the data points as the training set and the remaining 11 as the test set. Linear regression was evaluated using scikit-learn ³¹ with Google Colab (**Tables 2.2-2.3**). As shown in **Table 2.1**, the model accurately predicted the signs of the inhibition change of 9 out of 11 data points, with mean absolute error (MAE) to be 5.58. It should be noted that compound G2 is correctly predicted to have stronger binding. This demonstrated the practicality of using machine learning tools to analyze library synthesis data for

HA or other carbohydrate polymers. However, two limitations with this dataset are the relatively small size of dataset, and the significantly more negative output values of inhibition change % than the number of positive values.

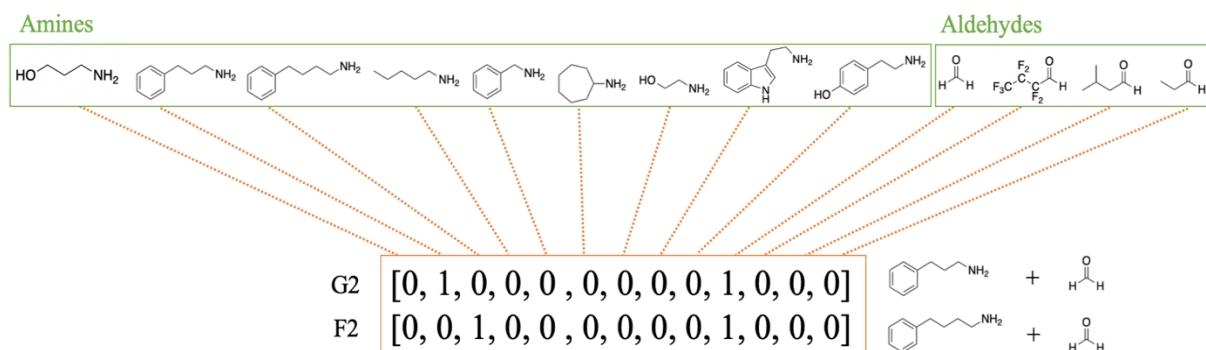


Figure 2.12 Vector representation of library data was accomplished through one-hot encoding. The input size is 13, corresponding to 9 different amines and 4 different aldehydes.

Compound ID	Amine	Aldehyde	Experimental Inhibition change (%)	Predicted inhibition change (%)
A4	Benzylamine	Propionaldehyde	-13	-24
B2	Ethanolamine	Formaldehyde	3	7
B3	Ethanolamine	Isovaleraldehyde	-14	-16
B4	Ethanolamine	Propionaldehyde	-11	-19
D1	Amylamine	Heptafluorobutyraldehyde	0	-7
D2	Amylamine	Formaldehyde	11	9
E3	Cycloheptylamine	Isovaleraldehyde	-23	-24
G2	3-Phenyl-1-propylamine	Formaldehyde	38	23
G3	3-Phenyl-1-propylamine	Isovaleraldehyde	4	0
H2	Tryptamine	Formaldehyde	22	20

Table 2.1 Machine learning model prediction for 11 data points randomly selected as the test set. Their corresponding inhibition change, and predicted inhibition changes were shown. The model was able to predict the sign of inhibition change for 9 out of 11 data points in the test set.

2.3 Conclusions

In summary, a library of 36 HA derivatives was synthesized readily using the Ugi reaction and screened for CD44 binding through competitive ELISA. Two lead compounds F2 and G2 were identified with significantly enhanced affinities with CD44 by ELISA. SPR further confirmed enhanced CD44 binding of G2. Validation of lead compound G2 was carried out: 1) improves binding for 10 kDa, 60 kDa and 100 kDa HA; 2) shows stronger binding at higher loading

percentage up to 38%; 3) does not show cytotoxicity on *Raw 264.7* cells; 4) improve cellular uptake on *Raw 264.7* cells; Machine learning algorithm was used to evaluate inherent structure within the dataset, with accuracy over 80% for data points in the test set. Thus, the Ugi reaction is a promising strategy to modify HA to develop novel CD44 binders with significantly enhanced affinities.

2.4 Experimental section

2.4.1 Reagents

Sodium hyaluronan (10 kDa) was purchased from Lifecore Biomedicals. Amines, aldehydes and isocyanides were obtained from Sigma unless otherwise stated. Full-length human CD44 HABD cDNA was a gift of Dr. James B. McCarthy at the University of Minnesota (Minneapolis, MN). Rosetta 2(DE3)pLysS competent cells were purchased from EMD Biosciences (Gibbstown, NJ). HiPrep 16/60 Sephacryl S-100 HR was obtained from GE Healthcare (Piscataway, NJ). CM5 and SA Biacore Sensor Chips were obtained from GE Healthcare (Piscataway, NJ). L-Arginine, reduced/oxidized glutathione, coupling reagents, and other general buffer reagents were from Sigma-Aldrich (St. Louis, MO). Hydrazide biotin linker for synthesizing biotinylated HA was from Thermo Scientific (Rockford, IL).

2.4.2 Batch synthesis of HA derivatives on 96-well plate

In each well of a 96-well plate, an HA aqueous solution (150 μ L, 0.025 mmol of carboxyl group) and an amine solution in ethanol (20 μ L, 0.025 mmol) were added. Hydrochloric acid (20 μ L 1.4M) was added to adjust the pH to 4. The aldehyde solution in ethanol (20 μ L, 0.025 mmol), cyclohexyl isocyanide solution in ethanol (20 μ L, 0.025 mmol) and ethanol (100 μ L) were added. The plate was kept on a shaker for 12 hours. An aqueous solution of NaOH (30 μ L, 0.5M) was added to each well to adjust the pH to about 10 to allow for the hydrolysis of ester byproduct from

Passerini reaction. The reaction mixture was then dialyzed (MWCO: 3.5 kDa) against MilliQ water for purification. Lead compounds identified through ELISA was resynthesized using 10 mL glass vials as the reaction vessel under vigorous stirring. Stoichiometric ratio of 1 : 1 : 0.25 : 1 (acid : amine : aldehyde : isocyanide) for synthesis of individual HA derivative led to similar level of HA functionalization (15% to 20%) as the compound synthesized in the 96 well plate.

2.4.3 Synthesis of individual HA derivative

HA (10 mg, 10 kDa, 60 kDa or 100 kDa) was dissolved in MilliQ water (600 μ L) in a 17 mL glass vial. Then ethanol (400 μ L) was added. Amine solution in ethanol (20 μ L, 0.025 mmol) were added followed by addition of hydrochloric acid (20 μ L 1.4M) to adjust the pH to 4. The aldehyde solution in ethanol (10 μ L, 0.0125 mmol) and cyclohexyl isocyanide solution in ethanol (20 μ L, 0.025 mmol) were added. The reaction was allowed proceeded for 1 hour under vigorous stirring. 50 μ L of 2 M sodium carbonate was added to adjust pH to 10 and kept stirring for overnight to allow for hydrolysis of ester by product. The reaction mixture was then dialyzed (MWCO: 3.5 kDa) against MilliQ water for two days. Different stoichiometry ratio can be adjusted by using various amounts of aldehyde while keeping the amount of other components the same.

2.4.4 Competitive ELISA

In a 96 well-plate, 100 μ L of goat antihuman IgG FC γ (3 μ g/well, Millipore, cat no. AP113) in PBS buffer was added to each well. The plate was covered with aluminum foil and incubated at 4 °C overnight. The wells were then washed 3 times with 200 μ L PBST buffer (0.5% Tween 20) as follows: the plate was emptied by inversion over a sink, tapped against some layers of soft paper tissue to remove residual liquid, and then washed with buffer repeatedly (insufficient washings may lead to a high background). Blocking was completed by adding 5% BSA in PBS (200 μ L) to each well followed by incubation at 37 °C for 2 h. The plate was then washed as described above.

100 μ L of CD44-FC γ chimera (0.2 μ g/well, R&D systems, cat no. 3660-CD) in PBS buffer was then added to each well and incubated at 37 °C for 45 min. The plate was washed 3 times with 200 μ L PBST buffer (0.05% Tween 20) as before. 100 μ L of b-HA (0.5 μ g/well) and 100 μ L HA 10 kDa (1 μ g/well) were then added to each well and incubated at room temperature for 2 h. The plate was then washed 3 times with 200 μ L PBST buffer (0.05% Tween 20) and twice with PBS buffer. 100 μ L Avidin-HRP in 0.2% BSA-PBS solution was then added to each well and incubated at room temperature for 1 h. The plate was then washed 3 times with 200 μ L PBST buffer (0.05% Tween 20) and twice with PBS buffer. 100 μ L of chromogenic TMB solution was added to each well, homogenized, and incubated for 15 min, or until a blue color appeared. The plate should be protected against light during this incubation. The reaction was then quenched by adding 0.5 M H₂SO₄ (50 μ L) to each well. For quantitative measurements, it was important that each well was incubated for exactly the same length of time. Optical absorbance was directly assessed through the bottom of the microwell plate using an automated ELISA plate reader (Biorad) at 450 nm.

2.4.5 MTS assay

Raw 264.7 cells were dispersed in DMEM cell culture media containing FBS (10 %) and cultured in a 96-well plate in the presence of 5 % CO₂ at 37 °C. Then, cells were incubated with various concentrations of HA or HA derivatives for 2 hours. The media was removed, and MTS reagent (Promega, cat no. G358C) dispersed in medium (10 %) was added and incubated for another 2 hours until the color was developed. The absorption of each well was measured at 490 nm using a SpectraMax M3 plate reader. Wells without cells (blanks) were subtracted as background from each sample.

2.4.6 Cellular uptake of HA and G2 with Raw 264.7 cells

To conjugate FITC onto HA and derivatives, 2 mg HA or G2 was mixed with 0.44 mg FITC at 1 : 5 molar ratios. The reaction was allowed to proceed for 2 days, followed by dialysis (MWCO: 3.5 kDa) in PBS for one day and in MilliQ water for 3 days to remove free FITC. *Raw 264.7* cells were used to evaluate the uptake of G2 and HA. *Raw 264.7* cells were cultured in a 96-well plate in DMEM cell culture media containing FBS (10%) for 24 h at 37 °C and 5% CO₂. HA and G2 at equivalent fluorescence amounts were dispersed in DMEM, added to the cells and incubated for 1.5 h at 37 °C and 5% CO₂. The cell culture medium was removed, and cells were washed with PBS three times. Cells were detached by adding trypsin, neutralized by adding five volumes of serum-containing DMEM, centrifuged (1,600 rpm, 5 min), resuspended in PBS, and transferred to FACS tubes kept on ice until FACS analysis. For confocal imaging, LysoTracker Red (50 nM) was added after HA or G2 incubation, and the plate was incubated for another 1 h. The supernatant was removed, and the cells were washed three times with PBS buffer. The cells were fixed by adding 10% formalin (1 mL/well), and after 15 min, formalin was removed, and cells were washed with PBS buffer for three times. DAPI solution (300 nM, 300 µL/well) and 200 µL of PBS buffer were added to each well. After 4 min, they were removed, and cells were washed five times with PBS buffer. The cover glass was placed on a microscope slide, and images were obtained by Olympus FluoView 1000 LSM confocal microscope.

2.4.7 CD44 HABD cloning, expression and purification

CD44 HABD was cloned, expressed, and purified as previously described ²².

2.4.8 Immobilized CD44 HABD SPR assay

Molecular affinity for the CD44 HABD was assessed by monitoring binding to a surface with covalently immobilized CD44 HABD using SPR on a Biacore S200 (GE Healthcare) as

previously described ²². In short, a CM5 Biacore Sensor Chip surface was activated with 0.4 M 1-ethyl-3-(3-dimethylaminopropyl)carbodiimide hydrochloride and 0.1 M *N*-hydroxysuccinimide. CD44 HABD was dialyzed against 10 mM MES pH 4.4. It was then flowed over the surface and bound via amine coupling until saturation at 3500 Response Units (RU) was achieved. Remaining carboxymethyl groups were blocked with 1 M ethanolamine. To quantify binding of molecules of interest, HA polysaccharide (10 kDa) and HA-derivatives in a PBS buffer containing 0.005% Surfactant P-20 were passed over the chip surface in a two-fold dilution series (2500 µg/mL – 19.5 µg/mL) at 30 µL/min. Equilibrium response units were measured after 60 seconds. Initial dissociation periods were set for 60 seconds but increased to 180 seconds to attempt to return binding levels back to baseline when slow dissociation was observed.

2.4.9 Immobilized HA SPR assay

HMW-HA (CAS Number: 9067-32-7, sodium salt from rooster comb, Sigma-Aldrich) was biotinylated using hydrazide biotin as previously described ³², and immobilized onto a streptavidin SA Biacore Sensor Chip using the previously established method ²². In short, biotinylated-HA in HEPES-EP was passed over the chip surface until the response signal stabilized at 115 RU as monitored with the Biacore S200 (GE Healthcare). For the competition-based assay, a fixed concentration of CD44 HABD (~17 µM) was incubated with serial dilutions (2500 µg/mL – 19.5 µg/mL) of ligands (HA and HA-derivatives) solubilized in HEPES-EP and placed on a plate shaker for 10 minutes at room temperature prior to placing samples on the Biacore S200. Mixtures were injected over the chip surface at 30 µL/min for 1 minute followed by 2 minutes of a dissociation phase using HEPES-EP buffer. RU values taken 5 seconds prior to the end of the equilibrium phase were plotted against concentration to calculate IC₅₀ values. Data was fitted using a nonlinear regression with log[inhibitor] vs. response using GraphPad Prism. Issues surrounding non-specific

binding, binding to reference chip surface, and fluidics problems of the polymeric molecules complicated the analysis.

2.4.10 Immobilized HA SPR assay with ligand only binding subtraction

A reference subtraction experiment was completed to decrease the interference due to fluidic problems and non-specific interactions associated with the polymeric nature of HA and HA-derivatives. Ligand only was passed over the chip surface using the same two-fold dilution series maintaining the same buffer and experimental conditions. The resulting sensorgram was subtracted from the sensorgram of CD44 preincubated with ligand. A graphical representation of the reference subtraction is shown in **Figure 2.13, 2.14 and 2.15**.

2.4.11 Machine learning modeling of library data

Library data as shown in **Figure 2.2** was converted into tabular format (**Table 2.1**). Categorical data, such as the types of amines, was converted into numerical data using one-hot encoding. Each entry is converted to a vector of size 14. The dataset was randomly shuffled using Sci-learn library for training set and test set, with 70 % of the data to training set. Each vector was divided into feature vector (size = 13) and label vector (size = 1). Linear regression was carried out using Sci-learn. Training set, test set, and code script from Google Colab were included in the supplementary materials. Mean absolute error (MAE) was calculated using sklearn metrics library.

APPENDIX

APPENDIX

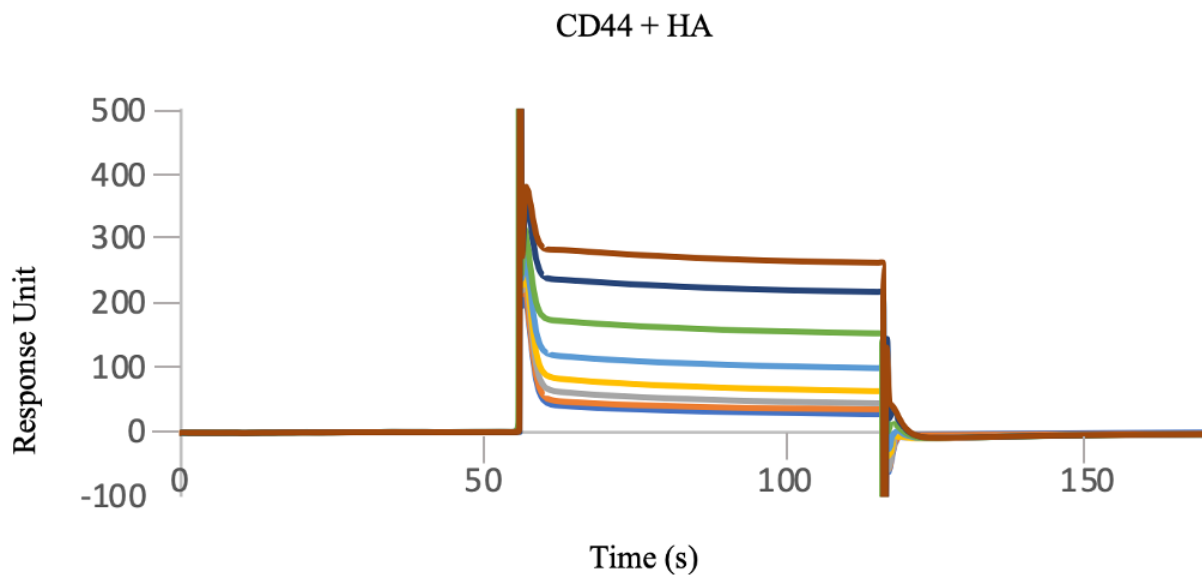


Figure 2.13 Sensograms of CD44 incubated with HA (10 kDa) at the following concentration range (from bottom to top): 2500 $\mu\text{g/mL}$, 1250 $\mu\text{g/mL}$, 625 $\mu\text{g/mL}$, 312 $\mu\text{g/mL}$, 156 $\mu\text{g/mL}$, 78 $\mu\text{g/mL}$, 39 $\mu\text{g/mL}$ and 19 $\mu\text{g/mL}$.

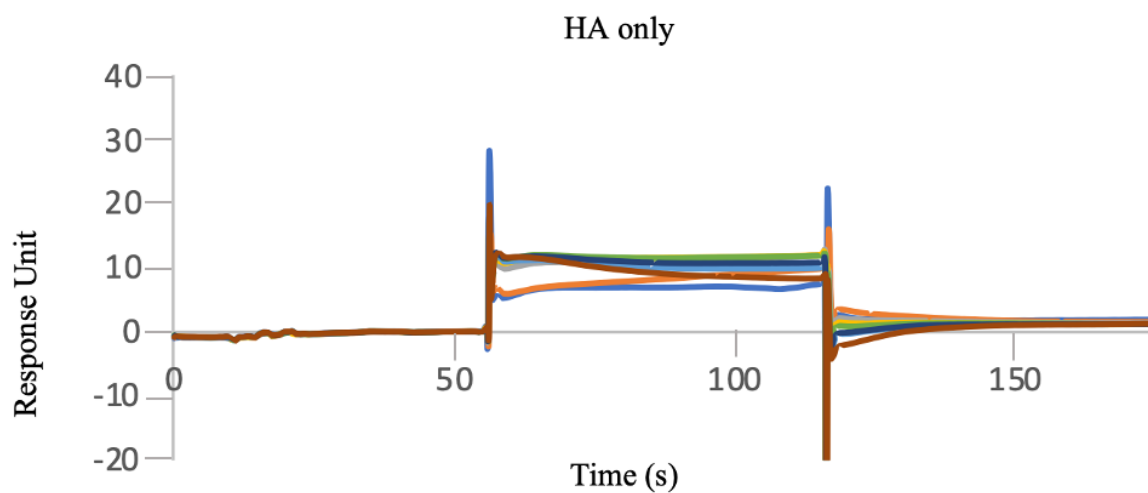


Figure 2.14 Sensograms of HA (10 kDa) only at the following concentration range: 2500 $\mu\text{g/mL}$, 1250 $\mu\text{g/mL}$, 625 $\mu\text{g/mL}$, 312 $\mu\text{g/mL}$, 156 $\mu\text{g/mL}$, 78 $\mu\text{g/mL}$, 39 $\mu\text{g/mL}$ and 19 $\mu\text{g/mL}$.

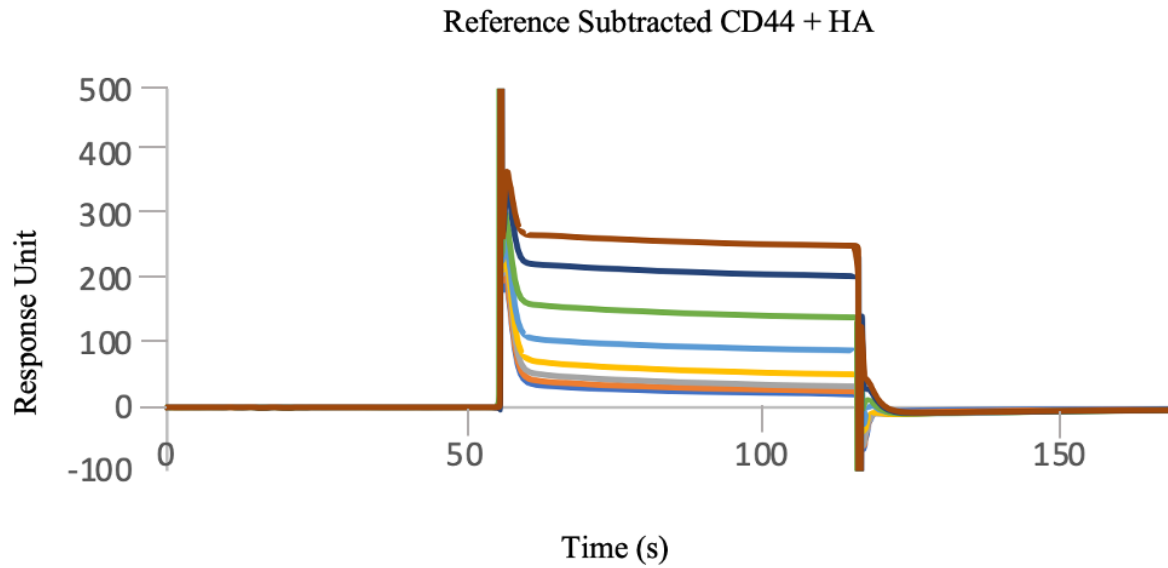


Figure 2.15 Sensograms of reference subtraction (as indicated by Figure 6 in main text) at the following concentration range (from bottom to top): 2500 $\mu\text{g/mL}$, 1250 $\mu\text{g/mL}$, 625 $\mu\text{g/mL}$, 312 $\mu\text{g/mL}$, 156 $\mu\text{g/mL}$, 78 $\mu\text{g/mL}$, 39 $\mu\text{g/mL}$ and 19 $\mu\text{g/mL}$.

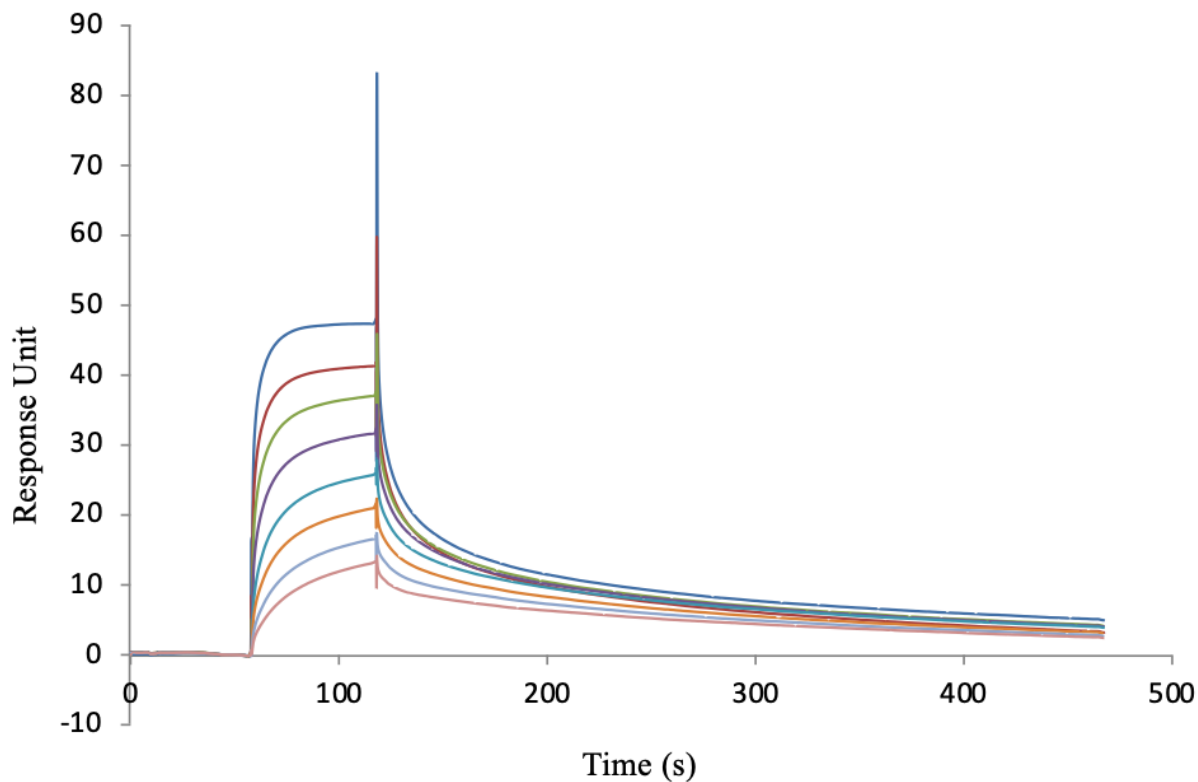


Figure 2.16 Sensograms of HA (10 kDa) in the immobilized CD44 SPR assay. Sensograms showed a non-plateau during the equilibrium phase and slow dissociation phase that never reached the baseline, at wide concentration range (from top to bottom): 2500 $\mu\text{g/mL}$, 1250 $\mu\text{g/mL}$, 625 $\mu\text{g/mL}$, 312 $\mu\text{g/mL}$, 156 $\mu\text{g/mL}$, 78 $\mu\text{g/mL}$, 39 $\mu\text{g/mL}$ and 19 $\mu\text{g/mL}$. This implies the non-specific interaction and avidity issue of the polymeric-HA.

05-11-4_PROTON_01

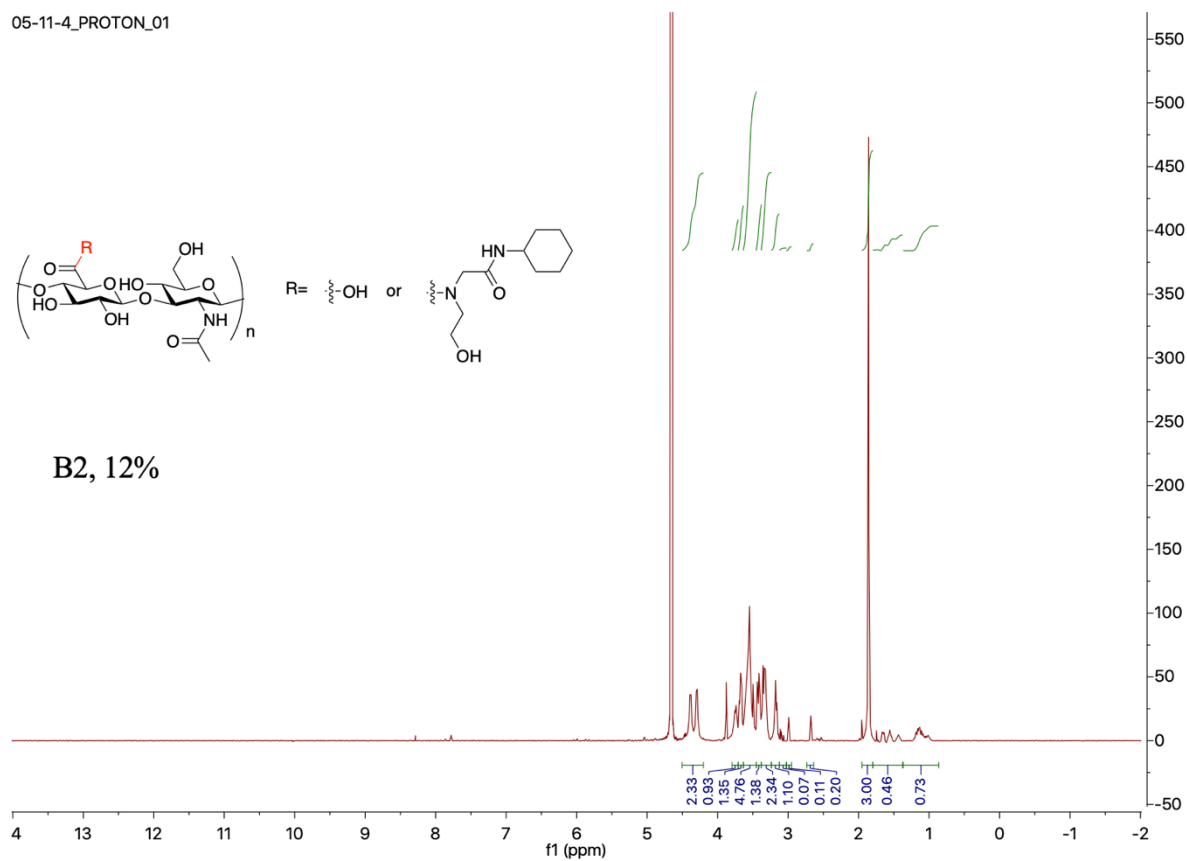


Figure 2.17 ^1H -NMR spectrum of compound B2 at 12% loading, 10 kDa.

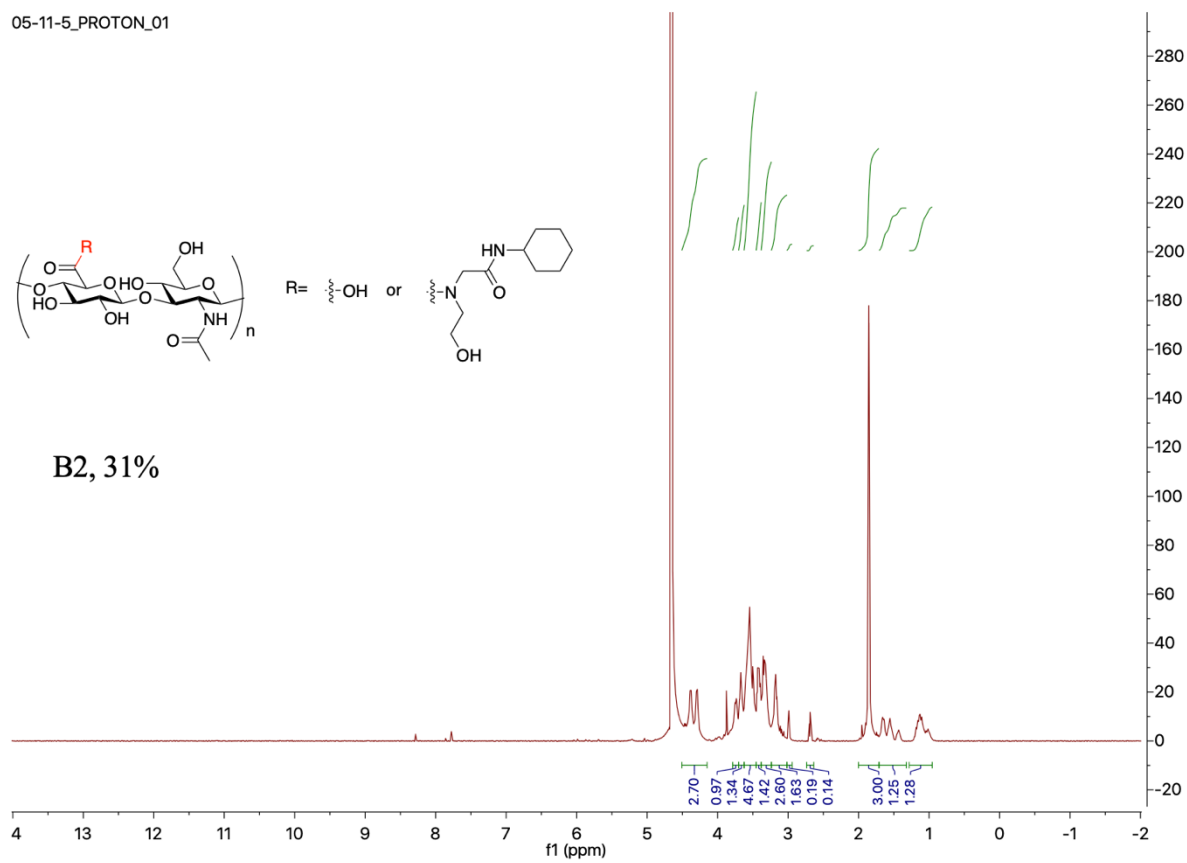


Figure 2.18 ^1H -NMR spectrum of compound B2 at 31% loading, 10 kDa.

05-11-7_PROTON_01

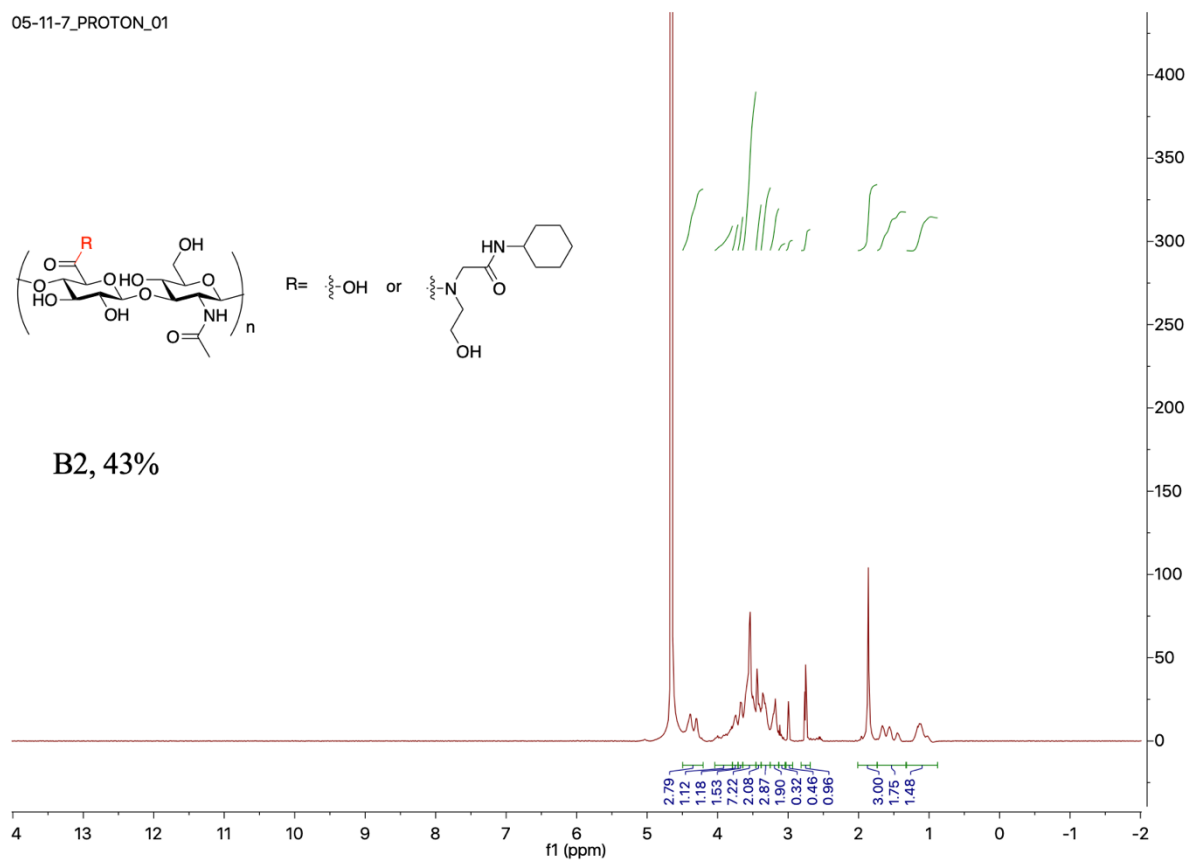


Figure 2.19 ^1H -NMR spectrum of compound B2 at 43% loading, 10 kDa.

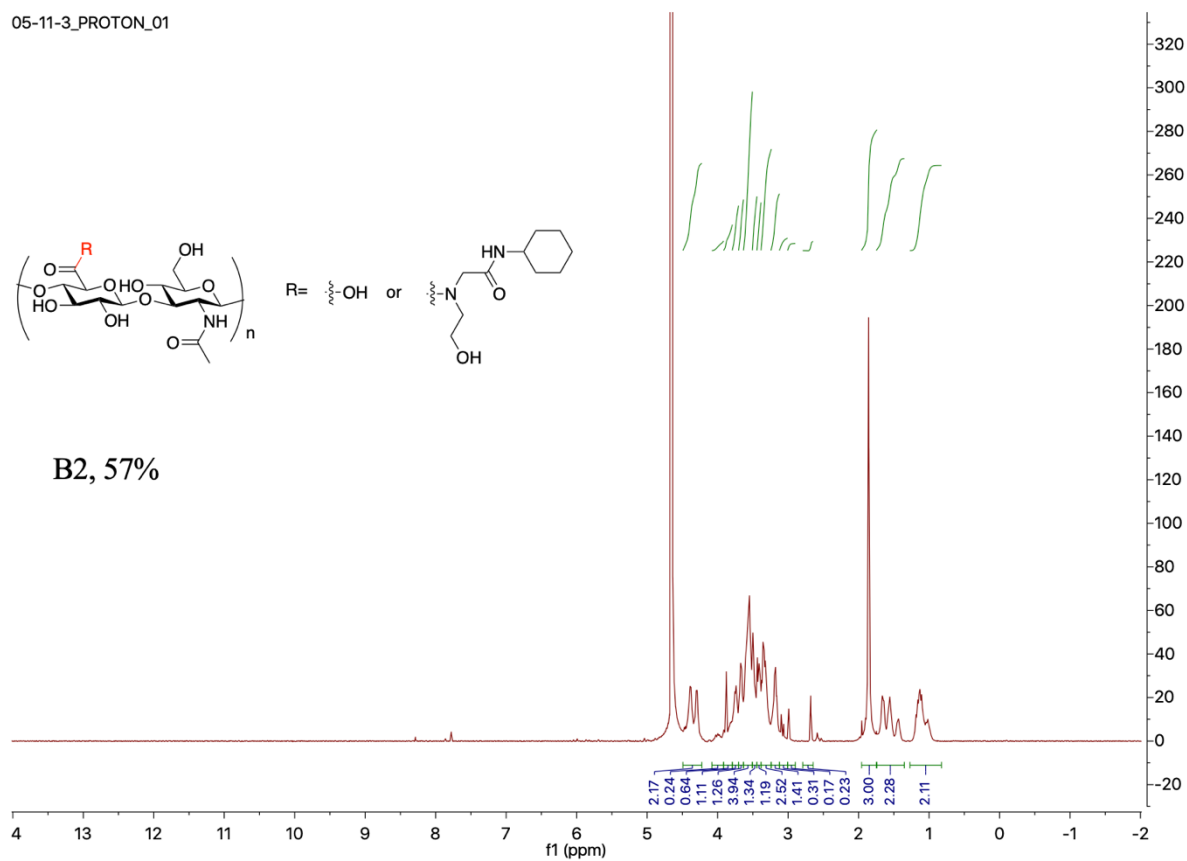


Figure 2.20 ^1H -NMR spectrum of compound B2 at 57 % loading, 10 kDa.

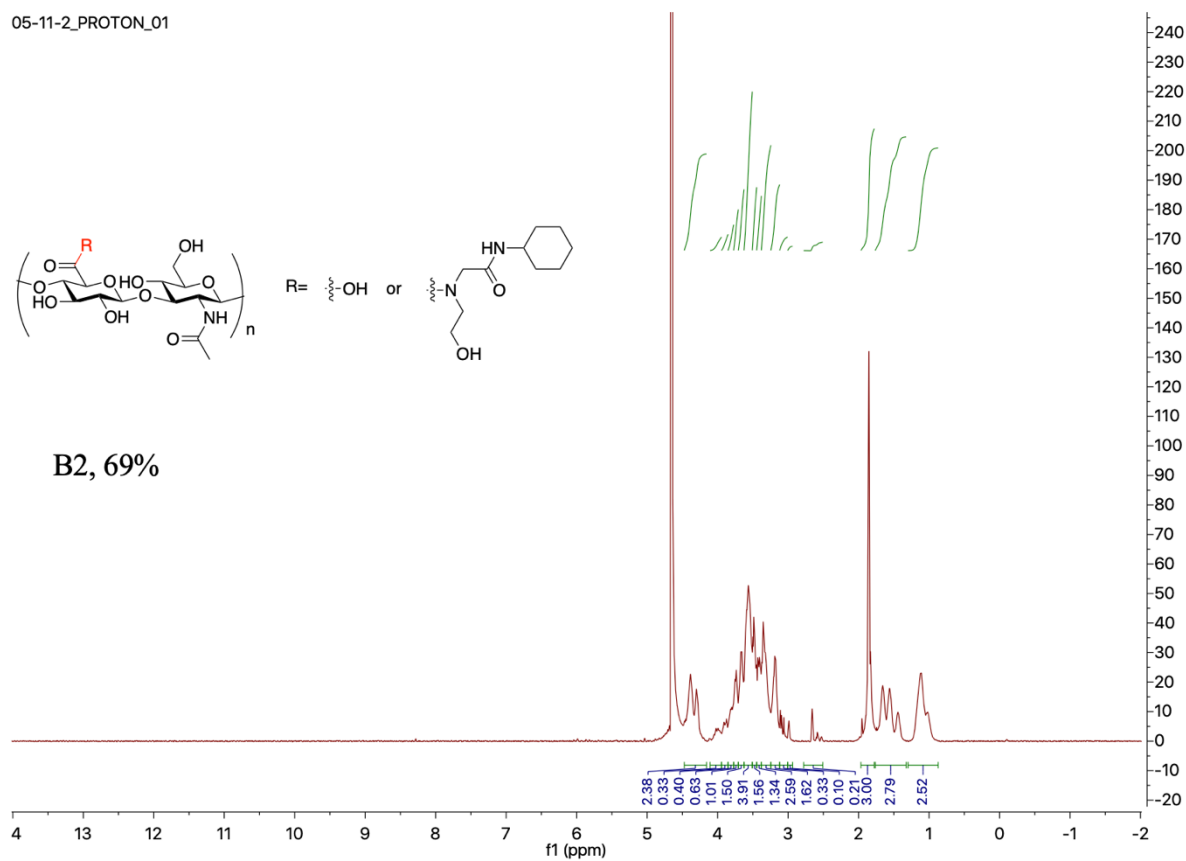


Figure 2.21 ^1H -NMR spectrum of compound B2 at 69% loading, 10 kDa.

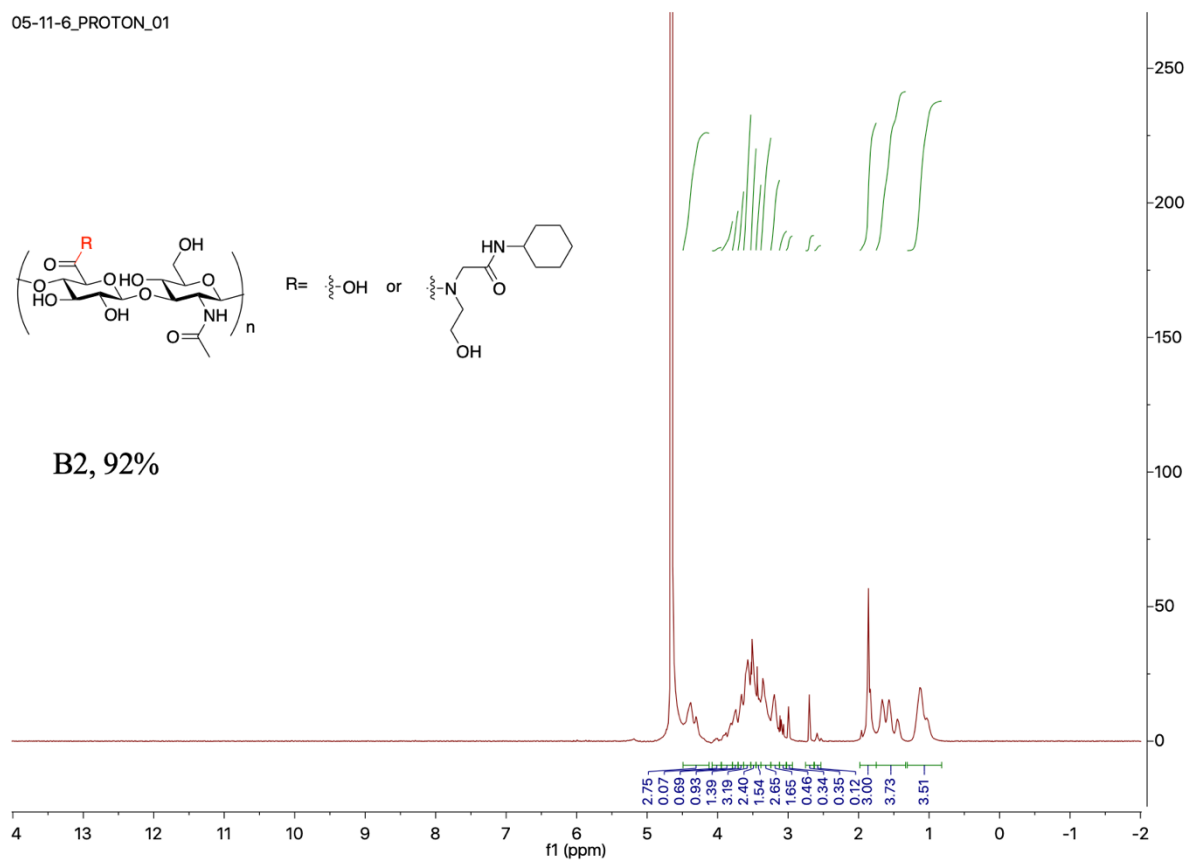


Figure 2.22 ^1H -NMR spectrum of compound B2 at 92% loading, 10 kDa.

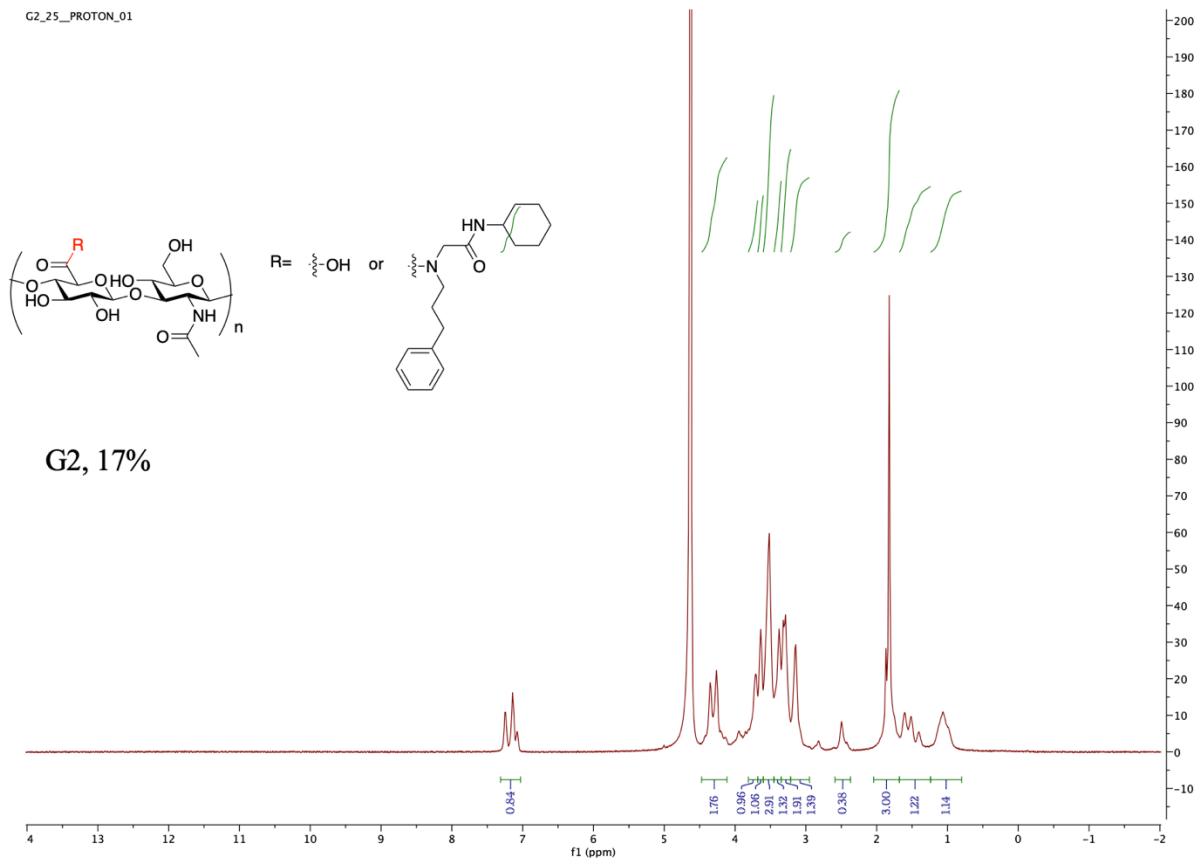


Figure 2.23 ^1H -NMR spectrum of compound G2 at 17% loading, 10 kDa.

G2_50_PROTON_01

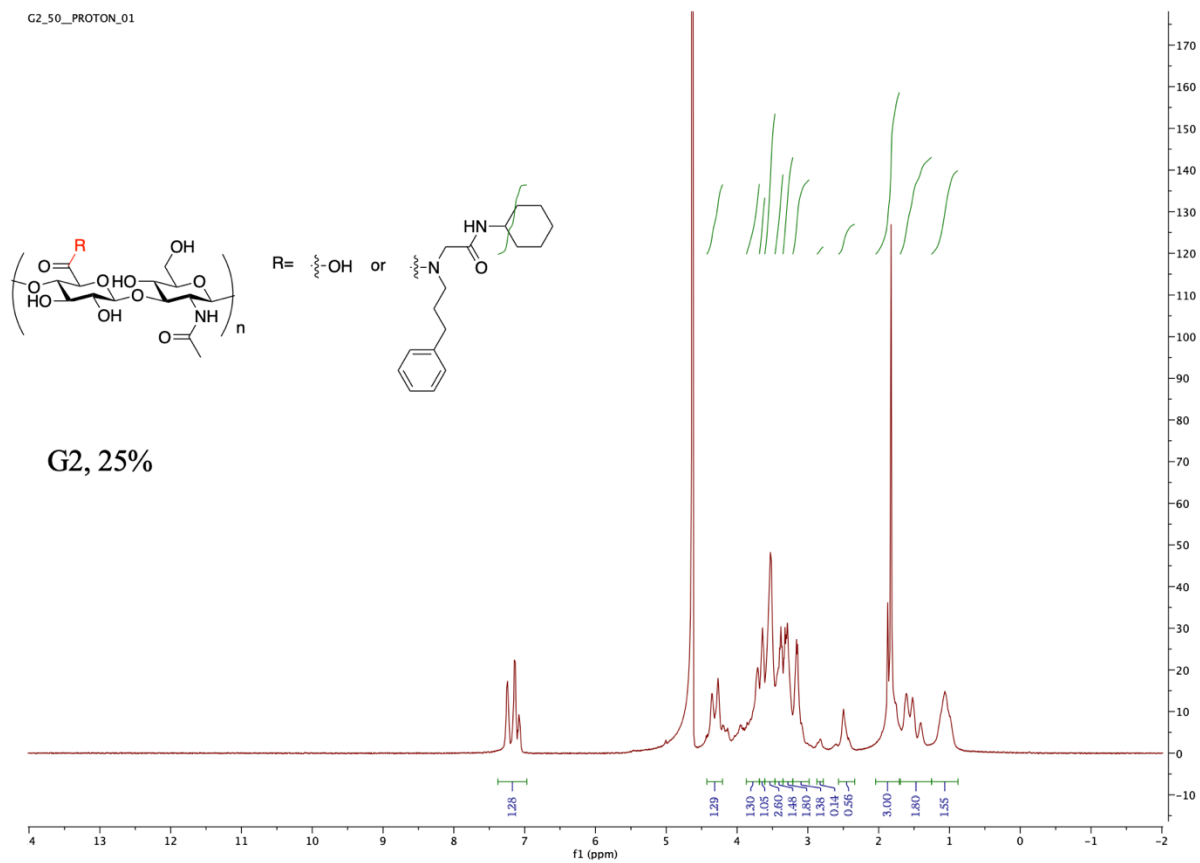
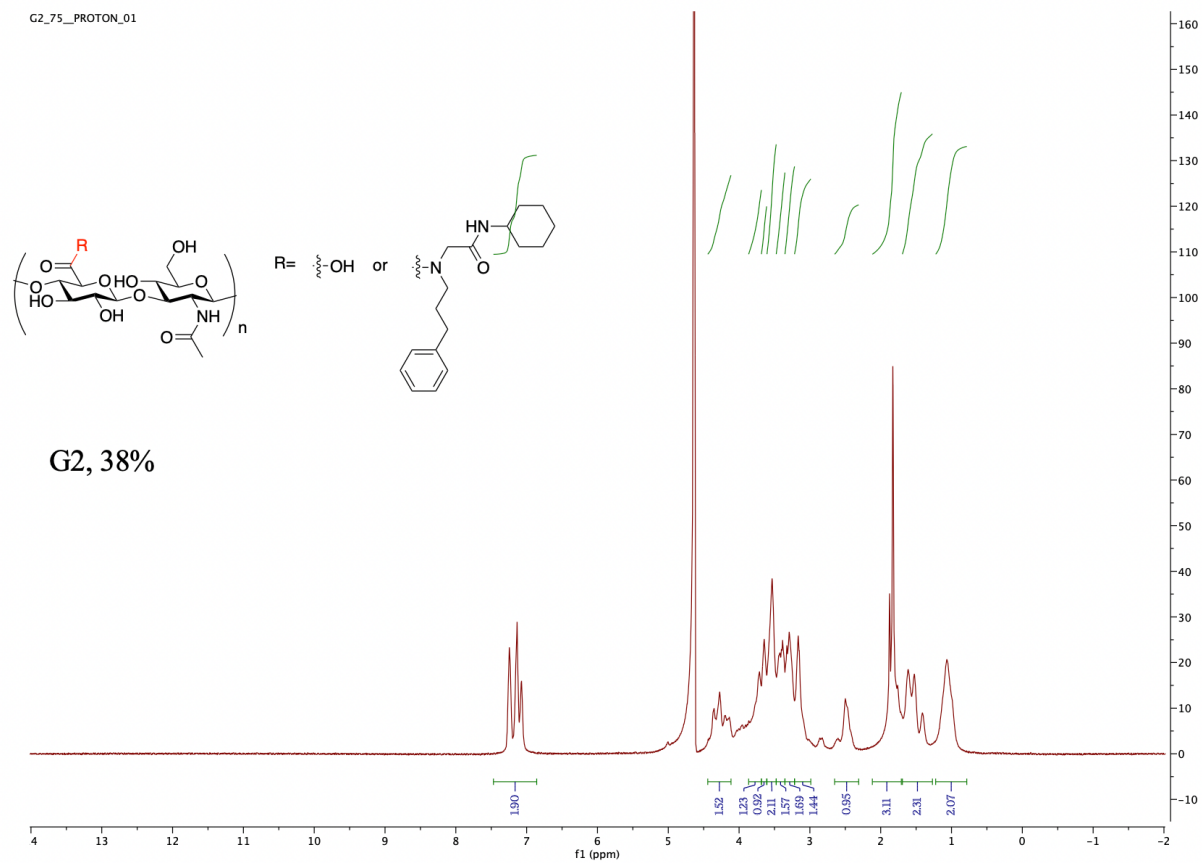


Figure 2.24 ¹H -NMR spectrum of compound G2 at 25% loading, 10 kDa.

G2_75_PROTON_01



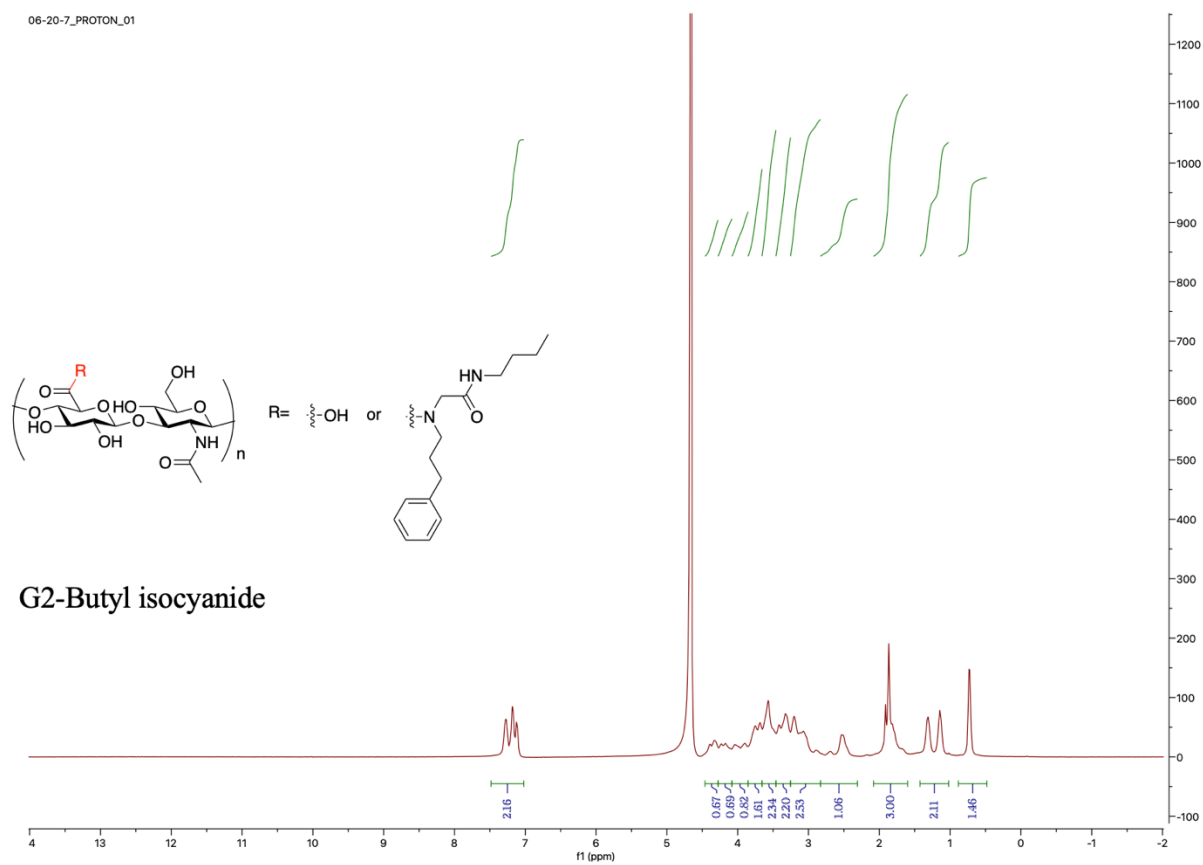


Figure 2.26 ¹H -NMR spectrum of compound G2-butyl isocyanide, 10 kDa.

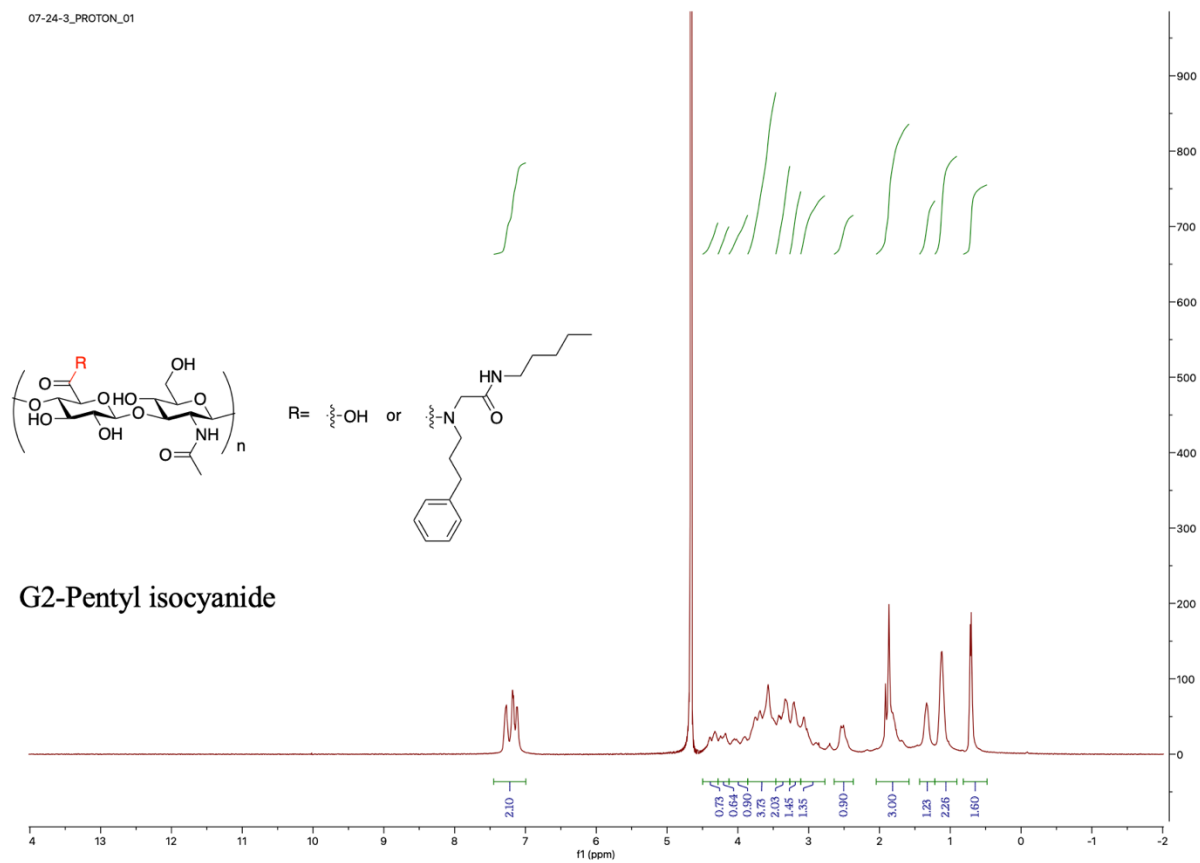


Figure 2.27 ^1H -NMR spectrum of compound G2-pentyl isocyanide, 10 kDa.

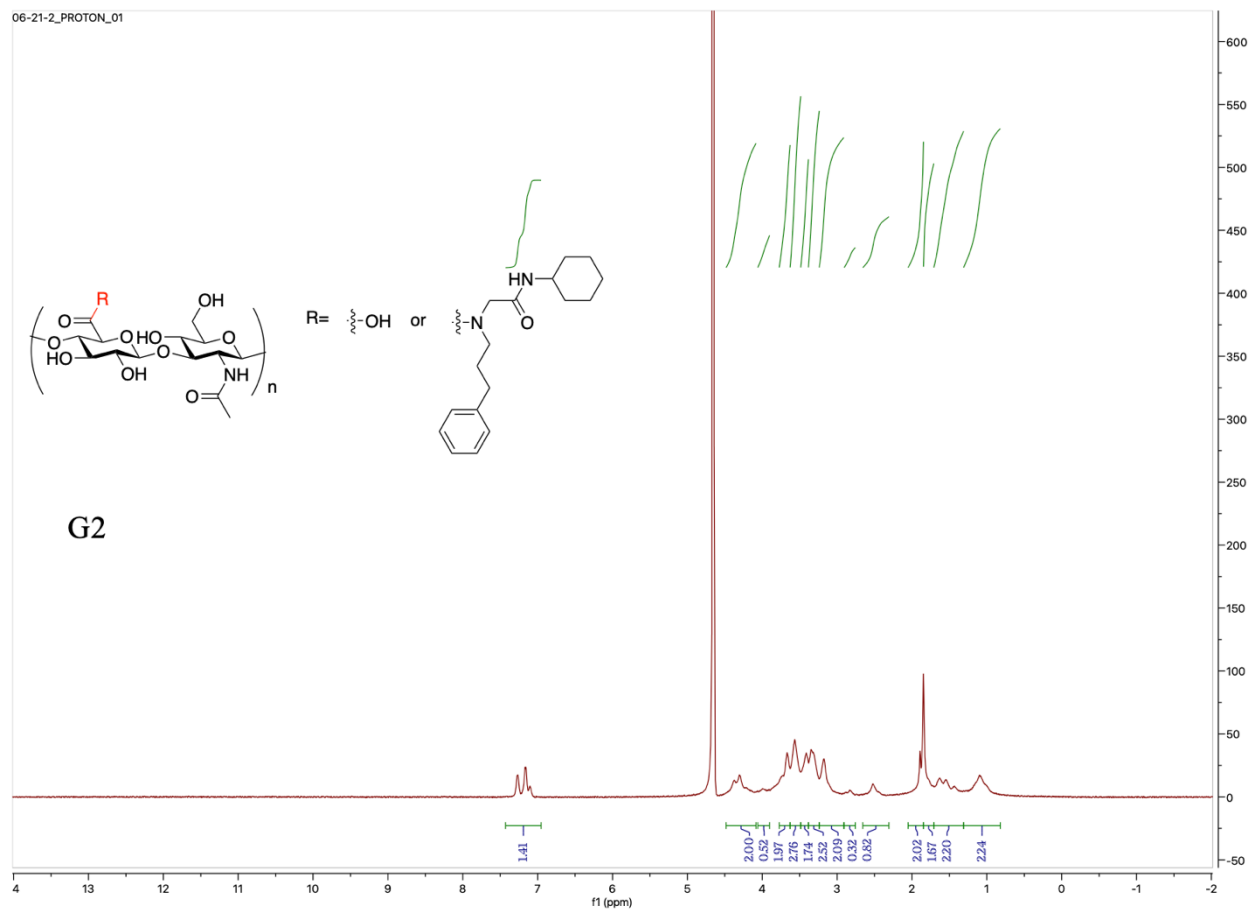


Figure 2.28 ¹H -NMR spectrum of compound G2, 60 kDa.

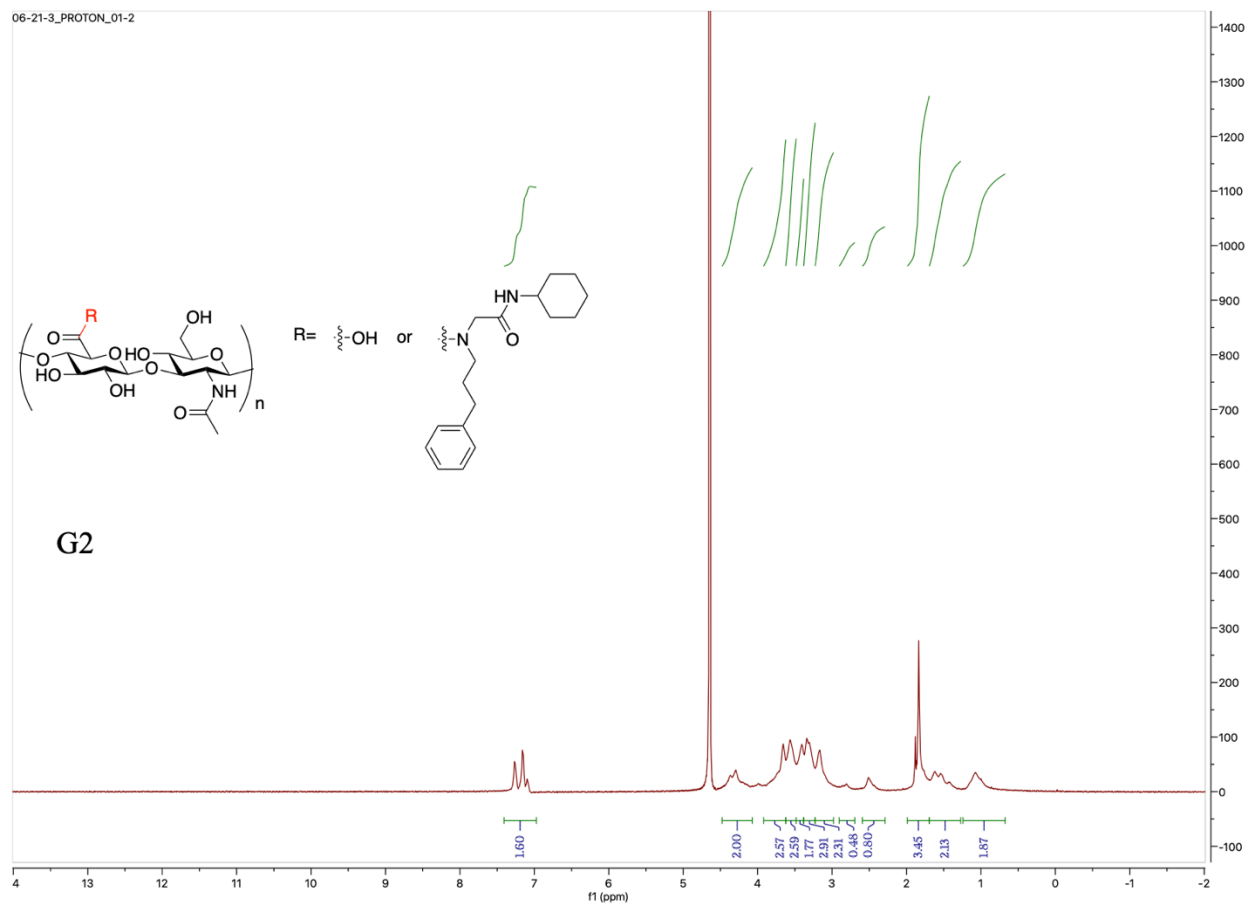


Figure 2.29 ¹H -NMR spectrum of compound G2, 100 kDa.

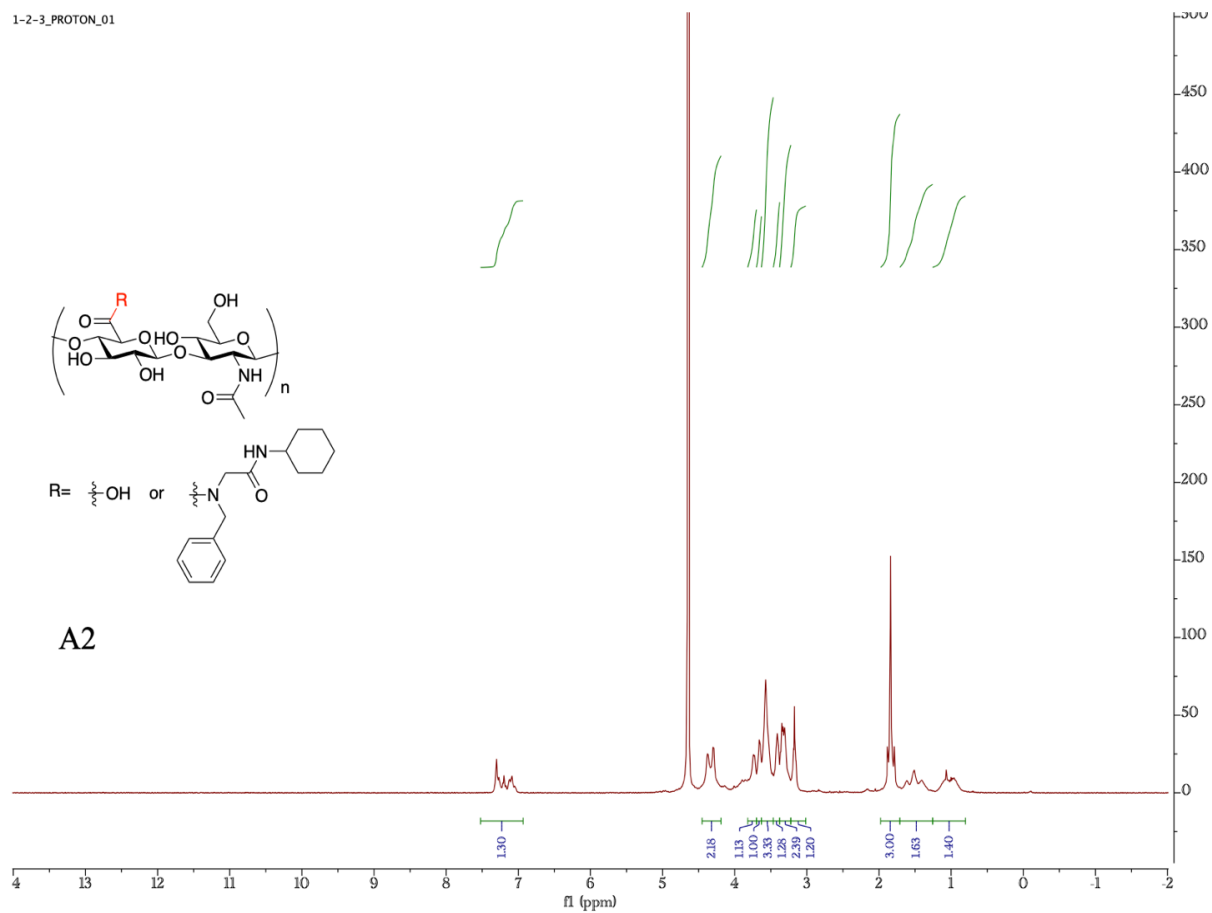


Figure 2.30 ^1H -NMR spectrum of compound A2, 10 kDa.

1-2-4_PROTON_01

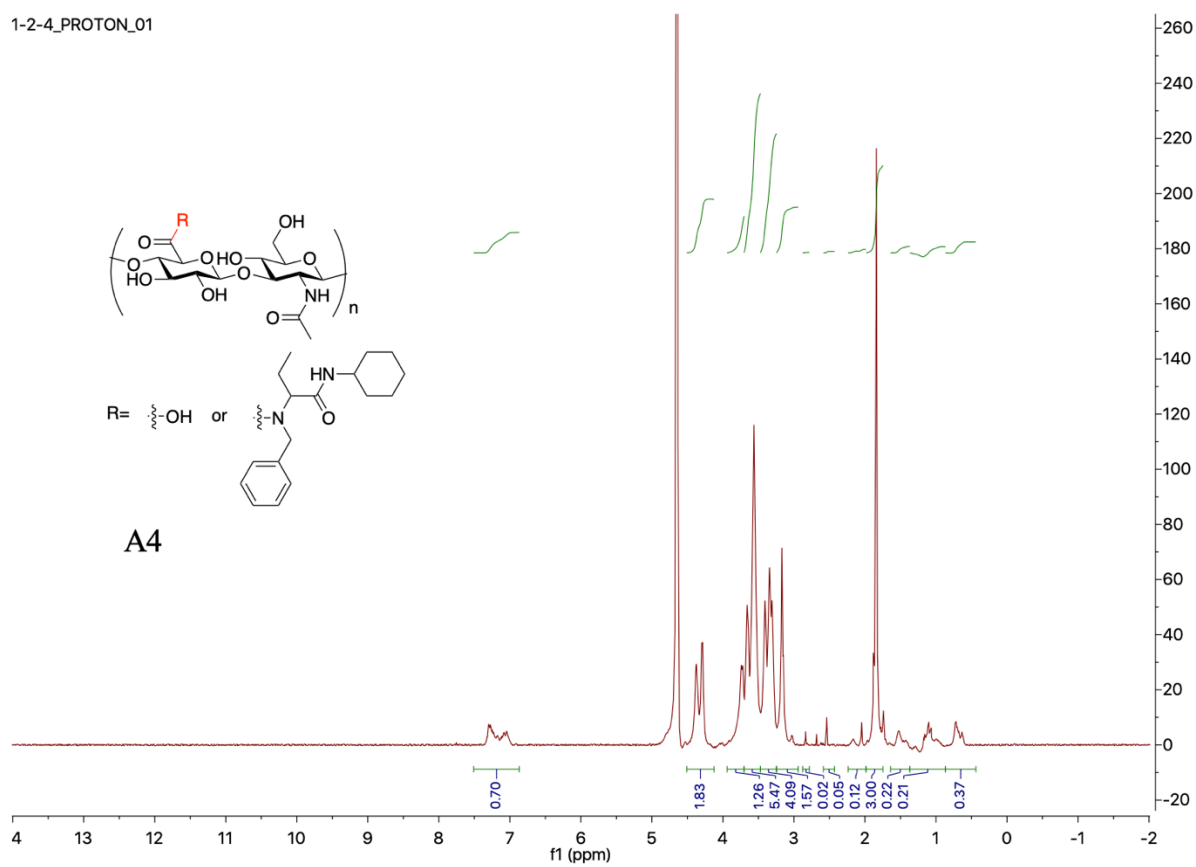


Figure 2.31 ¹H -NMR spectrum of compound A4, 10 kDa.

06-04-3_PROTON_01

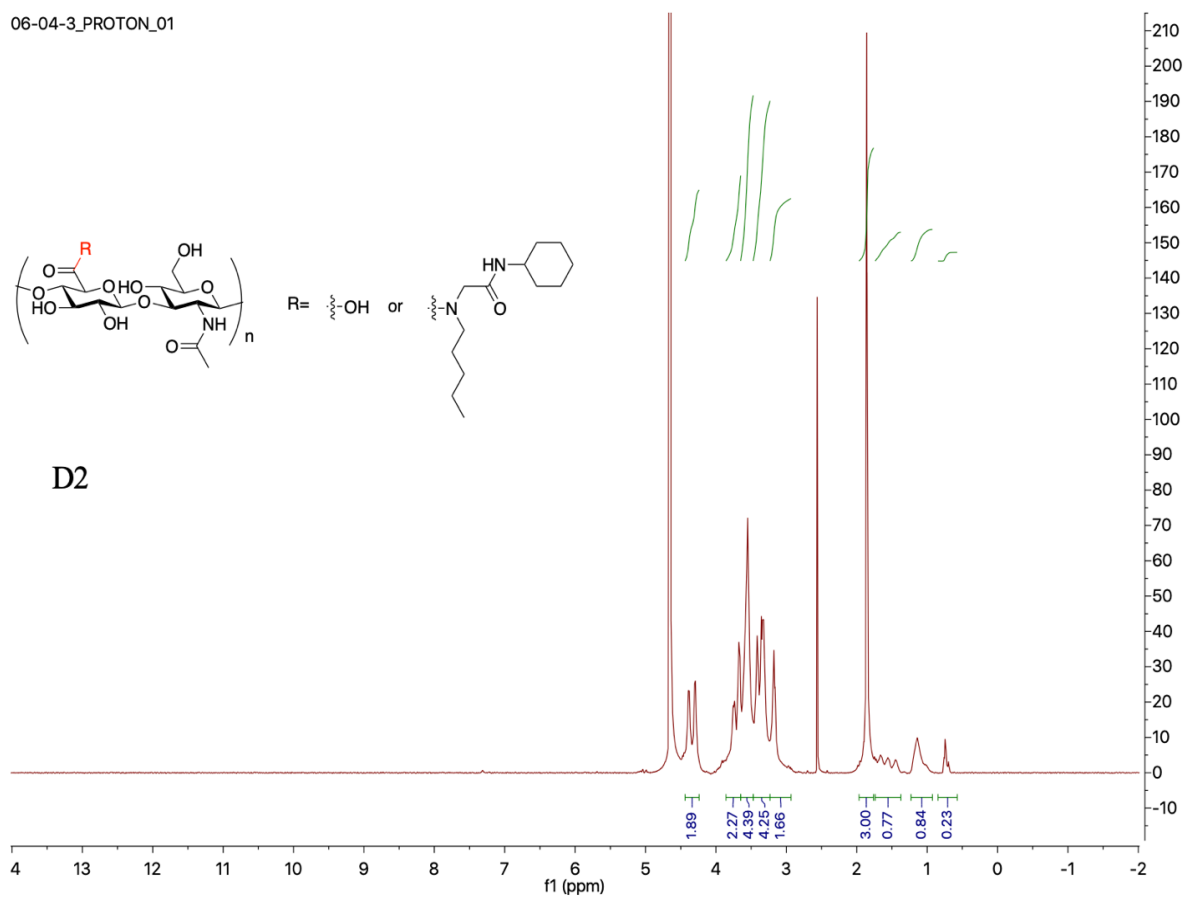


Figure 2.32 ^1H -NMR spectrum of compound D2, 10 kDa.

12-12-7_PROTON_01

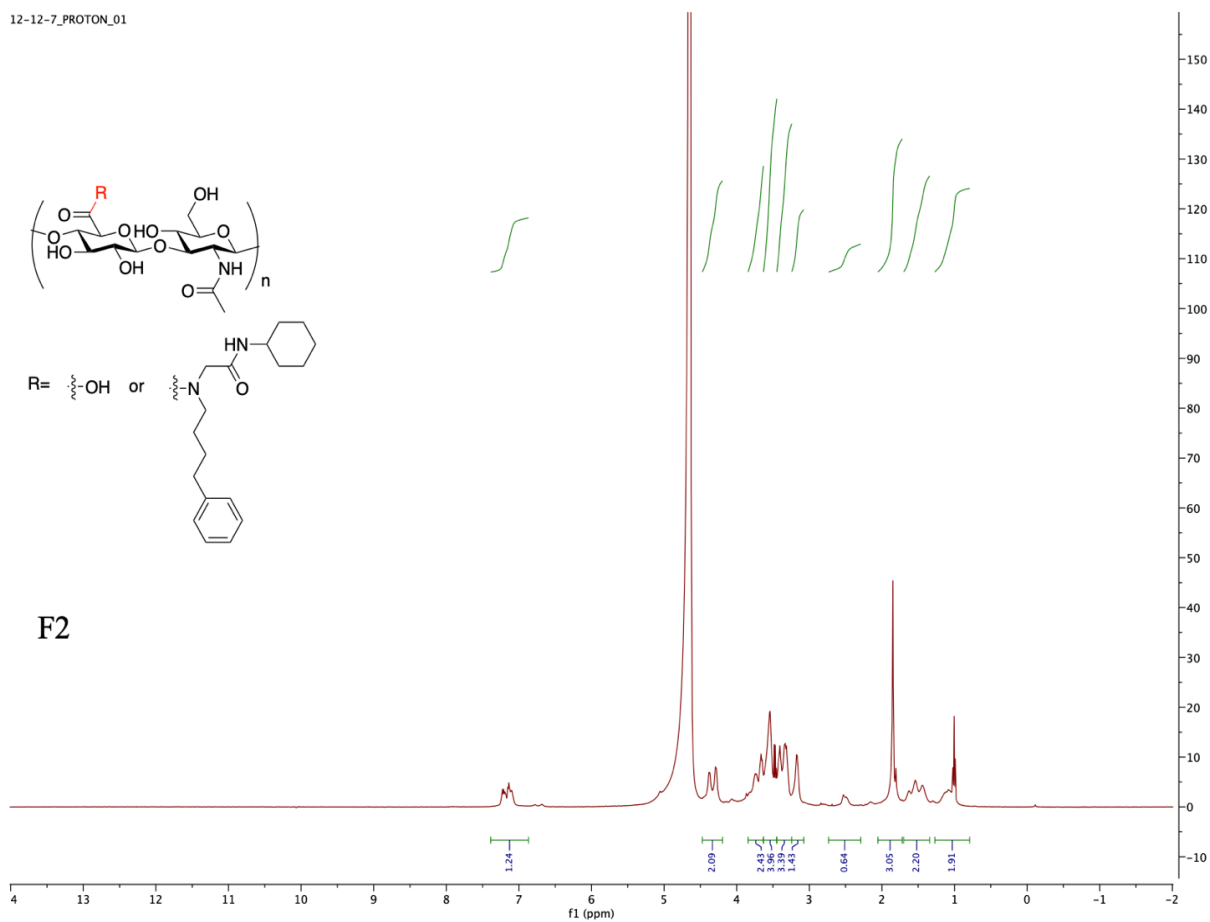
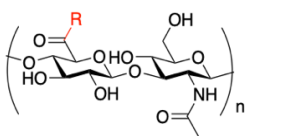
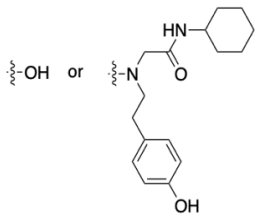
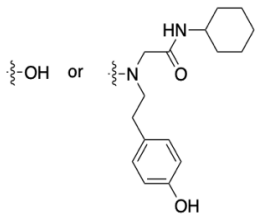


Figure 2.33 ^1H -NMR spectrum of compound F2, 10 kDa.

1-2-2_PROTON_01



R =  or 

I2

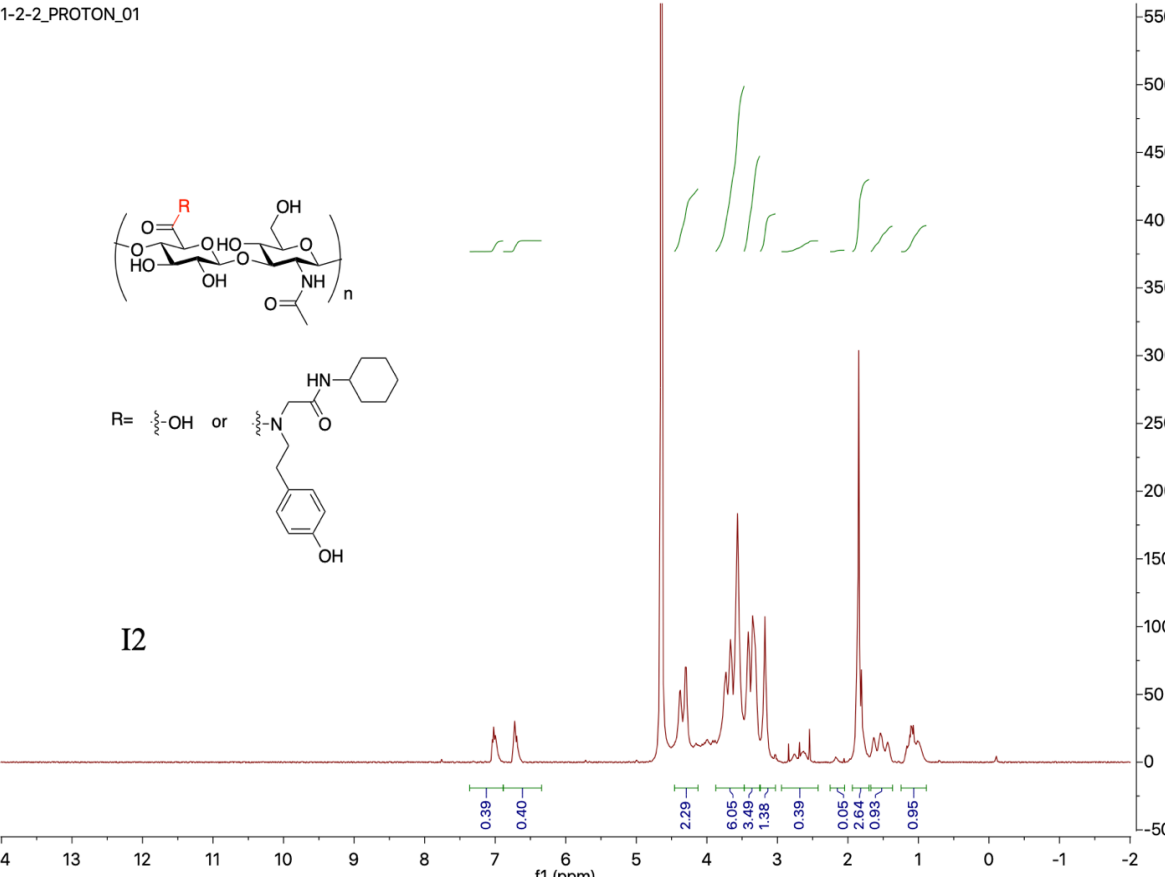


Figure 2.34 ^1H -NMR spectrum of compound I2, 10 kDa.

Amine	Aldehyde	Inhibition % change
Benzylamine	Heptafluorobutyraldehyde	-13
Benzylamine	Formaldehyde	-14
Benzylamine	Iso valeraldehyde	-10
Benzylamine	Propionaldehyde	-13
Ethanolamine	Heptafluorobutyraldehyde	-9
Ethanolamine	Formaldehyde	3
Ethanolamine	Iso valeraldehyde	-14
Ethanolamine	Propionaldehyde	-11
3-Amino-1-propanol	Heptafluorobutyraldehyde	-6
3-Amino-1-propanol	Formaldehyde	2
3-Amino-1-propanol	Iso valeraldehyde	-23
3-Amino-1-propanol	Propionaldehyde	-18
Amylamine	Heptafluorobutyraldehyde	0
Amylamine	Formaldehyde	11
Amylamine	Iso valeraldehyde	-17
Amylamine	Propionaldehyde	-15
Cycloheptylamine	Heptafluorobutyraldehyde	-7
Cycloheptylamine	Formaldehyde	-26
Cycloheptylamine	Iso valeraldehyde	-23
Cycloheptylamine	Propionaldehyde	-10
4-Phenylbutylamine	Heptafluorobutyraldehyde	1
4-Phenylbutylamine	Formaldehyde	38
4-Phenylbutylamine	Iso valeraldehyde	-6
4-Phenylbutylamine	Propionaldehyde	-8
Tryptamine	Heptafluorobutyraldehyde	-1
Tryptamine	Formaldehyde	22
Tryptamine	Iso valeraldehyde	4

Table 2.2 Tabular format of library data of 36 entries in total.

Table 2.2 (cont'd)

Tryptamine	Propionaldehyde	-8
Tyramine	Heptafluorobutyraldehyde	3
Tyramine	Formaldehyde	23
Tyramine	Iso valeraldehyde	-22
Tyramine	Propionaldehyde	-25

inh ibi tio n inc rea se	3- A mi no -1- pr op an ol	3- Phe nyl- 1- pro pyl ami ne	4- Phen ylbut ylami ne	Am yla min e	Ben zyla min e	Cyclo hepty lamin e	Etha nola min e	Try pta mi ne	Ty ra mi ne	For mal deh yde	Heptafl uorobut yraldeh yde	Iso vale rald ehy de	Propi onald ehyd e
- 13	0	0	0	0	1	0	0	0	0	0	1	0	0
- 14	0	0	0	0	1	0	0	0	0	1	0	0	0
- 10	0	0	0	0	1	0	0	0	0	0	0	1	0
-9	0	0	0	0	0	0	1	0	0	0	1	0	0
-6	1	0	0	0	0	0	0	0	0	0	1	0	0
2	1	0	0	0	0	0	0	0	0	1	0	0	0
- 23	1	0	0	0	0	0	0	0	0	0	0	1	0
- 17	0	0	0	1	0	0	0	0	0	0	0	1	0
- 15	0	0	0	1	0	0	0	0	0	0	0	0	1
-7	0	0	0	0	0	1	0	0	0	0	1	0	0
- 26	0	0	0	0	0	1	0	0	0	1	0	0	0

Table 2.3 Training set with 25 entries. Each entry was represented as a vector using one-hot encoding.

Table 2.3 (cont'd)

inh ibi tio n inc rea se	3- A mi no -1- pr op an ol	3- Phe nyl- 1- pro pyl ami ne	4- Phen ylbut ylami ne	Am yla min e	Ben zyla min e	Cyclo hepty lamin e	Etha nola min e	Try pta mi ne	Ty ra mi ne	For mal deh yde	Heptafl uorobut yraldeh yde	Iso vale rald ehy de	Propi onald ehyd e
- 10	0	0	0	0	0	1	0	0	0	0	0	0	1
1	0	0	1	0	0	0	0	0	0	0	1	0	0
38	0	0	1	0	0	0	0	0	0	1	0	0	0
-6	0	0	1	0	0	0	0	0	0	0	0	1	0
-8	0	0	1	0	0	0	0	0	0	0	0	0	1
38	0	1	0	0	0	0	0	0	0	1	0	0	0
-5	0	1	0	0	0	0	0	0	0	0	0	0	1
-1	0	0	0	0	0	0	0	1	0	0	1	0	0
4	0	0	0	0	0	0	0	1	0	0	0	1	0
-8	0	0	0	0	0	0	0	1	0	0	0	0	1
3	0	0	0	0	0	0	0	0	1	0	1	0	0
23	0	0	0	0	0	0	0	0	1	1	0	0	0
- 22	0	0	0	0	0	0	0	0	1	0	0	1	0
- 25	0	0	0	0	0	0	0	0	1	0	0	0	1
-6	0	1	0	0	0	0	0	0	0	0	1	0	0
1	0	0	1	0	0	0	0	0	0	0	1	0	0

inh ibi tio n inc rea se	3- A mi no -1- pr op an ol	3- Phe nyl- 1- pro pyl ami ne	4- Phen ylbut ylami ne	Am yla min e	Ben zyla min e	Cyclo hepty lamin e	Etha nola min e	Try pta mi ne	Ty ra mi ne	For mal deh yde	Heptafl uorobut yraldeh yde	Iso vale rald ehy de	Propi onald ehyd e
- 11	0	0	0	0	0	0	1	0	0	0	0	0	1
3	0	0	0	0	0	0	1	0	0	1	0	0	0
- 13	0	0	0	0	1	0	0	0	0	0	0	0	1
0	0	0	0	1	0	0	0	0	0	0	1	0	0
- 14	0	0	0	0	0	0	1	0	0	0	0	1	0
- 23	0	0	0	0	0	1	0	0	0	0	0	1	0
11	0	0	0	1	0	0	0	0	0	1	0	0	0
38	0	1	0	0	0	0	0	0	0	1	0	0	0
22	0	0	0	0	0	0	0	1	0	1	0	0	0
- 18	1	0	0	0	0	0	0	0	0	0	0	0	1
4	0	1	0	0	0	0	0	0	0	0	0	1	0

Table 2.4 Test set with 11 entries. Each entry was represented as a vector using one-hot encoding.

```

import pandas as pd
# read table format of library data using Pandas
init_df = pd.read_csv('/content/ELISA library.csv')
# one-hot encoding of categorical data into numerical data
init_df.amine = init_df.amine.astype('category')
init_df.aldehyde = init_df.aldehyde.astype('category')
init_df = pd.get_dummies(init_df)
# split into label and feature
label = init_df['inhibition increase']
features = init_df[init_df.columns.difference(['inhibition increase'])]
# split into training set and test set
from sklearn.model_selection import train_test_split
x_train, x_test, y_train, y_test = train_test_split(features, label, test_size = 0.3)
## use training set and test set from previous run
# train_df = pd.read_csv('/content/train.csv')
# test_df = pd.read_csv('/content/test.csv')

# y_train = train_df['inhibition increase']
# x_train = train_df[init_df.columns.difference(['inhibition increase'])]

# y_test = test_df['inhibition increase']
# x_test = test_df[init_df.columns.difference(['inhibition increase'])]

from sklearn.linear_model import LinearRegression
# Linear regression with sklearn package
regression = LinearRegression()
regression.fit(x_train, y_train)

# calculate predicted value for test set
y_pred = regression.predict(x_test)

# calculate MAE by comparing y_test and y_pred
from sklearn.metrics import mean_absolute_error
mae_test = mean_absolute_error(y_test, y_pred)

```

Table 2.5 Code script from Google Colab for machine learning.

REFERENCES

REFERENCES

1. Day, A. J.; Prestwich, G. D., Hyaluronan-binding proteins: tying up the giant. *J. Biol. Chem.* **2002**, *277*, 4585-4588.
2. Lesley, J., Hyaluronan binding by cell surface CD44. *J. Biol. Chem.* **2000**, *275*, 26967–26975.
3. Ponta, H.; Sherman, L.; Herrlich, P. A., CD44: from adhesion molecules to signalling regulators. *Nat. Rev. Mol. Cell Biol.* **2003**, *4*, 33-45.
4. Toole, B. P.; Wight, T. N.; Tammi, M. I., Hyaluronan-cell interactions in cancer and vascular disease. *J. Biol. Chem.* **2002**, *277*, 4593-4596.
5. Aruffo, A.; Stamenkovic, I.; Melnick, M.; Underhill, C. B.; Seed, B., CD44 is the principal cell surface receptor for hyaluronate. *Cell* **1990**, *61*, 1303-1313.
6. Li, M.; Sun, J.; Zhang, W.; Zhao, Y.; Zhang, S.; Zhang, S., Drug delivery systems based on CD44-targeted glycosaminoglycans for cancer therapy. *Carbohydr. Polym.* **2021**, *251*, 117103.
7. Liu, K.; Huang, X., Synthesis of self-assembled hyaluronan based nanoparticles and their applications in targeted imaging and therapy. *Carbohydr. Res.* **2022**, *511*, 108500.
8. Misra, S.; Heldin, P.; Hascall, V. C.; Karamano, N. K.; Skandalis, S. S.; Markwald, R. R.; Ghatak, S., Hyaluronan–CD44 interactions as potential targets for cancer therapy. *FASEB J.* **2011**, *278*, 1429-.
9. Nasr, S. H.; Tonson, A.; El-Dakdouki, M. H.; Zhu, D. C.; Agnew, D.; Wiseman, R.; Qian, C.; Huang, X., Effects of nanoprobe morphology on cellular binding and inflammatory responses: hyaluronan-conjugated magnetic nanoworms for magnetic resonance imaging of atherosclerotic plaques. *ACS Appl. Mater. Interfaces* **2018**, *10*, 11495-11507.
10. Nasr, S. H.; Rashidijahanabad, Z.; Ramadan, S.; Kauffman, N.; Parameswaran, N.; Zinn, K. R.; Qian, C.; Arora, R.; Agnew, D.; Huang, X., Effective atherosclerotic plaque inflammation inhibition with targeted drug delivery by hyaluronan conjugated atorvastatin nanoparticles. *Nanoscale* **2020**, *12*, 9541-9556.
11. Zhang, W.; Cai, J.; Wu, B.; Shen, Z., pH-responsive hyaluronic acid nanoparticles coloaded with sorafenib and cisplatin for treatment of hepatocellular carcinoma. *J. Biomater. Appl.* **2019**, *34*, 219-228.
12. Lee, H.; Lee, K.; Park, T. G., Hyaluronic acid–paclitaxel conjugate micelles: Synthesis, characterization, and antitumor activity. *Bioconjug. Chem.* **2008**, *19*, 1319-1325.
13. Vyas, D.; Lopez-Hisijos, N.; Gandhi, S.; El-Dakdouki, M.; Basson, M. D.; Walsh, M. F.; Huang, X.; Vyas, A. K.; Chaturvedi, L. S., Doxorubicin-Hyaluronan Conjugated Super-Paramagnetic Iron Oxide Nanoparticles (DOX-HA-SPION) Enhanced Cytoplasmic Uptake of

Doxorubicin and Modulated Apoptosis, IL-6 Release and NF-kappaB Activity in Human MDA-MB-231 Breast Cancer Cells. *J. Nanosci. Nanotechnol.* **2015**, *15*, 6413-6422.

14. El-Dakdouki, M. H.; Xia, J.; Zhu, D. C.; Kavunja, H.; Grieshaber, J.; O'Reilly, S.; McCormick, J. J.; Huang, X., Assessing the in vivo efficacy of doxorubicin loaded hyaluronan nanoparticles. *ACS Appl. Mater. Interfaces* **2014**, *6*, 697-705.

15. Bayer, I. S., Hyaluronic acid and controlled release: A review. *Molecules* **2020**, *25*, 2649.

16. Rao, N. V.; Yoon, H. Y.; Han, H. S.; Ko, H.; Son, S.; Lee, M.; Lee, H.; Jo, D.-G.; Kang, Y. M.; Park, J. H., Recent developments in hyaluronic acid-based nanomedicine for targeted cancer treatment. *Expert Opin. Drug Deliv.* **2016**, *13*, 239-252.

17. Tripodo, G.; Trapani, A.; Torre, M. L.; Giammona, G.; Trapani, G.; Mandracchia, D., Hyaluronic acid and its derivatives in drug delivery and imaging: recent advances and challenges. *Eur. J. Pharm. Biopharm.* **2015**, *97*, 400-416.

18. Wickens, J. M.; Alsaab, H. O.; Kesharwani, P.; Bhise, K.; Amin, M. C. I. M.; Tekade, R. K.; Gupta, U.; Iyer, A. K., Recent advances in hyaluronic acid-decorated nanocarriers for targeted cancer therapy. *Drug Discov. Today* **2017**, *22*, 665-680.

19. Mao, H.-L.; Qian, F.; Li, S.; Shen, J.-W.; Ye, C.-K.; Hua, L.; Zhang, L.-Z.; Wu, D.-M.; Lu, J.; Yu, R.-T.; Liu, H.-M., Delivery of Doxorubicin from Hyaluronic Acid-Modified Glutathione-Responsive Ferrocene Micelles for Combination Cancer Therapy. *Mol. Pharm.* **2019**, *16*, 987-994.

20. Baggio, C.; Barile, E.; Di Sorbo, G.; Kipps, T. J.; Pellecchia, M., The Cell Surface Receptor CD44: NMR-Based Characterization of Putative Ligands. *ChemMedChem* **2016**, *11*, 1097-1106.

21. Pustula, M.; Czub, M.; Labuzek, B.; Surmiak, E.; Tomala, M.; Twarda-Clapa, A.; Guzik, K.; Popowicz, G. M.; Holak, T. A., NMR fragment-based screening for development of the CD44-binding small molecules. *Bioorg. Chem.* **2019**, *82*, 284-289.

22. Liu, L.-K.; Finzel, B. C., Fragment-based identification of an inducible binding site on cell surface receptor CD44 for the design of protein-carbohydrate interaction inhibitors. *J. Med. Chem.* **2014**, *57*, 2714-2725.

23. Bhattacharya, D. S.; Svehkarev, D.; Soucek, J. J.; Hill, T. K.; Taylor, M. A.; Natarajan, A.; Mohs, A. M., Impact of structurally modifying hyaluronic acid on CD44 interaction. *J. Mater. Chem. B* **2017**, *5*, 8183-8192.

24. Lu, X. W.; Huang, X. F., Design and syntheses of hyaluronan oligosaccharide conjugates as inhibitors of CD44-Hyaluronan binding. *Glycoconj. J.* **2015**, *32*, 549-556.

25. Rocha, R. O.; Rodrigues, M. O.; Neto, B. A. D., Review on the Ugi Multicomponent Reaction Mechanism and the Use of Fluorescent Derivatives as Functional Chromophores. *ACS Omega* **2020**, *5*, 972-979.

26. Godet, T.; Bonvin, Y.; Vincent, G.; Merle, D.; Thozet, A.; Ciufolini, M. A., Titanium catalysis in the Ugi reaction of α -amino acids with aromatic aldehydes. *Org. Lett.* **2004**, *6*, 3281-3284.
27. Pouyani, T.; Prestwich, G. D., Biotinylated hyaluronic acid: a new tool for probing hyaluronate-receptor interactions. *Bioconjug. Chem.* **1994**, *5*, 370-372.
28. Banerji, S.; Wright, A. J.; Noble, M.; Mahoney, D. J.; Campbell, I. D.; Day, A. J.; Jackson, D. G., Structures of the Cd44-hyaluronan complex provide insight into a fundamental carbohydrate-protein interaction. *Nat. Struct. Mol. Biol.* **2007**, *14*, 234-239.
29. Perera, D.; Tucker, J. W.; Brahmbhatt, S.; Helal, C. J.; Chong, A.; Farrell, W.; Richardson, P.; Sach, N. W., A platform for automated nanomole-scale reaction screening and micromole-scale synthesis in flow. *Science* **2018**, *359*, 429-434.
30. Rodríguez, P.; Bautista, M. A.; González, J.; Escalera, S., Beyond one-hot encoding: Lower dimensional target embedding. *Image Vision Comput.* **2018**, *75*, 21-31.
31. Pedregosa, F.; Varoquaux, G.; Gramfort, A.; Michel, V.; Thirion, B.; Grisel, O.; Blondel, M.; Prettenhofer, P.; Weiss, R.; Dubourg, V., Scikit-learn: Machine learning in Python. *J. Mach. Learn. Res.* **2011**, *12*, 2825-2830.
32. Mahoney, D. J.; Aplin, R. T.; Calabro, A.; Hascall, V. C.; Day, A. J., Novel methods for the preparation and characterization of hyaluronan oligosaccharides of defined length. *Glycobiology* **2001**, *11*, 1025-1033.

Chapter 3 Synthesis of Liposome-SERS-hyaluronate with low-femtomolar sensitivity and its potential for image guided surgery

3.1 Introduction

Surface-enhanced Raman scattering (SERS) is a powerful optical spectroscopic technique. It is used to detect minute amounts of analyte molecules by enhancing their Raman scattering. The enhancement is typically achieved by depositing the analyte molecules onto nanostructured metal surfaces. The resulting nanostructures, known as SERS substrates, can increase the Raman signals by up to 10 orders of magnitude. SERS was first reported in 1974 by Fleischmann and Pons ¹, who used it to detect the Raman scattering of water molecules. Since then, the technique has been used for a wide range of applications, including chemical analysis, environmental monitoring, and medical diagnostics.

The most commonly employed SERS substrates are made of gold or silver. These metals have a high affinity for certain molecules, which causes the molecules to be strongly adsorbed onto the surface. The resulting nanostructures have a large surface area that amplifies the Raman signal. One simple way to produce quasi-spherical Au NPs is the use of sodium citrate to reduce HAuCl₄ in water, as developed by Turkevich in 1951 ². In 1973, Frens ³ expanded the method to produce Au NPs ranging from 16 nm to 150 nm, but the size distribution became significantly broader. Seed-mediated synthesis of AuNPs has been an effective strategy for generating uniform AuNPs ^{4, 5}. While different protocols for generating uniform AuNPs were developed, there is no literature reported protocol specifically designed for generating bright and sensitive SERS NPs with uniform size and shape distribution, partly due to the difficulty and irreproducibility of Raman dye installation to AuNPs. This chapter addresses this issue by exploring different synthesis and Raman dye installation strategies for producing bright and uniform SERS NPs.

A wide spectrum of ligands, including antibodies ⁶ and carbohydrate ⁷ has been conjugated to AuNPs for biomedical applications. Antibodies can be readily absorbed onto the metal surface of AuNPs at low salt condition at alkaline pH without causing aggregation ⁸. Other strategies include covalent conjugation such as amide formation via EDC coupling ⁹. Carbohydrates such as HA were conjugated to AuNPs of different sizes by utilizing thiol-gold interaction with thiolated HA. After attachment of thiolated HA to AuNPs, salt stability of AuNPs improved significantly ^{7, 10-12}. However, physical characterization to quantify loading percentage with this conjugation method can be difficult, and loading percentage usually was not reported in the literature.

We hypothesized that liposome can be an effective platform to bridge SERS NPs and HA. Liposomes are self-assembled vesicles made of lipids, which can be used for loading hydrophobic or hydrophilic probes due to the amphiphilic nature of the lipid ¹³. AuNP-liposome complex can be prepared using 3 different methods: thin-film hydration, reverse-phase hydration, and *in situ* growth of AuNPs. Au nanorod-liposome can be synthesized by thin-film hydration, by using an aqueous solution of Au nanorod for hydrating the lipid film ¹⁴. AuNP-liposome complex can be prepared with a similar method ^{15, 16}. Alternatively, AuNP-liposome can be prepared by reverse-phase hydration: AuNPs are added into lipid organic solution, for dehydration to form the lipid film, followed by hydration to form AuNPs-liposome complex ^{17, 18}. Another strategy is to allow *in situ* AuNPs formation in presence of liposomes, in which case small AuNPs can be effectively attached to liposome surface ^{19, 20}. However, to the best of our knowledge, there is no literature reported synthesis of 50 nm uniform SERS NP-liposome complex ²¹⁻²³. To employ liposome as the platform, SERS NPs must be effectively attached to liposomes. *In situ* formation of AuNPs, followed by Raman dye installation may not to be feasible, due to the strict requirement for

producing uniform and bright SERS NPs. In this study, thin-film hydration method was employed along with thiolated HA for producing liposome-SERS-HA complex.

SERS NPs are a promising tool for tumor margin removal in image-guided surgery. SERS NPs are well-known for strong multiplexing capability, since different flavors of SERS NPs can be synthesized using different SERS dyes. In the context of image-guided surgery, one flavor can be used as the control, while other flavors for targeting and binding with tumor cells. However, there are several challenges associated with SERS NPs for cancer imaging: 1) reproducible synthesis of SERS NPs; 2) ligand attachment for SERS NPs. This paper addresses these two issues separately by: 1) developing tris-base assisted protocol for the synthesis of SERS NPs; 2) developing liposome-SERS-HA complex for HA conjugation to SERS NPs.

3.2 Result and discussions

3.2.1 Development of a robust synthesis protocol for SERS NPs

Synthesis of SERS NPs starts from the formation of Au NP core followed by NP coating with a Raman active dye. There are in general two types of Raman dyes, i.e., resonant Raman dyes, which have optical absorbance maxima in the range of the typical plasmon resonance wavelength of Au NPs (500 – 800 nm), as well as non-resonant dyes. Our first approach for SERS NP synthesis followed a common route to Au NPs through sodium citrate reduction of tetrachloroauric(III) acid^{24, 25}. The Au NPs formed were then incubated with a non-resonant Raman dye such as S440, S420, S421, or S481 respectively, which was followed by coating of the NPs with a layer of silica through the Stöber procedure using tetraethyl orthosilicate (TEOS) to improve the stability of the particles.²⁴ However, while this method worked well for resonant Raman dyes such as IR780 and IR792, for the non-resonant dyes S440, S420, S421, and S481, the NPs gave very little SERS

signals. This is presumably because of the lower affinity of non-resonant dyes toward Au NP binding.

As non-resonant Raman dyes can give Raman spectra with lower background and peaks with narrower bandwidth, it is desirable to develop a protocol that SERS NPs can be prepared bearing non-resonant dyes. A variety of reaction conditions were examined ²⁶, which included varying the sequence of dye addition vs formation of Au NPs, and addition of additives such as ammonia hydroxide to stabilize Au NPs formed before installation of the Raman dye. However, none of these procedures yielded stable NPs with strong SERS signals.

Another observation from the synthesis was that by controlling the reaction condition, sodium citrate reduction can lead to different Au NP core size. It is known that the ideal core size for maximum SERS enhancement was around 50 nm to 60 nm ²⁷. Our results were consistent with the literature, as the 13 nm AuNPs we synthesized ²⁸ only produced minimal SERS signals. When we pursued the synthesis of particles larger than 30 nm through sodium citrate reduction, significant heterogeneities in shape and size of Au NPs produced were observed (**Figure 3.2a**) ²⁹.

The aforementioned difficulties encountered in SERS NP synthesis prompted us to examine alternative synthetic procedures. There are many literature methods for the preparation of homogeneous AuNPs, including transition metal ion-assisted synthesis ^{29, 30}, seed mediated synthesis with sodium citrate ^{4, 5}, seed mediated growth with tris base ^{31, 32}, and cetyltrimethylammonium bromide (CTAB) assisted synthesis ³³⁻³⁵. However, few of them have been applied to the formation of SERS NPs with strong SERS signals for both resonant and non-resonant Raman dyes. After screening through multiple conditions, the seed mediated growth method with tris base turned out to be the best approach in our hands.

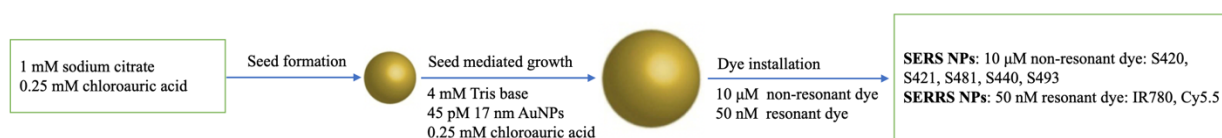


Figure 3.1 Tris base assisted synthesis of SERS NPs. 17 nm seeds were first synthesized via sodium citrate reduction, followed by seed mediated growth of homogenous 50 nm AuNPs via tris base at 100 °C. Raman dye was added right after the formation of AuNPs and stirred for 1 min, followed by immediate cooling down in an ice bath. This method worked for non-resonant or resonant dye yielding bright SERS-NPs, while the working concentration differed for two orders of magnitude for non-resonant dye (10 μ M) vs resonant dye (50 nM).

For the seed mediated growth strategy, as shown in **Figure 3.1**, 17 nm Au NP seeds were synthesized first with sodium citrate as the reducing agent. The seeds were then mixed with tris base solution heated at 100 °C, followed by the addition of tetrachloroauric acid, which triggered the NP growth to form 50 nm AuNPs by controlling the number of seeds. To install the Raman dye, among various conditions explored, we discovered that upon formation of the 50 nm Au NPs, 10 μ M Raman dye such as S420 should be immediately added to the NP solution at 100 °C. The resulting SERS NPs were stable in the solution and gave bright Raman signals. Adding the dye after the AuNP solution had cooled down, or adding the dye before or during seeded growth of the NPs failed to produce NPs with strong Raman signals. It is thus suggested that non-resonant Raman dye can only be installed onto AuNPs at a very small time window right after the formation of AuNPs, presumably because the nascent Au NP surface has strong binding to the Raman dye. Characterization of SERS NPs of both tris base assisted approach and sodium citrate approach was shown in **Figure 3.2**.

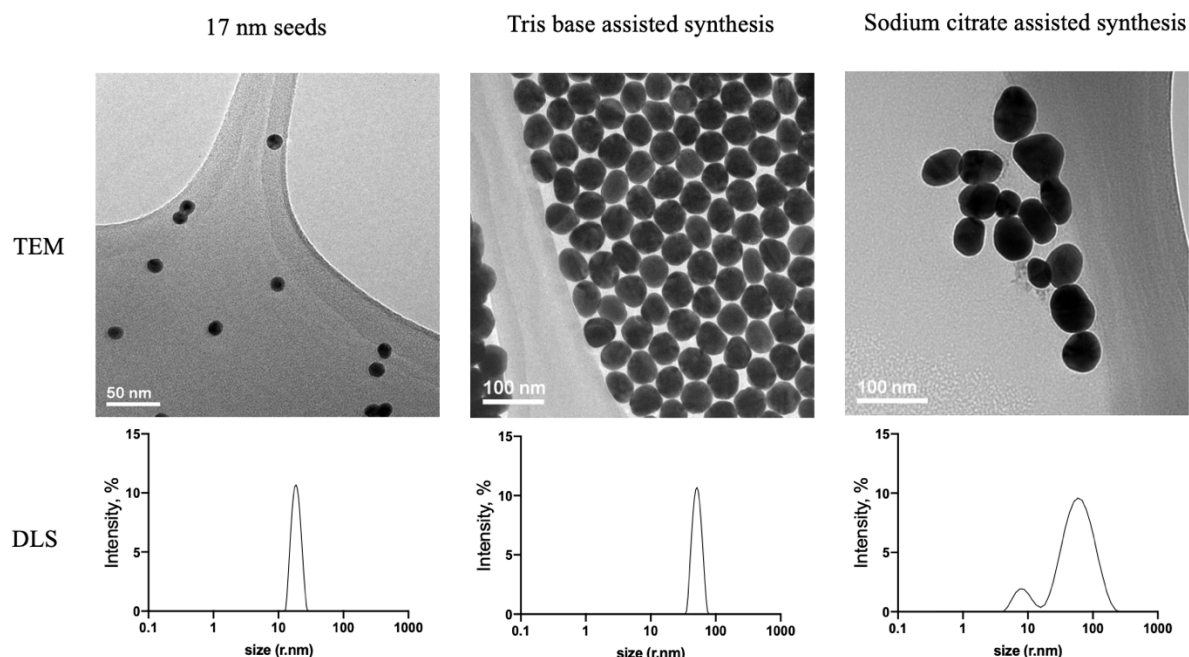


Figure 3.2 Characterizations of SERS NPs synthesized via the sodium citrate reduction method, and the tris-base reduction method. Sodium citrate reduction can lead to heterogeneity when the targeted size is above 30 nm as shown in TEM images. This is also indicated by size distribution in DLS. For the tris-base method, 17 nm seeds were first synthesized with sodium citrate reduction, followed by seed-mediated growth of homogeneous SERS NPs with tris base as a weak reducing agent. With seed mediated, tris base assisted synthesis, there was a significant improvement both in terms of size and homogeneity of shape.

To test the generality of our approach, a panel of 14 potential non-resonant Raman dyes (**Figure 3.3**) was investigated. S421, S440, and S481, which have been used to construct SERS NPs³⁶, produced NPs with strong SERS Raman signals. Interestingly, S470 generated nearly identical SERS fingerprints as S440 presumably due to their structural similarities. S493 also produced strong Raman signals with distinctive fingerprint patterns, while all other molecules tested did not yield bright SERS NPs. It is not clear what structural features of the molecules render them suitable Raman dyes *a priori* based on the results from our study. Computational modeling on molecular binding to AuNPs surface may yield insights on this issue and guide future design.

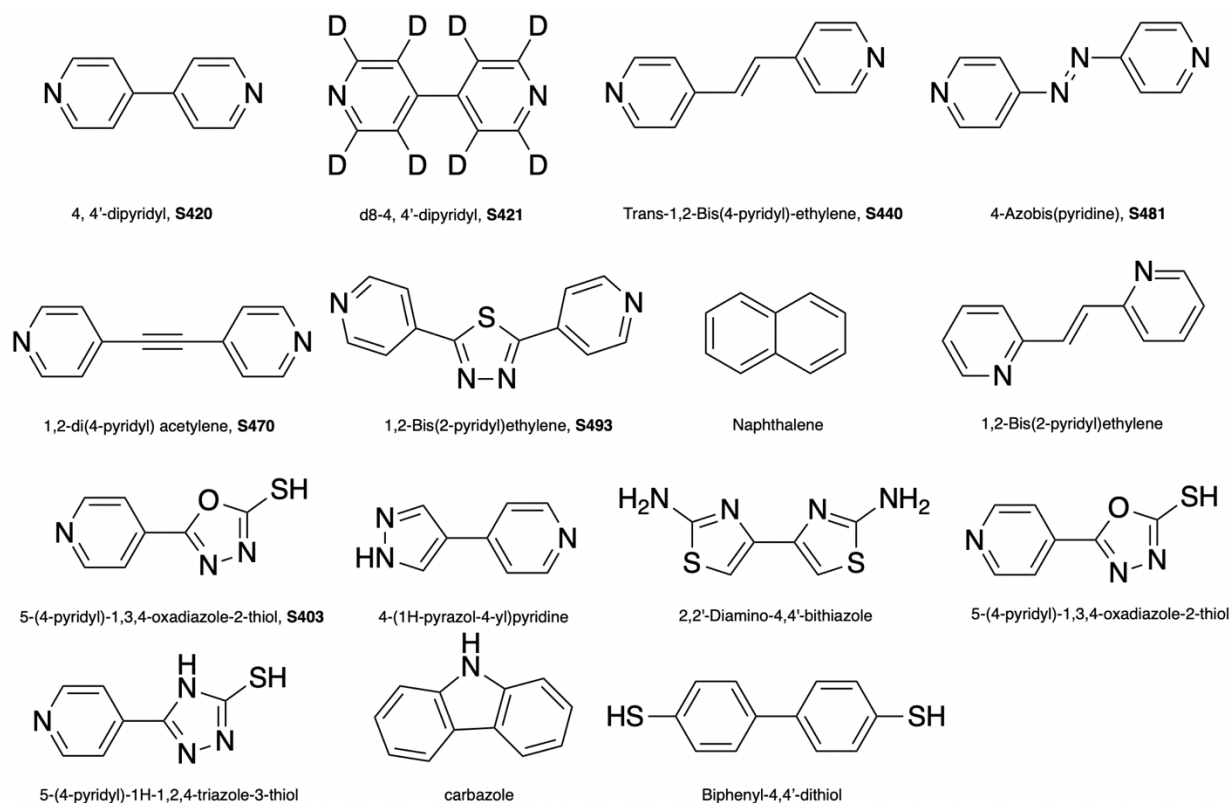


Figure 3.3 Structures of non-resonant Raman dyes and other compounds screened.

Next, resonant Raman dye such as IR780 was investigated to produce surface-enhanced resonant Raman scattering nanoparticles (SERRS NPs). When 10 μM of the IR780 dye was used as for the non-resonant dye, it led to instantaneous aggregation of AuNPs. Upon careful optimization, it was found that 50 nM of IR780 was sufficient to produce bright SERRS NPs, which is 200 times less than the concentration used for non-resonant dye such as S420. This supported the idea that with its extended conjugative structure, a resonant Raman dye can have a higher affinity to Au NPs as compared to a non-resonant Raman dye. Other near-infrared dyes including IR792, ICG, Cy5.5, Cy3, and CW800 were explored for SERRS NP development as well, as shown in **Figure 3.4**. However, only Cy5.5 produced SEERS NPs with strong signals. It is worth noting that IR792 would produce the same fingerprint as IR780.

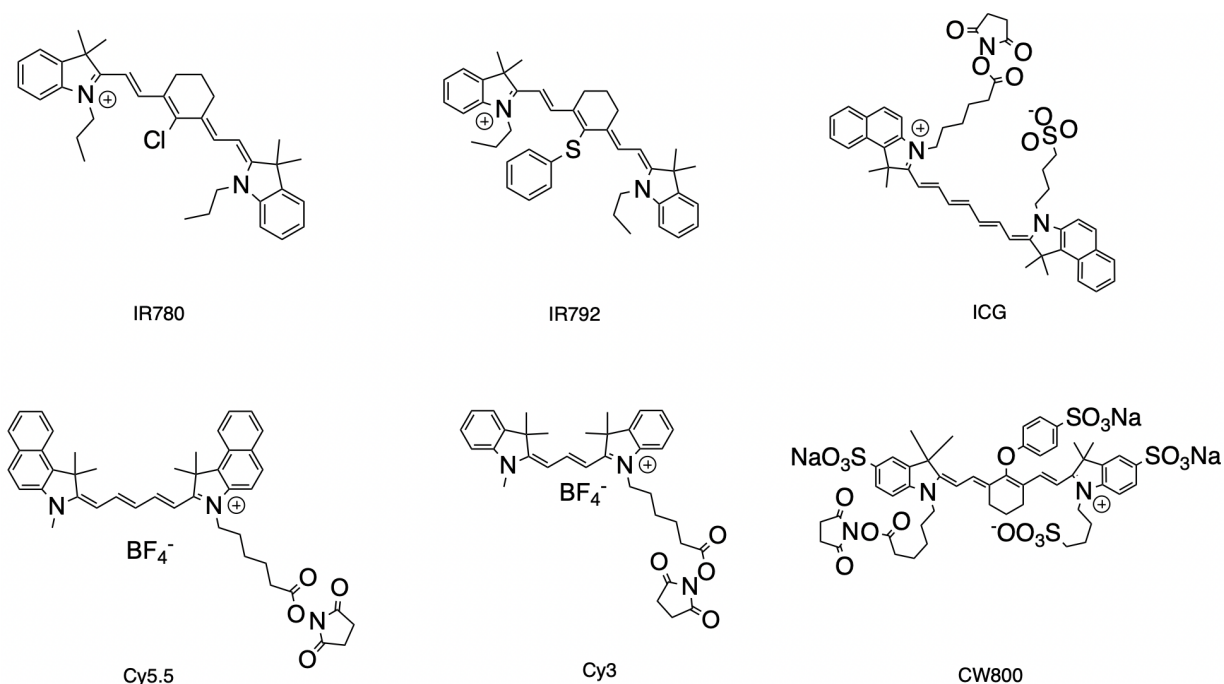


Figure 3.4 Structures of resonant Raman dyes and other compounds screened.

3.2.2 Other dye installation methods

It is surprising to find that the working concentrations for resonant Raman dye (S420, S421, S481, and S440) and non-resonant Raman dye (IR780 and Cy5.5) differed by two orders of magnitude. Also, AuNPs from tris base synthesis demonstrated significantly better surface stability during Raman dye installation. Based on these two pieces of information, we hypothesized that the dye concentration for sodium citrate-based synthesis may be further optimized: by reducing dye concentration by two or three orders of magnitude, the need for ammonia hydroxide as an extra stabilizer may be removed, yielding brighter SERS signals. This hypothesis is confirmed with S420, S421, S481 and S440. SERS NPs can be synthesized with minimal aggregation while installing the dye at only 0.1 μM . S493 would not produce signal with 0.1 μM , while higher concentration would lead to aggregation of AuNPs. For resonant dyes, Cy5.5 and IR780 were explored with this protocol. However, by employing Cy5.5 and IR780 at 0.005 μM for dye

installation, the resulting NPs showed minimal signals. Cy5.5 at 0.05 μM would cause aggregation, leading to NPs with minimal signals. This may be explained that AuNP surface coated with sodium citrate or tris base would have different surface behaviors towards resonant dyes.

Due to higher affinity of resonant Raman dyes toward AuNPs surface, IR780 and Cy5.5 can be installed by incubating 2 μM resonant Raman dye with 1.5 nM AuNPs at room temperature. Employing non-resonant dyes such as S440 would not produce visible signals.

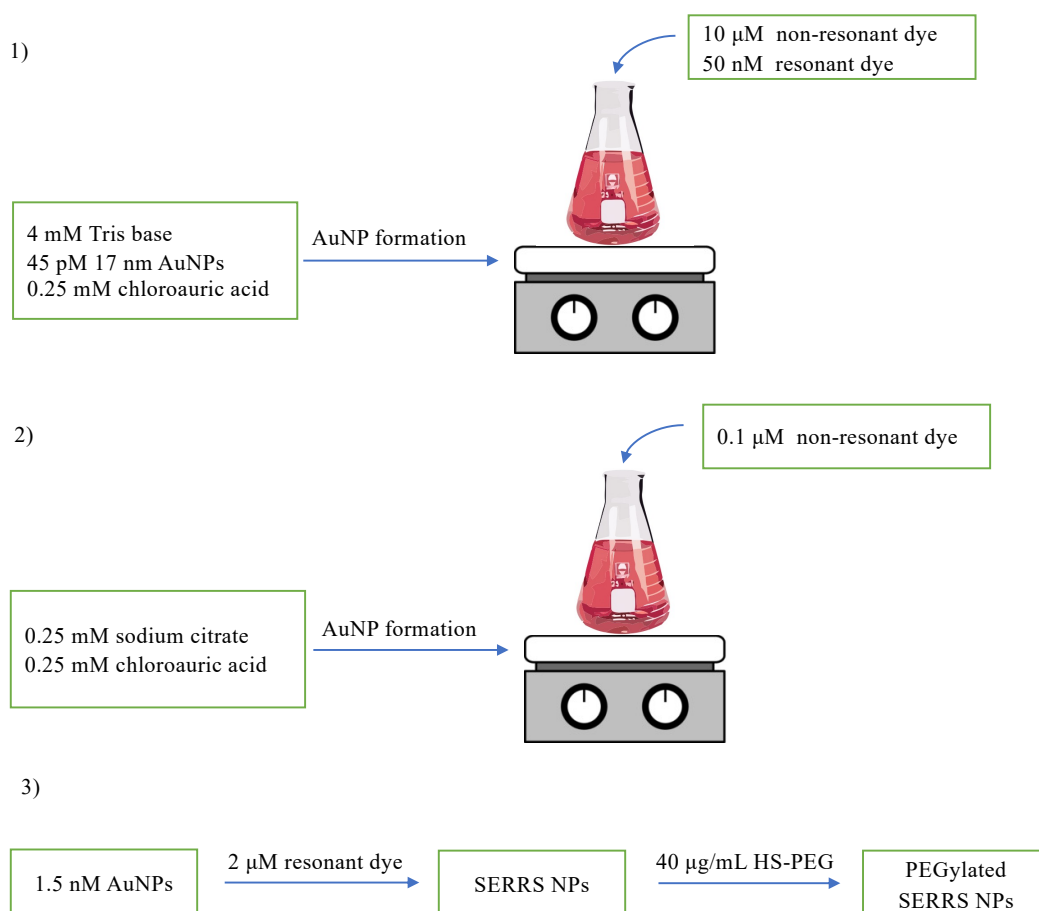


Figure 3.5 Various methods for the synthesis of SERS NPs. 1) Tris base assisted synthesis of SERS NPs. This method works for non-resonant or resonant dye, while the working concentrations differed by two orders of magnitude. 2) Sodium citrate assisted synthesis of SERS NPs with heterogeneous size and shape distribution. This method can only work for non-resonant dye, with working concentration to be 100 times smaller than the one for tris base assisted synthesis. 3) Raman dye installation with concentrated AuNPs. 50 nm AuNPs from tris base assisted synthesis were incubated with 2 μ M resonant dye for 10 mins, followed by PEGylation. This method can only work for resonant dye. Dye installation has to precede PEGylation to yield SERS signals.

3.2.3 Detection limit quantification of SERS NPs

Detection limits of seven different flavor of SERS NPs from sodium citrate assisted synthesis were evaluated with Renishaw inVia Reflex Raman system, as shown in **Figure 3.6**. Briefly, in 96 well plate, 200 μ L SERS NPs (S420, S421, S440, S481, S493, IR780, and Cy5.5) of varying concentrations: 200 pM, 100 pM, 20 pM, 4 pM, 800 fM, 160 fM, 32 fM, 6 fM were added into the wells. The highest peak of each flavor was used to quantify the detection limit. As

shown in **Figure 3.6**, the detection limit of S420, S440, S481, IR780 and Cy5.5 is as low as 6 fM using the Renishaw system.

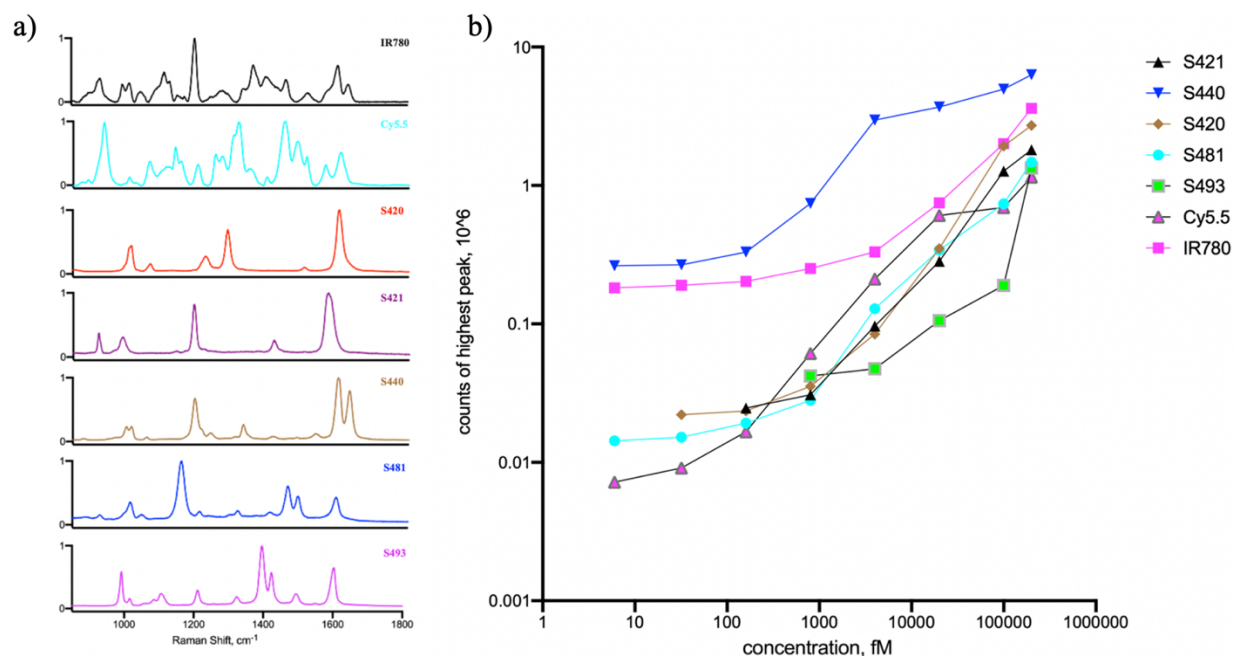


Figure 3.6 (a) Raman spectra of SERS particles (S420, S421, S440, S481, IR780, and Cy5.5) acquired by the Renishaw system; (b) The highest peaks of Raman spectra acquired by the Renishaw system of each flavor at different concentrations.

3.2.4 Ratio metric evaluation of mixture of SERS flavors

To evaluate the demultiplexing algorithm, the phantoms with a mixture of SERS solutions at seven different ratios of individual types of SERS-NPs were prepared and the Raman spectra were acquired using the Andor Raman system, as shown in **Figure 3.7**. Three main parameters for ratio determination were acquired: 1) the reference spectra for each flavor at the highest concentration of each flavor; 2) background spectra, i.e., the spectra of container (plastic tube) and water; 3) spectra of the solutions of various mixed NPs. All these spectra were fed to the demultiplexing algorithm, and the results were shown in **Figure 3.7b** below.

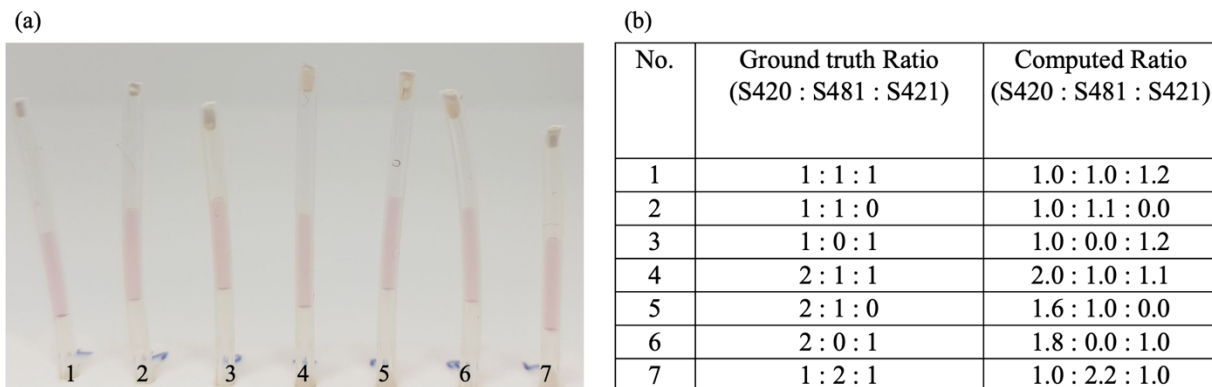


Figure 3.7 Ratio metric experiment. (a) the phantom with the mixture SERS solution (S420, S481, and S421); (b) the result of ratio estimation using the demultiplex algorithm.

3.2.5 Cytotoxicity evaluation of SERS NPs

For biological applications, it is important that the NPs are biocompatible. *In vitro* cytotoxicity assay was performed to evaluate the toxicity of SERS NPs toward Raw 264.7 cells using the colorimetric MTS assay. The results of the cytotoxicity assay showed that SERS NPs were not toxic up to the highest concentration tested (100 pM), as shown in **Figure 3.8**.

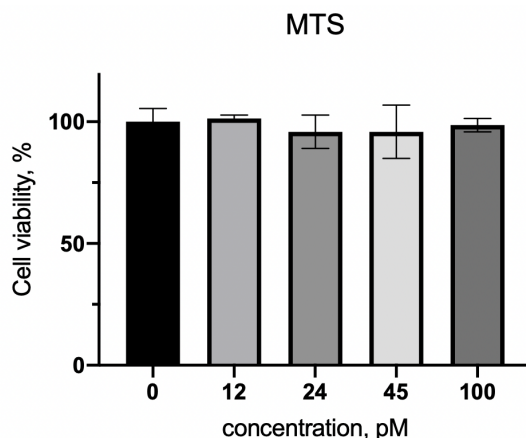


Figure 3.8 MTS assay with S420 prepared from the tris base assisted synthesis. SERS-NPs were pegylated to prevent aggregation in cell media. Various concentrations of S420-PEG were incubated with Raw cells for 3 hours: 0 pM, 12 pM, 24 pM, 45 pM and 100 pM. No cytotoxicity was observed for all concentrations tested.

3.2.6 Ligand attachment to SERS NPs

In order to bestow targeting abilities of the SERS NPs, it is important to be able to attach targeting ligand to the NPs. The first approach attempted was TEOS coating with non-resonant dye labeled AuNPs³⁷. During TEOS coating, AuNPs were dissolved in isopropanol solution with the addition of ammonia hydroxide to facilitate TEOS hydrolysis. The resulting AuNPs with TEOS coating had minimal SERS signals. SERS signals were monitored during the TEOS process. It was found that the addition of ammonia hydroxide during TEOS coating significantly reduced SERS signals. Even in presence of non-resonant dye up to 1 mM during TEOS coating, it would still not yield TEOS coated SERS with strong signals. Thus, we did not proceed with TEOS coating for SERS NPs.

To attach biomolecules such as HA, thiol group can be installed to HA, and gold-thiol interaction^{7, 10-12, 38} can be employed for attachment of HA to SERS NPs. Briefly, SERS NPs were mixed with thiolated HA and incubated overnight followed by repeated centrifugation to remove unbounded HA. Characterizations of SERS-HA and SERS-PEG are shown in **Figure 3.9**. We

observed size increase in DLS and salt stability in PBS after HA attachment. However, with this method, SERS-HA showed relatively weak competition in competitive ELISA against biotinated HA for CD44 binding even at high concentrations of SERS NPs (250 pM). It is suspected that dye installation may have interfered with HA attachment. However, AuNPs without dye installation did not lead to a better result. The effect of molecular weight of HA was examined next. Thiolated HAs at 3 different molecular weight (10 kDa, 250 kDa and 1500 kDa) were used for attachment to SERS NPs as we expected higher molecular weight HA to bind better with the gold surface. However, no improvements in Raman intensities were observed (**Figure 3.9c**).

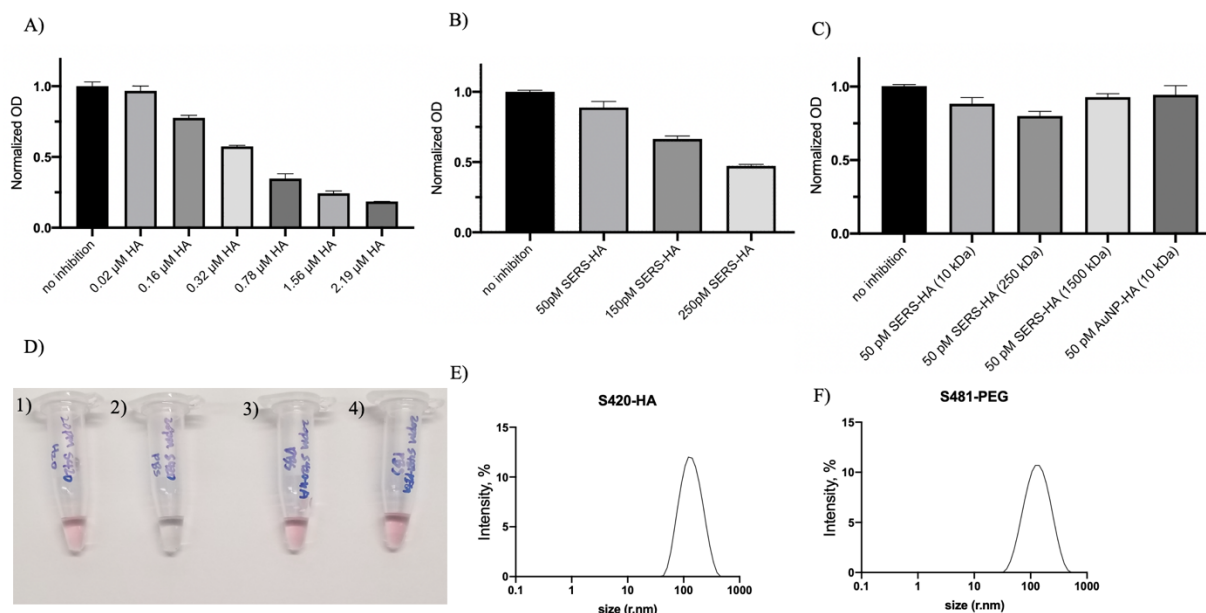


Figure 3.9 Characterizations of SERS-HA and SERS-PEG. A) HA competition with b-HA at various concentrations. B) Dose-dependent competition of SERS-HA (10 kDa) with b-HA. SERS-HA showed weak competition even at elevated concentration at 250 pM. C) Competition of 50 pM SERS-HA with HA at different molecular weight: 10 kDa, 250 kDa and 1500 kDa. Similar results were observed across 3 different molecular weights. D) Pictures of SERS, SERS-HA and SERS-PEG in MilliQ water or PBS: 1) 20 pM S420 in MilliQ water; 2) 20 pM S420 in PBS, aggregation is indicated by color change from red to black; 3) 20 pM S420-HA in PBS; 4) 20 pM S481-PEG in PBS. HA or PEG attachment to SERS NPs significantly improved salt stability of SERS NPs in PBS. E, F) DLS of S420-HA and S481-PEG. Size increase was observed compared with unmodified SERS NPs.

To address this issue, our hypothesis is that SERS NPs can be potentially anchored to some polymeric systems to enhance ligand attachment. Liposome was explored as a platform to bridge SERS NPs and HA. Liposomes, self-assembled vesicles made of lipid bilayers, are widely used as drug delivery vehicles. Liposome can be used to encapsulate both hydrophilic and hydrophobic drugs, and to target specific cell types by attaching ligands or antibodies to the membrane surface¹³. To load hydrophilic probes, the thin-film hydration method is widely applied. Briefly, the dry lipid membrane is hydrated with hydrophilic probe-containing aqueous solution to form liposomes. SERS NPs are coated with tris base and thus are hydrophilic on the surface. The idea is to load SERS NPs into liposome and attach HA during the process. Several strategies were employed: 1)

use SERS NP solution to hydrate the lipid film; 2) premix SERS NPs with HS-PEG, incubate overnight, and use that to hydrate the lipid film; 3) premix SERS NPs with HS-HA, incubate overnight, and use that to hydrate the lipid film; 4) premix SERS NPs with HS-PEG and HA, incubate overnight, and use that to hydrate the lipid film.

Strategy 1 caused SERS NPs aggregation during the hydration process, as indicated by color change. To overcome this, SERS NPs were first PEGylated with 5 kDa HS-PEG to stabilize the surface, leading to minimal aggregation, as used in strategy 2. Strategies 3 and 4 both yielded liposome-coated SERS NPs, but only strategy 3 yielded liposome-coated SERS NPs with strong HA activity, as shown in **Figure 3.10**. It is proposed that HA attachment to liposome is through both thiol-gold interaction ³⁸, and HA binding to liposome ³⁹. For Liposome-SERS-HA, strong competition from HA was observed at 20 pM (**Figure 3.10a**). This is a significant improvement from the method without liposome. By comparing with HA inhibition at various concentrations, we can estimate that 20 pM liposome-SERS-HA corresponds to about 2.19 μ M HA, which is 37.5 μ g/mL. Based on this, the overall loading percentage of HA was estimated as 18%. HA attachment was confirmed with the carbazole assay ⁴⁰, which estimated the loading percentage of HA as 5%. Higher loading percentage of HA from ELISA can be explained by the enhanced multi-valency effect after HA attachment to liposome surface. To benchmark the CD44 binding ability of liposome-SERS-HA, 100 pM Liposome-SERS-HA would be as equivalent to 10.95 μ M 10 kDa HA.

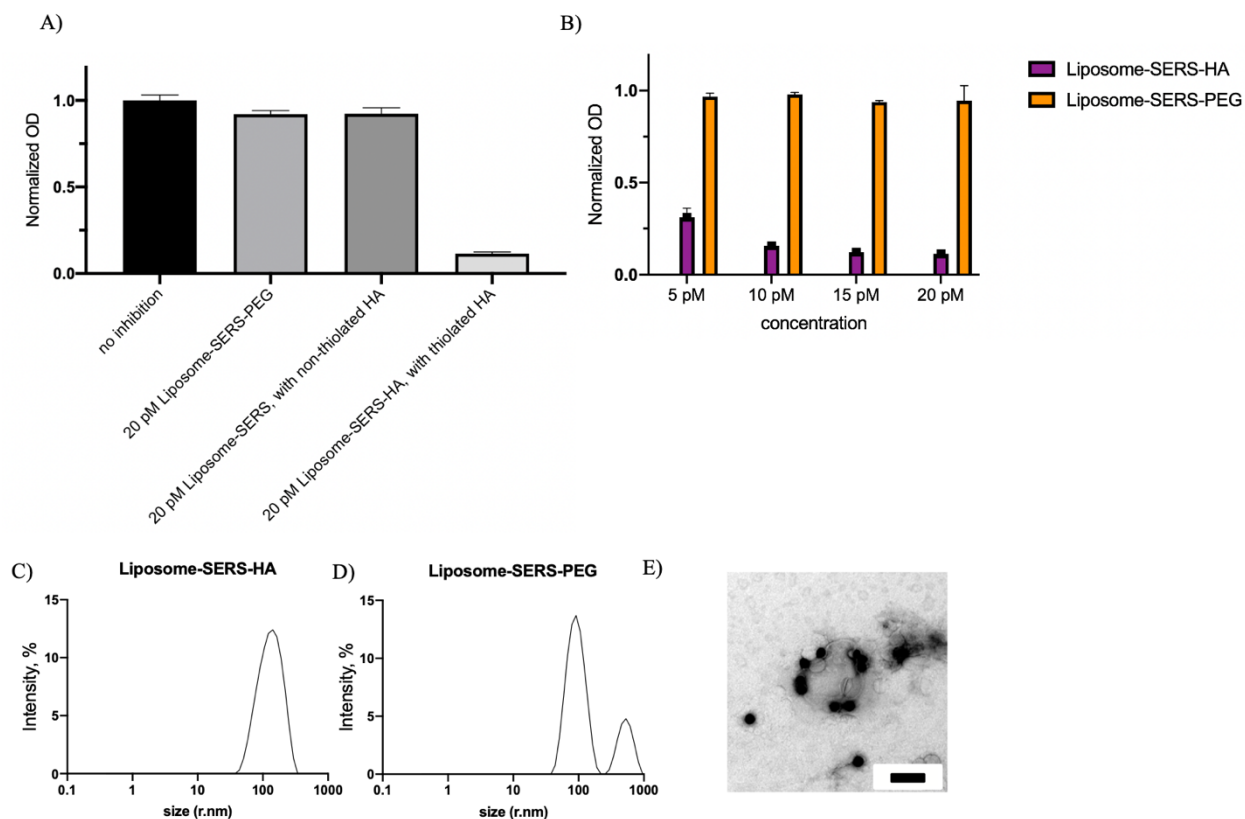


Figure 3.10 Characterizations of Liposome-SERS-HA and Liposome-SERS-PEG. A) Competitive ELISA showed that HA attachment was successfully only with thiolated HA. Strong competition was observed at only 20 pM when the particles were made with thiolated HA. B) Dose dependent competition of Liposome-SERS-HA. Liposome-SERS-PEG showed no competition at all four concentrations. DLS of C) liposome-SERS-HA and D) liposome-SERS-PEG respectively. E) TEM images of liposome-SERS-HA. SERS NPs were chelated to the surface of liposome. 0.5 % uranyl acetate staining was employed for TEM imaging (scale bar: 200 nm).

3.2.7 Liposome-SERS HA NPs enabled successful image-guided surgery of spontaneous breast cancer model in mice

Breast cancer is the leading cause of death in female cancer patients. Surgery is the primary approach for cancer removal. However, it can be challenging to completely remove cancer through surgery as some tumor may have infiltrated into surrounding normal tissues. Breast cancer surgeons often rely on touch and experience during surgery to determine the tumor margin. Nevertheless, there are still significant incidences that residue tumor was left in the surgical sites

as observed by the presence of tumor at the margin of breast tissues removed. Thus, a method that can guide the surgeon to completely remove tumor will be tremendously beneficial.

To test the possibility of image guided surgery, a spontaneous breast cancer model was built using the MUC1/MMTV breast cancer model. These mice spontaneously develop breast cancer in 4-6 months with tumor morphology similar to those observed in human patients. During surgical removal of tumor, we sprayed the liposomal-SERS-S421-HA solution to the tumor site for tumor detection. While Raman signals could be observed in the tumor site upon rinsing the tissues to remove unbound particles, it was unclear of the extent of non-specific binding of NPs by the tissues. To resolve this, we synthesized the liposome-S440-PEG NP via similar synthetic methods as the liposomal-S421-HA. A solution was prepared by mixing liposome-S421-HA and liposome-S440-PEG at 1 : 1 ratio. Tumor was sequentially removed followed by spraying of the mixed NP solution and removal of unbound particles. As shown in **Figure 3.11**, after the first cut of the tumor, particle spraying and washing of unbound particles, the liposome-S440-PEG also stained part of the tumor site including surrounding normal tissues, which reflected the non-specific binding by the NPs. To more precisely determine the location of tumor, the Raman signals from the surgical site were acquired and deconvoluted. The ratio of the signal intensities from S421 and S440 was calculated. Hotspots with significantly higher S421 signals in ratiometric images of the tumor would be indicative of tumor presence due to the high levels of CD44 expression in tumor. After removal of tumors three times, the surgical site was free of tumor signals. Sequential tumor removal and corresponding IHC and H&E images of resected tumor were shown in **Figure 3.11**. Ex vivo staining was carried out with the surgical removed tumor, and other tissues including liver, heart and kidney tissue. Resected tissues were stained with a mixture of Liposome-

S421-HA and Liposome-S440-PEG, followed by repeated washing with PBS. Raman imaging was performed and the ratiometric images were generated as shown in **Figure 3.12**.

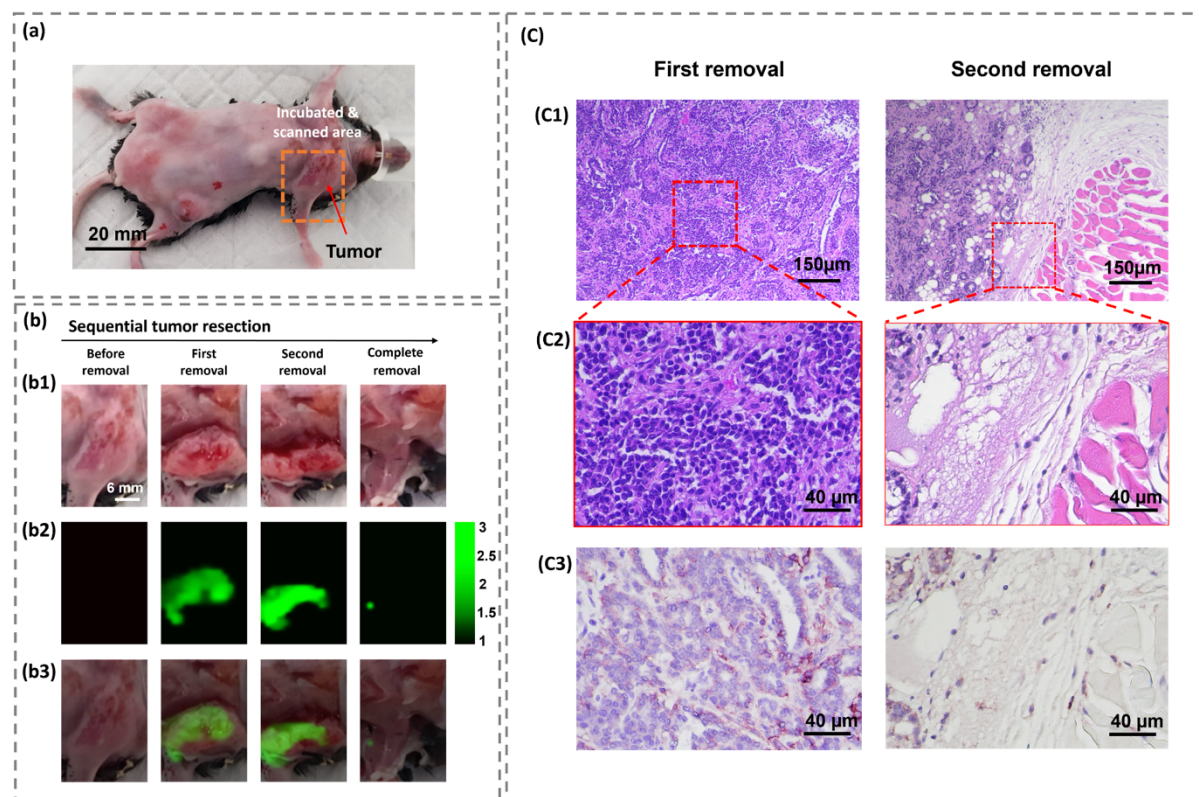


Figure 3.11 Raman Image-guided surgery using the mixture solution of Liposome-S421-HA and Liposome-S440-PEG. (a) photograph of the tumor mouse; (b) Sequential tumor resection, (b1) photographs of scanning area, (b2) the ratiometric Raman (S421/S440) images, (b3) overlaid images; (c) H&E and IHC images of resected tumors from (b), (c1-c2) H&E images acquired by 10 x and 40 x magnification, respectively, (c3) the corresponding IHC images acquired by 40 x magnification.

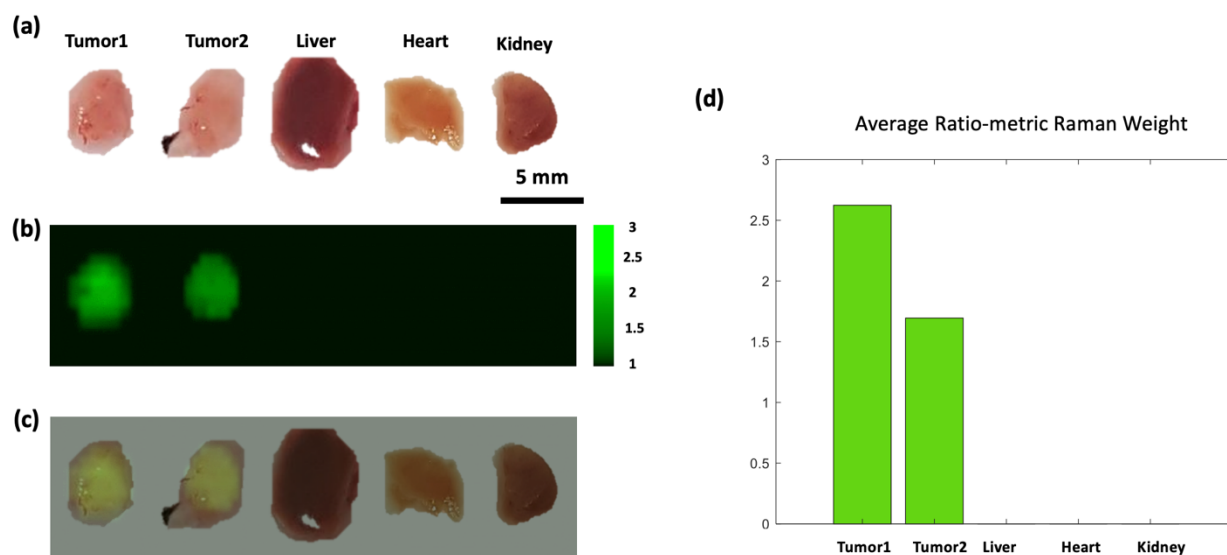


Figure 3.12 Ratiometric images of the mixture solution of Liposome-S421-HA and Liposome-S440-PEG applied on the tumor and control tissues. (a) photograph of specimens; (b) ratiometric Raman image(S421/S440) ; (c) overlaid image between the photograph and the ratiometric Raman image; (d) the average of Ratiometric Raman weight.

3.3 Conclusion

In summary, a one-pot synthesis of SERS NPs leading to a low-femtomolar detection limit was developed for both resonant and non-resonant Raman dye: S440, S420, S421, S481, IR780, and Cy5.5. The synthesized 50 nm spherical SERS NPs have homogeneous size and shape distribution, which is a significant improvement from the more traditional sodium citrate assisted synthesis. Overall, three novel methods for effective installation of Raman dyes to AuNPs were developed. Liposome as an effective platform was employed to yield liposome-SERS-HA complex, which had significantly higher CD44 binding compared to the corresponding SERS-HA NPs without the liposome formulation. The bright SERS signals and the strong CD44 binding of the liposome-SERS-HA particles enabled successful image-guided surgical removal of breast cancer from a spontaneous mouse breast cancer model. In summary, this is the first report of 1) one-pot synthesis of SERS NPs with low-femtomolar detection limit; 2) synthesis of liposome-

SERS NP (50 nm) complex; 3) *in vivo* image-guided surgery for spontaneous mouse breast cancer model.

3.4 Experimental section

3.4.1 Reagents

Sodium hyaluronan (10 kDa) was purchased from Lifecore Biomedicals. HS-PEG and HS-HA of different molecular weight were purchased from Creative PEGWorks. Sodium citrate, tris base, and chloroauric acid, 4,4'-dipyridyl (S420), d8-4,4'-dipyridyl (S421), trans-1,2-bis(4-pyridyl)-ethylene (S440), 4-azobis(pyridine) (S481), 2,5-bis(4-pyridyl)-1,3,4-thiadiazole (S493), IR780 and Cy5.5, cholesterol as well as other chemicals were obtained from Sigma unless otherwise stated. 1,2-Dipalmitoyl-sn-glycero-3-PC (DPPC) was obtained from Cayman Chemical.

3.4.2 Sodium citrate assisted synthesis of SERS NPs

A 250 mL Erlenmeyer flask was cleaned extensively by washing with Aqua regia, then with DI water. 100 mL MilliQ water was added to the 250 mL Erlenmeyer flask, boiled and discarded for further washing. Then 48 mL MilliQ water and 0.5 mL 25 mM HAuCl₄ solution were added into the 250 mL Erlenmeyer flask, and capped with aluminum foil. For a standard hot plate (Corning PC-4200), the stirring was set to 500 RPM, and heating was set to 500, for vigorous stirring and heating. Under vigorous stirring, the solution was heated to boiling, followed by the addition of 0.75 mL 5 mg/mL sodium citrate. Color change occurred within 4 mins, indicating the formation of AuNPs. After the formation of AuNPs, 5 μ L 1 mM S440, S420, S421, or S481 in DMF was added. Stirring was kept for another 2 mins, followed by cooling down in ice bath, and centrifugation at 5000 g at 4 °C for 10 mins to collect SERS NP pellet.

3.4.3 Tris base assisted synthesis of SERS NPs

Synthesis of 17 nm seeds: a 250 mL Erlenmeyer flask was cleaned extensively by washing with Aqua regia, then with DI water. 100 mL MilliQ water was added to the 250 mL Erlenmeyer flask, boiled and discarded for further washing. 48 mL MilliQ water was added into the Erlenmeyer flask, and capped with aluminum foil. For a standard hot plate (Corning PC-4200), the stirring was set to 500 RPM, and heating was set to 500, for vigorous stirring and heating. When the solution started to boil, 0.5 mL 25 mM HAuCl₄ solution was added, followed by the addition of 1.5 mL 1% sodium citrate solution. With the addition of sodium citrate, AuNPs formation was initiated. Color change occurred within 5 mins, indicating the formation of AuNPs. The solution was kept stirring for another 8 mins after the addition of sodium citrate. Gold colloidal was then cooled down in ice bath. The volume of the solution is adjusted to 50 mL.

Synthesis of 50 nm SERS NPs: a 250 mL Erlenmeyer flask was cleaned extensively by washing with Aqua regia, then with DI water. 100 mL MilliQ water was added to the 250 mL Erlenmeyer flask, boiled and discarded for further washing. 91 mL MilliQ water was added into 200mL Erlenmeyer flask, capped with aluminum foil. For a standard hot plate (Corning PC-4200), the stirring was set to 500 RPM, and heating was set to 500, for vigorous stirring and heating. When the solution started to boil, 4 mL 0.1 M tris-base was added, and heat was reduced to 300. Then 3 mL seed solution was added, followed by the addition of 1 mL 25 mM HAuCl₄. The addition of chloroauric acid initiated the formation of AuNPs. Color change occurred within 3 mins. Then 10uL Raman dye solution (100 mM for S420, S420, S421, S481 and S493, 500 μ M for IR780, Cy5.5) was added and stirring was kept for exactly 1 min. Then gold colloidal was cooled down in ice bath for 3 mins, followed by centrifugation at 5000 g at 4 °C for 10 mins. Supernatant was carefully removed without disturbing the pellets. SERS NPs were redispersed

into MilliQ water. Concentration was measured using calibration curve established with absorption at 527 nm.

3.4.4 Synthesis of Liposome-SERS NPs complex

Liposomes-SERS NP complexes were prepared by a thin film hydration method. Briefly, 2 mg DPPC and 0.5 mg cholesterol was dissolved in 0.5 mL CHCl_3 / MeOH co-solvent (2 : 1), and dried using a rotary evaporator at 37 °C to form lipid film. The film was hydrated with SERS-HA or SERS-PEG solution. For SERS-HA, 500 μL 200 pM SERS NPs was mixed with 100 μL 10 mg/mL HS-HA (10 kDa) and incubated overnight. For SERS-PEG, 500 μL 200 pM SERS NPs were mixed with 10 μL 10 mg/mL HS-PEG (5 kDa) and incubated overnight. During hydration, the solution was kept still for 30 mins without sonication. Then the solution was pipetted up and down to facilitate the hydration process, followed by water bath sonication. The complex was centrifuged down at 2500 g for 5 mins, washed two times by repeated centrifugation to remove unbounded PEG, HA and empty liposome, and redispersed back in to MilliQ water.

3.4.5 Carbazole assay for hyaluronan quantification

The sample (50 μL) was mixed with 200 μL 25 mM sodium tetraborate in sulfuric acid in a 0.7 mL tube. The mixture was heated at 100 °C for 10 min. After cooling down at room temperature, 50 μL 0.125% carbazole in absolute ethanol was added. The mixture was heated at 100 °C for another 10 mins. After cooling down at room temperature, 200 μL of the mixture was transferred into 96 well microtiter plate for reading at wavelength of 550 nm.

3.4.6 Image-guide surgery through SERS imaging

The staining solution was prepared by mixing 500 pM liposome-S420-HA and 500 pM liposome-S440-PEG at 1 : 1 ratio. A MUC1/MMTV mouse was put under anesthesia with 5% isoflurane in oxygen. The tumor area was first opened, and the tissue background was scanned.

Then 50 μ L of the staining solution was topically applied to both the tumor area and surrounding normal area. After 15 mins, the staining area was washed with PBS for three times. Raman mapping of the tissue area was obtained before and after the washing process. Then a portion of the tumor was removed, followed by repeated staining and imaging. The whole process is repeated until all the tumor is removed. Dissected tissue was fixed with paraformaldehyde (4 %) for H&E and IHC staining.

3.4.7 Competitive ELISA

In a 96 well-plate, 100 μ L of goat antihuman IgG FC γ (3 μ g/well, Millipore, cat no. AP113) in PBS buffer was added to each well. The plate was covered with aluminum foil and incubated at 4 °C overnight. The wells were then washed 3 times with 200 μ L PBST buffer (0.5% Tween 20) as follows: the plate was emptied by inversion over a sink, tapped against some layers of soft paper tissue to remove residual liquid, and then washed with buffer repeatedly (insufficient washings may lead to undesired high background). Blocking was completed by adding 5% BSA in PBS (200 μ L) to each well followed by incubation at 37 °C for 2 h. The plate was then washed as described above. 100 μ L of CD44-FC γ chimera (0.2 μ g/well, R&D systems, cat no. 3660-CD) in PBS buffer was then added to each well and incubated at 37 °C for 45 min. The plate was washed 3 times with 200 μ L PBST buffer (0.05% Tween 20) as before. 100 μ L of b-HA (0.5 μ g/well) and 100 μ L HA 10 kDa (1 μ g/well), or liposome-SERS-HA were then added to each well and incubated at room temperature for 2 h. The plate was then washed 3 times with 200 μ L PBST buffer (0.05% Tween 20) and twice with PBS buffer. 100 μ L Avidin-HRP in 0.2% BSA-PBS solution was then added to each well and incubated at room temperature for 1 h. The plate was washed 3 times with 200 μ L PBST buffer (0.05% Tween 20) and twice with PBS buffer. 100 μ L of chromogenic TMB solution was added to each well, homogenized, and incubated for 15 min, or until a blue color

appeared. The plate should be protected against light during this incubation. The reaction was then quenched by adding 0.5 M H₂SO₄ (50 µL) to each well. For quantitative measurements, it was important that each well was incubated for exactly the same length of time. Optical absorbance was directly assessed through the bottom of the microwell plate using an automated ELISA plate reader (Biorad) at 450 nm.

3.4.8 MTS assay with SERS NPs

Raw 264.7 cells were dispersed in DMEM cell culture media containing FBS (10 %) and cultured in a 96-well plate in the presence of 5 % CO₂ at 37 °C. Then, cells were incubated with various concentrations of SERS-PEG for 2 hours. The media was removed, and MTS reagent (Promega, cat no. G358C) dispersed in medium (10 %) was added and incubated for another 2 hours until the color was developed. The absorption of each well was measured at 490 nm using a SpectraMax M3 plate reader. Wells without cells (blanks) were subtracted as background from each sample.

APPENDIX

APPENDIX

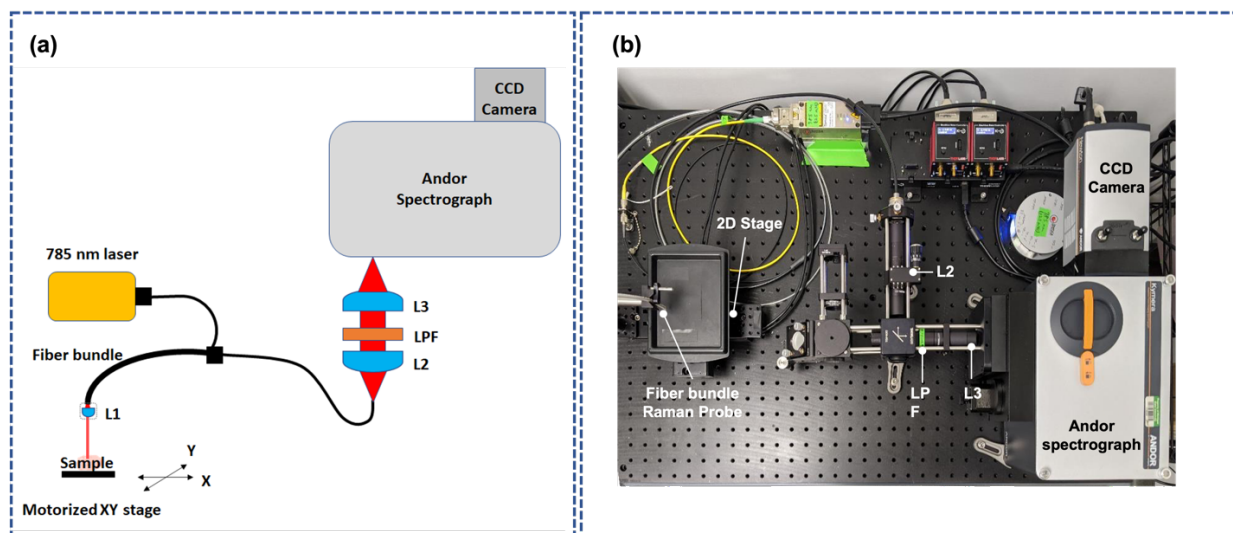


Figure 3.13 (a) Schematic configuration of the fiber bundle Raman spectrometer. (b) Photograph of the fiber bundle Raman spectrometer. A 785 nm laser (iBeam Smart 785, Toptica Photonics, Munich, Germany) is applied to illuminate the sample. The scattered Raman spectra is acquired by the custom-made fiber bundle Raman probe (Fiber guide Industries, Caldwell, ID, USA). The lens L1 ($f=6.83$ mm, PLCS-4.0-3.1-UV, CVI Laser Optics, Albuquerque, NM, USA) is used to collimate both excitation (785 nm laser) and emission (scattered Raman spectra) through the fiber bundle Raman probe. An optical relay, containing two lenses (L2, L3) and a long pass filter (LPF), couples the light into the slit of the spectrometer (Kymera 193i-A, Andor Technology, Belfast, UK) and CCD camera (1024 pixel x 256 pixels with pixel size of 26 μm x 26 μm ; DU920P Bx-DD, Andor technology, Belfast, UK).

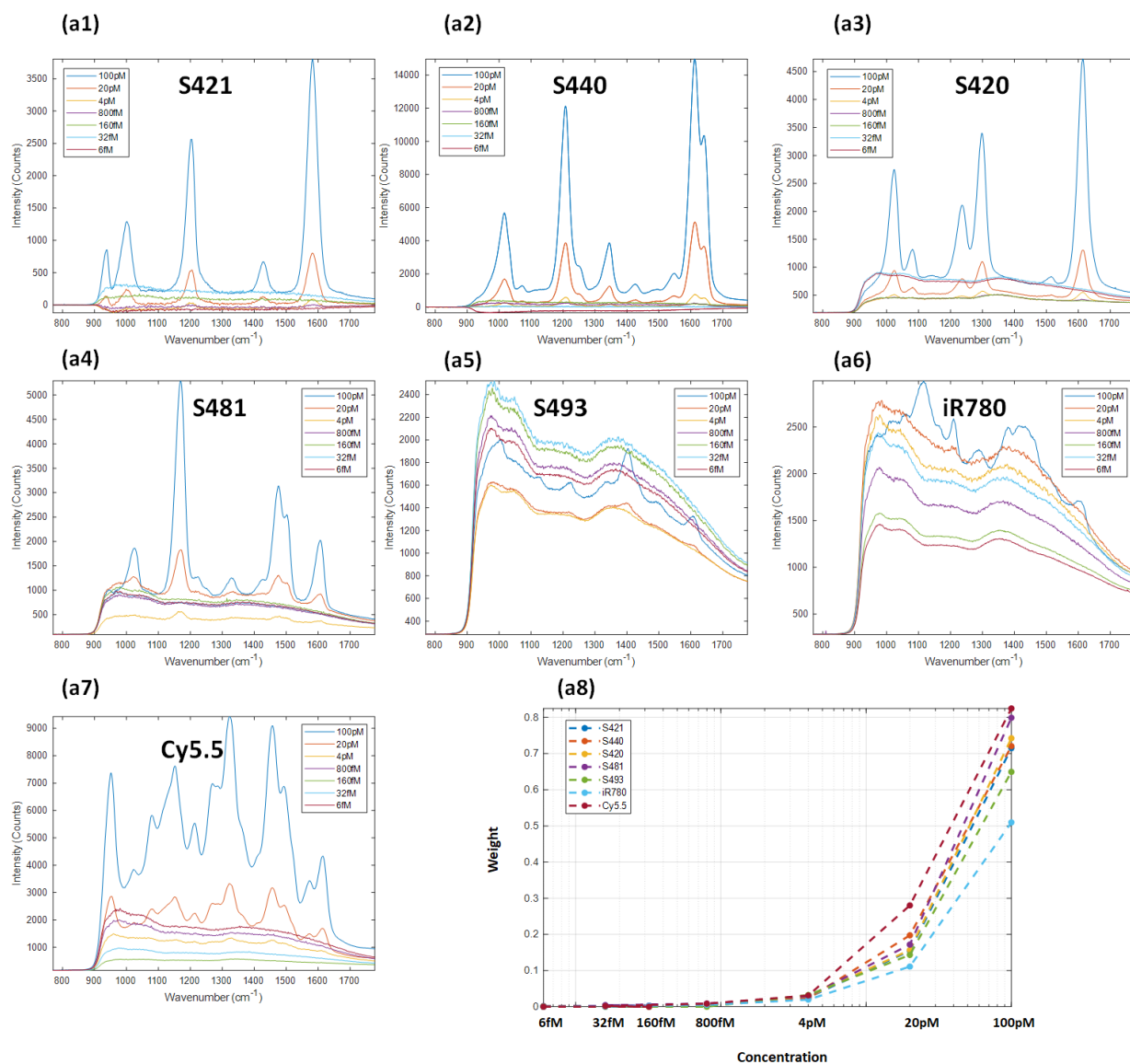


Figure 3.14 (a1-a7) Raman spectra of SERS particles (S420, S421, S440, S481, IR780, and Cy5.5) at seven different concentrations (100 pM, 20 pM, 4 pM, 800 fM, 160 fM, 32 fM, 6 fM) for each flavor; (a8) the quantitative weight calculation graph using demultiplexing algorithm, x-axis is the concentration and y-axis the weight value.

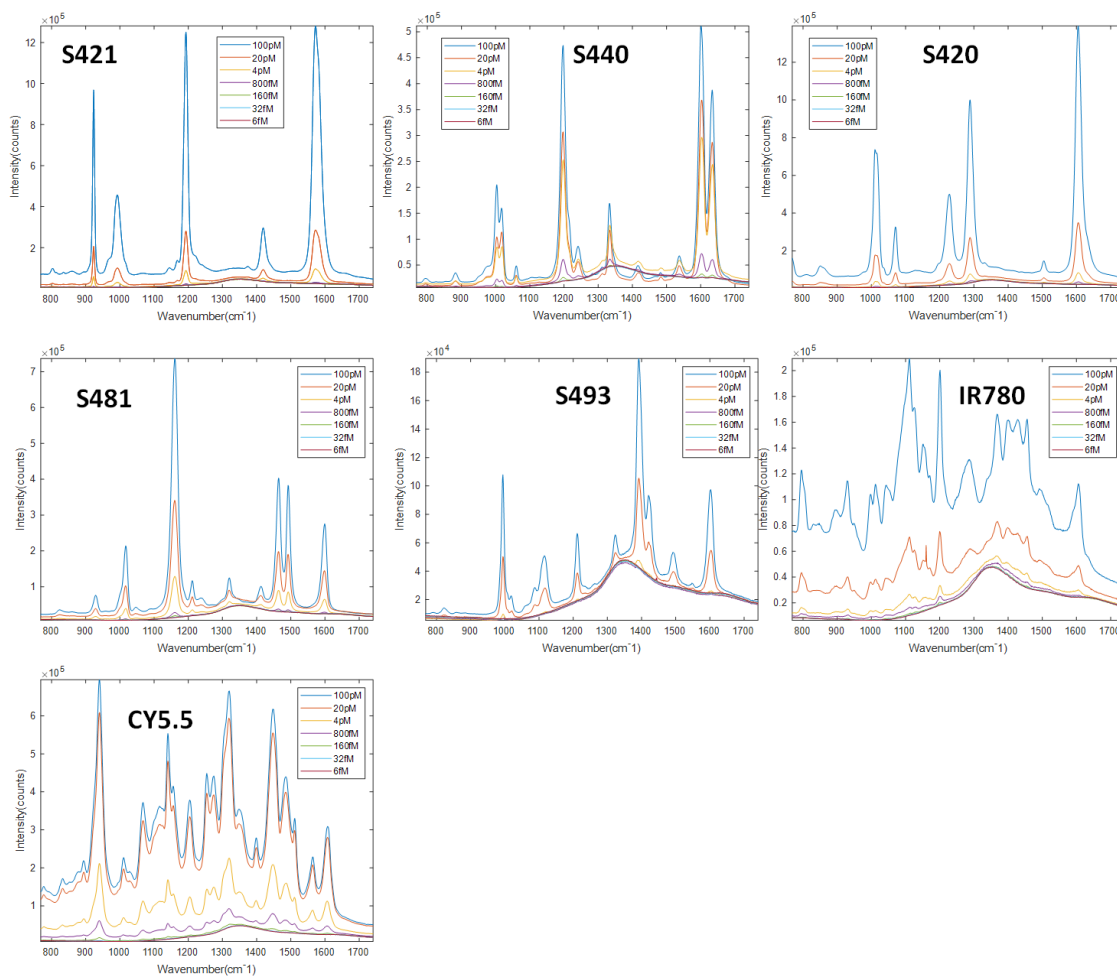


Figure 3.15 (a1-a7) Raman spectra of SERS particles (S420, S421, S440, S481, IR780, and Cy5.5) at seven different concentrations (100 pM, 20 pM, 4 pM, 800 fM, 160 fM, 32 fM, 6 fM) for each flavor; (a8) the quantitative weight calculation graph using demultiplexing algorithm, x-axis is the concentration and y-axis is the weight value.

REFERENCES

REFERENCES

1. McQuillan, A. J., The discovery of surface-enhanced Raman scattering. *Notes Rec. R. Soc. Lond.* **2009**, *63*, 105-109.
2. Turkevich, J.; Stevenson, P. C.; Hillier, J., A study of the nucleation and growth processes in the synthesis of colloidal gold. *Discuss. Faraday Soc.* **1951**, *11*, 55-75.
3. Frens, G., Controlled nucleation for the regulation of the particle size in monodisperse gold suspensions. *Nat. Phys. Sci.* **1973**, *241*, 20-22.
4. Ziegler, C.; Eychmuller, A., Seeded growth synthesis of uniform gold nanoparticles with diameters of 15– 300 nm. *J. Phys. Chem. C* **2011**, *115*, 4502-4506.
5. Bastús, N. G.; Comenge, J.; Puentes, V., Kinetically controlled seeded growth synthesis of citrate-stabilized gold nanoparticles of up to 200 nm: size focusing versus Ostwald ripening. *Langmuir* **2011**, *27*, 11098-11105.
6. Arruebo, M.; Valladares, M.; González-Fernández, Á., Antibody-conjugated nanoparticles for biomedical applications. *J. Nanomater.* **2009**, *2009*.
7. Lee, M.-Y.; Yang, J.-A.; Jung, H. S.; Beack, S.; Choi, J. E.; Hur, W.; Koo, H.; Kim, K.; Yoon, S. K.; Hahn, S. K., Hyaluronic acid–gold nanoparticle/interferon α complex for targeted treatment of hepatitis C virus infection. *ACS Nano* **2012**, *6*, 9522-9531.
8. Okyem, S.; Awotunde, O.; Ogunlusi, T.; Riley, M. B.; Driskell, J. D., Probing the mechanism of antibody-triggered aggregation of gold nanoparticles. *Langmuir* **2021**, *37*, 2993-3000.
9. Jazayeri, M. H.; Amani, H.; Pourfatollah, A. A.; Pazoki-Toroudi, H.; Sedighimoghaddam, B., Various methods of gold nanoparticles (GNPs) conjugation to antibodies. *Sens. Bio-Sens. Res.* **2016**, *9*, 17-22.
10. Gotov, O.; Battogtokh, G.; Shin, D.; Ko, Y. T., Hyaluronic acid-coated cisplatin conjugated gold nanoparticles for combined cancer treatment. *J. Ind. Eng. Chem.* **2018**, *65*, 236-243.
11. Lee, H.; Lee, K.; Kim, I. K.; Park, T. G., Synthesis, characterization, and in vivo diagnostic applications of hyaluronic acid immobilized gold nanoprobe. *Biomaterials* **2008**, *29*, 4709-4718.
12. Li, X.; Zhou, H.; Yang, L.; Du, G.; Pai-Panandiker, A. S.; Huang, X.; Yan, B., Enhancement of cell recognition in vitro by dual-ligand cancer targeting gold nanoparticles. *Biomaterials* **2011**, *32*, 2540-2545.
13. Xia, Y.; Xu, C.; Zhang, X.; Ning, P.; Wang, Z.; Tian, J.; Chen, X., Liposome-based probes for molecular imaging: from basic research to the bedside. *Nanoscale* **2019**, *11*, 5822-5838.

14. Lozano, N.; Al-Jamal, W. T.; Taruttis, A.; Beziere, N.; Burton, N. C.; Van den Bossche, J.; Mazza, M.; Herzog, E.; Ntziachristos, V.; Kostarelos, K., Liposome–gold nanorod hybrids for high-resolution visualization deep in tissues. *J. Am. Chem. Soc.* **2012**, *134*, 13256-13258.
15. Paasonen, L.; Laaksonen, T.; Johans, C.; Yliperttula, M.; Kontturi, K.; Urtti, A., Gold nanoparticles enable selective light-induced contents release from liposomes. *J. Control. Release* **2007**, *122*, 86-93.
16. Mathiyazhakan, M.; Wiraja, C.; Xu, C., A concise review of gold nanoparticles-based photo-responsive liposomes for controlled drug delivery. *Nano-micro letters* **2018**, *10*, 1-10.
17. Park, S.-H.; Oh, S.-G.; Mun, J.-Y.; Han, S.-S., Loading of gold nanoparticles inside the DPPC bilayers of liposome and their effects on membrane fluidities. *Colloids Surf. B. Biointerfaces* **2006**, *48*, 112-118.
18. Mady, M. M.; Fathy, M. M.; Youssef, T.; Khalil, W. M., Biophysical characterization of gold nanoparticles-loaded liposomes. *Phys. Med.* **2012**, *28*, 288-295.
19. Rengan, A. K.; Bukhari, A. B.; Pradhan, A.; Malhotra, R.; Banerjee, R.; Srivastava, R.; De, A., In vivo analysis of biodegradable liposome gold nanoparticles as efficient agents for photothermal therapy of cancer. *Nano Lett.* **2015**, *15*, 842-848.
20. Kojima, C.; Hirano, Y.; Yuba, E.; Harada, A.; Kono, K., Preparation and characterization of complexes of liposomes with gold nanoparticles. *Colloids Surf. B. Biointerfaces* **2008**, *66*, 246-252.
21. Zivanovic, V.; Kochovski, Z.; Arenz, C.; Lu, Y.; Kneipp, J., SERS and cryo-EM directly reveal different liposome structures during interaction with gold nanoparticles. *J. Phys. Chem. Lett.* **2018**, *9*, 6767-6772.
22. Lum, W.; Bruzas, I.; Gorunmez, Z.; Unser, S.; Beck, T.; Sagle, L., Novel liposome-based surface-enhanced raman spectroscopy (SERS) substrate. *J. Phys. Chem. Lett.* **2017**, *8*, 2639-2646.
23. Zhu, D.; Wang, Z.; Zong, S.; Chen, H.; Wu, X.; Pei, Y.; Chen, P.; Ma, X.; Cui, Y., Ag@ 4ATP-coated liposomes: SERS traceable delivery vehicles for living cells. *Nanoscale* **2014**, *6*, 8155-8161.
24. Harmsen, S.; Wall, M. A.; Huang, R.; Kircher, M. F., Cancer imaging using surface-enhanced resonance Raman scattering nanoparticles. *Nat. Protoc.* **2017**, *12*, 1400-1414.
25. Mir-Simon, B.; Reche-Perez, I.; Guerrini, L.; Pazos-Perez, N.; Alvarez-Puebla, R. A., Universal one-pot and scalable synthesis of SERS encoded nanoparticles. *Chem. Mater.* **2015**, *27*, 950-958.
26. Nagy-Simon, T.; Potara, M.; Craciun, A.-M.; Licarete, E.; Astilean, S., IR780-dye loaded gold nanoparticles as new near infrared activatable nanotheranostic agents for simultaneous photodynamic and photothermal therapy and intracellular tracking by surface enhanced resonant

Raman scattering imaging. *J. Colloid Interface Sci.* **2018**, *517*, 239-250.

27. Hong, S.; Li, X., Optimal size of gold nanoparticles for surface-enhanced Raman spectroscopy under different conditions. *J. Nanomater.* **2013**, *2013*.

28. Cho, W.-S.; Cho, M.; Jeong, J.; Choi, M.; Cho, H.-Y.; Han, B. S.; Kim, S. H.; Kim, H. O.; Lim, Y. T.; Chung, B. H., Acute toxicity and pharmacokinetics of 13 nm-sized PEG-coated gold nanoparticles. *Toxicol. Appl. Pharmacol.* **2009**, *236*, 16-24.

29. Xia, H.; Bai, S.; Hartmann, J. r.; Wang, D., Synthesis of monodisperse quasi-spherical gold nanoparticles in water via silver (I)-assisted citrate reduction. *Langmuir* **2010**, *26*, 3585-3589.

30. Zhang, P.; Xi, C.; Feng, C.; Xia, H.; Wang, D.; Tao, X., Transition metal ion-assisted synthesis of monodisperse, quasi-spherical gold nanocrystals via citrate reduction. *CrystEngComm* **2014**, *16*, 5268-5274.

31. Zhang, P.; Li, Y.; Wang, D.; Xia, H., High-Yield Production of Uniform Gold Nanoparticles with Sizes from 31 to 577 nm via One-Pot Seeded Growth and Size-Dependent SERS Property. *Part. Part. Syst. Charact.* **2016**, *33*, 924-932.

32. Li, Y.; Zhang, P.; Duan, J.; Ai, S.; Li, H., One-step seeded growth of monodisperse, quasi-spherical, Tris-stabilized gold nanocrystals with sizes from 17 to 325 nm. *CrystEngComm* **2017**, *19*, 318-324.

33. Baruah, B.; Craighead, C.; Abolarin, C., One-phase synthesis of surface modified gold nanoparticles and generation of SERS substrate by seed growth method. *Langmuir* **2012**, *28*, 15168-15176.

34. Huang, Y.; Kim, D.-H., Synthesis and self-assembly of highly monodispersed quasispherical gold nanoparticles. *Langmuir* **2011**, *27*, 13861-13867.

35. Jana, N. R.; Pal, T., Anisotropic metal nanoparticles for use as surface-enhanced Raman substrates. *Adv. Mater.* **2007**, *19*, 1761-1765.

36. Zavaleta, C. L.; Smith, B. R.; Walton, I.; Doering, W.; Davis, G.; Shojaei, B.; Natan, M. J.; Gambhir, S. S., Multiplexed imaging of surface enhanced Raman scattering nanotags in living mice using noninvasive Raman spectroscopy. *Proc. Natl. Acad. Sci. U.S.A.* **2009**, *106*, 13511-13516.

37. Achike, F. I.; To, N. H. P.; Wang, H.; Kwan, C. Y., Obesity, metabolic syndrome, adipocytes and vascular function: a holistic viewpoint. *Clin. Exp. Pharmacol. Physiol.* **2011**, *38*, 1-10.

38. Xue, Y.; Li, X.; Li, H.; Zhang, W., Quantifying thiol-gold interactions towards the efficient strength control. *Nat. Commun.* **2014**, *5*, 1-9.

39. Ewurum, A.; Alur, A. A.; Glenn, M.; Schnepf, A.; Borchman, D., Hyaluronic acid-lipid binding. *BMC chemistry* **2021**, *15*, 1-8.

40. Cesaretti, M.; Luppi, E.; Maccari, F.; Volpi, N., A 96-well assay for uronic acid carbazole reaction. *Carbohydr. Polym.* **2003**, *54*, 59-61.